Reverse Flow Dynamic Stall Modelling for HAWTs

Belén Sánchez Díaz

Delft University of Technology

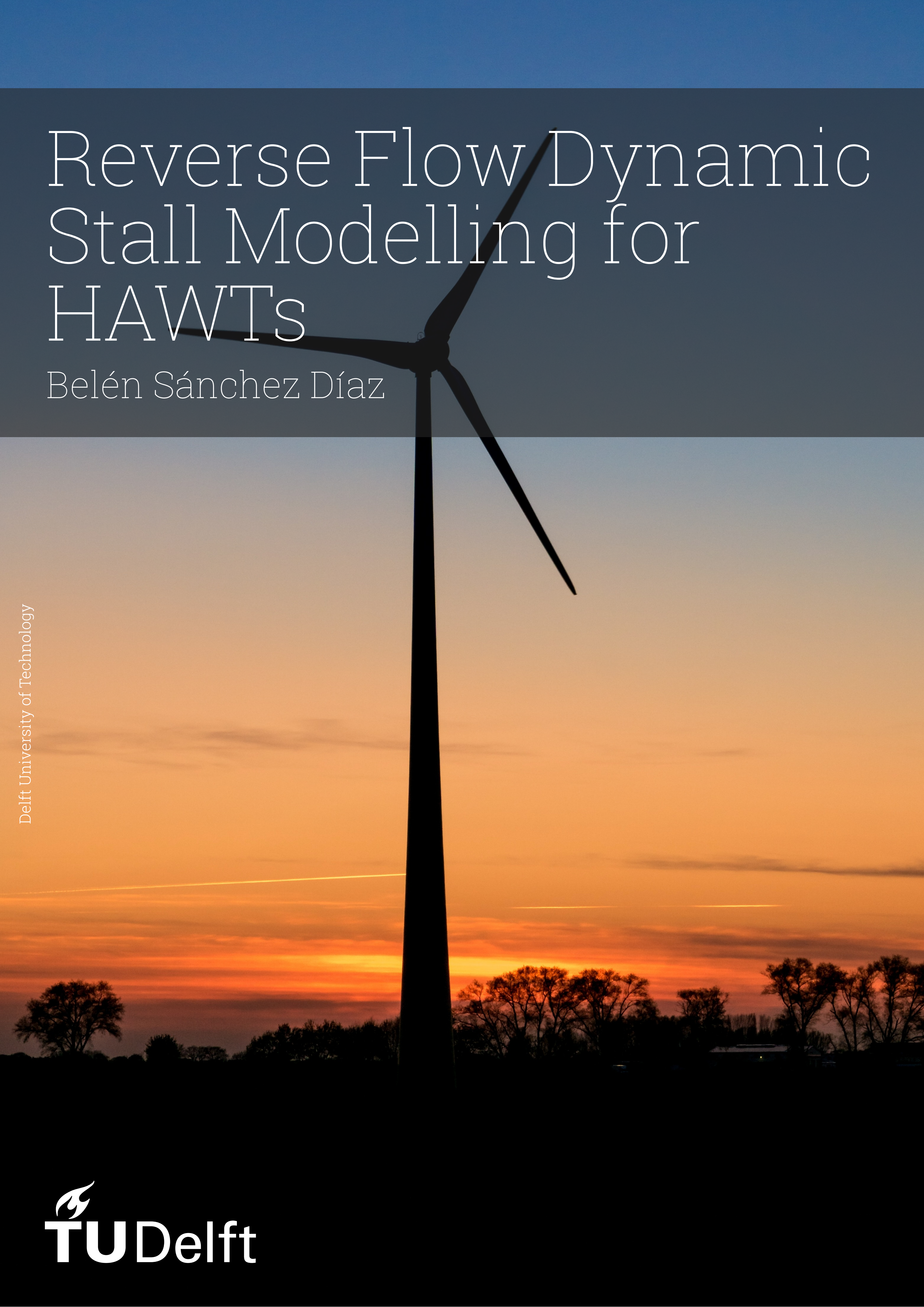

Reverse Flow Dynamic Stall Modelling for HAWTs

by

Belén Sánchez Díaz

To obtain the degree of
Master of Science in Aerospace Engineering
at the Delft University of Technology,
to be defended on Friday September 22, 2023

Student Number:	5215765
TU Delft Supervisor:	Dr. Ragni
General Electric Supervisors:	Dr. Hartung and Dr. Motta
Faculty:	Faculty of Aerospace Engineering, Delft

Acknowledgements

The completion of the Master Thesis is one of the biggest challenges students at TU Delft face. However, the support offered by my supervisors both at General Electric and at TU Delft was extremely valuable to help me accomplish this huge achievement. Thank you Dr. Hartung and Dr. Motta for giving me the opportunity to develop this research in collaboration with GE, which enabled me to gain experience in a field I love and cherish. Thank you Dr. Ragni for the support you offered me to help me finalize this challenging project.

Earning my master's degree would not have been possible without the support of my friends and family, who have encouraged me on a daily basis. I cannot express how grateful I am to my family, who have provided me with this opportunity and many others, showed up when I needed the most and held too many long conversations over the phone when I needed it.

Thank you all.

Abstract

Forward flow dynamic stall is a heavily researched field with multiple well-established models that appropriately capture this type of flow at moderate angles of attack. However, horizontal axis wind turbines operate at a wide range of angles of attack and rapidly changing wind directions, conditions for which limited literature studying the performance of these models has been found. An especially under-researched field is reverse flow dynamic stall, both in terms of experimental investigation and modelling. Therefore, the purpose of this research is to identify the relevant flow phenomena occurring in reverse flow and analyze what dynamic stall models can accurately represent these flow conditions.

The performance of established dynamic stall models such as the one developed by Pierce and the current General Electric dynamic stall model (GE2021) were assessed in reverse flow conditions. In addition, improvements for the GE2021 model were proposed to enhance its performance, including a delay in the effective angle of attack as a function of the reduced frequency and the addition of vortex effects in the load calculation. Three options for the inclusion of vortex effects were explored. The first used the formulation of vortex effects developed by Pierce which, being very similar to those proposed in the original Beddoes-Leishman model, allows to assess the performance of the latter for reverse flow dynamic stall. The second one focused on the interpretation proposed by Sheng, Galbraith and Coton, of the vortex effects calculation formulated by Beddoes. The last consisted on a simplification of the sinusoidal vortex effects computation of the second. In addition, study and tuning of the variables and coefficients involved in this calculation were developed in order to provide a versatile model, with the ability to provide reliable results both in forward and reverse flow conditions.

This project aims to be a first step in the study of reverse flow modelling and to improve our understanding of its modelling requirements.

Contents

List of Figures

List of Tables

Nomenclature

Abbreviations

Abbreviation	Definition
ISA	International Standard Atmosphere
LE	Leading Edge
TE	Trailing Edge
DSV	Dynamic Stall Vortex
LEV	Leading Edge Vortex
TEV	Trailing Edge Vortex
PDSV	Primary Dynamic Stall Vortex
SDSV	Secondary Dynamic Stall Vortex
HAWTs	Horizontal Axis Wind Turbines

Symbols

Symbol	Definition	Unit
α	Angle of Attack	[deg]
α_0	Angle of Attack at Zero-Lift	[deg]
α_1	Angle of Attack at $f = 0.7$	[deg]
α_a	Pitching motion amplitude	[deg]
α_E	Effective Angle of Attack from Beddoes-Leishman	[deg]
α_{eff}	Effective Angle of Attack	[deg]
α_m	Mean Angle of Attack	[deg]
α_{mod}	Modified Angle of Attack	[deg]
α_{rev}	Reverse Flow Angle of Attack	[deg]
β	Prandtl-Glauert factor	[-]
ρ	Flow Density	[kg/m^3]
ω	Rotational Frequency	[rad/s]
τ	Vortex Position	[-]
a	Speed of Sound	[m/s]
c	Chord	[m]
C_l	Lift Coefficient	[-]
C_{l_α}	Lift Coefficient Slope	[-]
C_{l_0}	Lift Coefficient at Zero-Lift	[-]
C_d	Drag Coefficient	[-]
C_N	Normal Force Coefficient	[-]
C_{N_α}	Normal Force Coefficient Slope	[-]
C_C	Chordwise Force Coefficient	[-]
f	Separation Point	[-]
k	Reduced Frequency	[-]
M	Mach Number	[-]
Re	Reynolds Number	[-]
S	Non-Dimensional Time using Freestream Velocity	[-]
s	Non-Dimensional Time using Relative Velocity	[-]

Symbol	Definition	Unit
St	Strouhal Number	[-]
t	Time	[s]
T	Total Pitch Cycle Time	[s]
T_f	Separation Point Time Constant	[-]
T_I	Impulsive or Non-Circulatory Time Constant	[-]
T_p	Pressure Time Constant	[-]
T_{St}	Strouhal Number related Time Constant	[-]
T_v	Vortex Decay Time Constant	[-]
T_{VL}	Vortex Passage Time Constant	[-]
U	Velocity	[m/s]
U_∞	Free-stream velocity	[m/s]
w_{LE}	Induced Velocity at the Leading Edge	[m/s]
^{C}	Circulatory	
^{I}	Impulsive or Non-Circulatory	
$_n$	N-th Timestep	
$_{eff}$	Effective	
$_{stat}$	Static	
$_{rel}$	Relative	
$_{dyn}$	Dynamic	
$_{inv}$	Inviscid	
$_{visc}$	Viscous	
$_{sep}$	Separation	
$_{mod}$	Modified	

1 Introduction

Horizontal Axis Wind Turbines (HAWTs) have become one of the most prominent sources of clean energy battling climate change. This is only possible through the development of leading innovative technologies. These include the development of longer, more slender and flexible blades that operate in taller towers. While wind turbine energy output increases, these systems are subject to complex structural vibrations and loads that cannot only lead to lower energy capture efficiency but most importantly to failure. Damage in HAWT blades can lead to blade fracture and can become catastrophic. Therefore, it is of utmost importance to correctly assess the behaviour and quantification of aerodynamic loads in blades.

One of the relevant flow phenomena these slender and flexible blades encounter is dynamic stall, in which the aerodynamic body is subject to changing inflow conditions and/or angles of attack. Dynamic stall is characterized by hysteresis cycles, turbulent flows and separation regions that make the study of this phenomenon incredibly complex. In addition, the unsteady nature of dynamic stall makes its modelling challenging. Nevertheless, several models have been developed from the late 1980s with results that closely resemble the experimental data, as well as a variety of variations in their formulations.

However, due to the fact that most of these models were initially developed to assess loads for helicopter blades, their validation was typically limited to a small range of angles of attack, usually positive and close to zero. HAWT blades are subject to a wider variety of angles of attack, and rapidly changing wind speeds and directions. In addition, pitch and yaw controls are slow compared to these rapid changes, and inactive when the turbine is in parked and idling conditions, increasing the likelihood of experiencing angles of attack anywhere between $0°$ and $360°$ [1]. It is also important to note that HAWT spend a between a 10% and a 35% of their lifespan in parked and idling conditions, making it crucial to obtain an accurate assessment of the loading these can be subjected to during that time [2].

Limited research about the aerodynamic phenomena of reverse flows (airfoil at around an angle of attack of $180°$) is available, for both experimental and modelling, mostly focusing on steady conditions. Dynamic stall in reverse flows is also a phenomenon of great interest in the helicopter industry, as the rotor blades are subject to a reverse flow region. Thus, the limited experimental research available focuses on thin airfoils that could belong to helicopter rotor blades. On the other hand, the modelling of reverse flows dynamic stall is an entirely unexplored matter, with only one abstract available [3], but no published literature.

Therefore, this research aims to give an overview of the of reverse flow dynamic stall characteristics, while identifying its main differences to the more researched forward flow dynamic stall, as well as the effect of different pitching dynamics parameters and flow conditions on reverse flow dynamic stall, available in Chapter 2. Different dynamic stall models and variants are summarized in Chapter 3, providing an outline and discussing their potential to model reverse flow dynamic stall.

Chapter 5 focuses on the assessment of the performance of the established models, Pierce, GE2021 and an interpretation of the SGC model proposed by Sheng, Galbraith and Coton, in reverse flow dynamic stall conditions. After said analysis, three proposals for vortex effects modelling were added to the GE2021 model in order to improve its performance in reverse flow conditions. These were tackled in Chapter 6. First, the implementation of the vortex effects proposed by Pierce were used. Afterwards, a modification of the SGC vortex effects modelling as well as a simplification of this sinusoidal implementation were analyzed. For these two last models, an added delay in the angle of attack proportional to the reduced frequency was considered.

To conclude, in Chapter 7, established and newly proposed models were compared and validated in forward and reverse flow conditions to assess their performance and in Chapter 8, conclusions and recommendations for future work were discussed.

2
Dynamic stall

HAWT operate in unsteady aerodynamic conditions with rapidly fluctuating windspeed and direction. These unsteady inflow conditions generate rapidly changing effective angles of attack in addition to yawed flows before the steering mechanism can compensate for these [4]. Parked or idling conditions are also necessary in HAWT lifespan, during installation or when maintenance is taking place for example. In these conditions pitch and yaw controls are inactive, preventing any possible mitigation of the unsteady aerodynamic inflow conditions and possible high angles of attack or reverse flow (angles of attack close to $\alpha = 180°$) for which the HAWT has not been designed and optimized [5].

Therefore, the study of unsteady aerodynamics and its effects is crucial for an accurate prediction of these unsteady phenomena and the design of more efficient and reliable wind turbines. While the dynamic inflow conditions are of great importance, the focus of this research is the unsteady airfoil aerodynamics and dynamic stall of a pitching airfoil.

When an airfoil is subjected to a certain angle of attack, a pressure imbalance between the upper and lower surface of the studied geometry can cause flow separation resulting in a lift reduction and drag increase. When flow separation becomes severe enough, a sudden strong lift reduction and drag increase occur, this is referred to as stall. Stall occurs when an airfoil surpasses a critical angle of attack and is highly dependent on the airfoil's geometry [6].

Dynamic stall refers to the stalling of an airfoil under unsteady flow conditions that can be sometimes associated to pitching or plunging motions. This phenomenon has been long studied and documented. As previously mentioned, static stall occurs when the studied airfoil is at an angle of attack that exceeds its critical angle of attack. In the case of an oscillating airfoil, the rapid pitch up can delay the onset of stall. However, once stall is onset, dynamic stall has greater effects and is more persistent than static stall, with aerodynamic forces suffering hysteresis with respect to the instantaneous angle of attack ($\alpha(t)$) [7].

Most of the prior experimental research on dynamic stall focuses on two-dimensional oscillating airfoils. However, even after simplifying the setup and conditions, a large number of parameters affect the dynamic stall phenomenon. Some relevant parameters in dynamic stall include the reduced frequency (k), mean pitch angle (α_m) and pitch amplitude (α_a). The reduced frequency is a function of the free-stream velocity U_∞, the rotational frequency (ω) and the chord (c), can be defined as:

$$k = \frac{\omega c}{2U_\infty}$$

The aforementioned parameters influence the temporal progression of dynamic stall and affect the extent of flow separation [8]. The magnitude of the mean pitch angle (α_m) and pitch amplitude

(α_a) determine the extent to which the static stall angle is surpassed or avoided. Consequently, this combination plays a significant role in determining the type of dynamic stall, and the influence of the dynamic stall vortex (DSV) on the distribution of unsteady pressure. Reduced frequency (k) affects the strength of the suction peak generated by the dynamic stall. Additionally, it has an impact on the onset and persistence of the DSV during. Thus, reduced frequency has a major impact on the generated airloads during the pitching cycle [9][8][10].

2.1. Forward Flow Dynamic Stall

Dynamic stall is characterized by the shedding of vortex-like disturbances that move over the airfoil's upper surface, inducing a highly unsteady and fluctuating pressure field. The vortex generation and shedding process was divided in 5 stages by Leishman [11] represented in Figure 2.1. During the first stage, the airfoil follows a pitch-up motion, increasing the angle of attack up to the static stall angle of attack. In the second stage, past the static stall angle of attack, flow reversal appears in the boundary layer near the leading edge and spreads downstream. However, loads are not greatly affected at this stage, and the lift coefficient maintains its linear trend. The third stage is characterized by the leading edge vortex (LEV) convection, decreasing the pressure on the suction side, and therefore increasing lift. At the fourth stage, the vortex reaches the trailing edge, shedding from the airfoil, and the flow fully separates. This causes stall to initiate, with a abrupt decrease in lift. The last stage is the reattachment that occurs during the pitch down, or decrease of the angle of attack, when a sufficiently small angle of attack has been reached, the flow reattaches from the leading edge (LE) to the trailing edge (TE). During the flow reattachment, the airfoil loading approaches the static lift curve [11].

The five stages previously described do not necessarily occur in every dynamic stall cycle, and static coefficient curves do not always remain within the unsteady values as it can be observed in the drag coefficient plot in Figure 2.1.

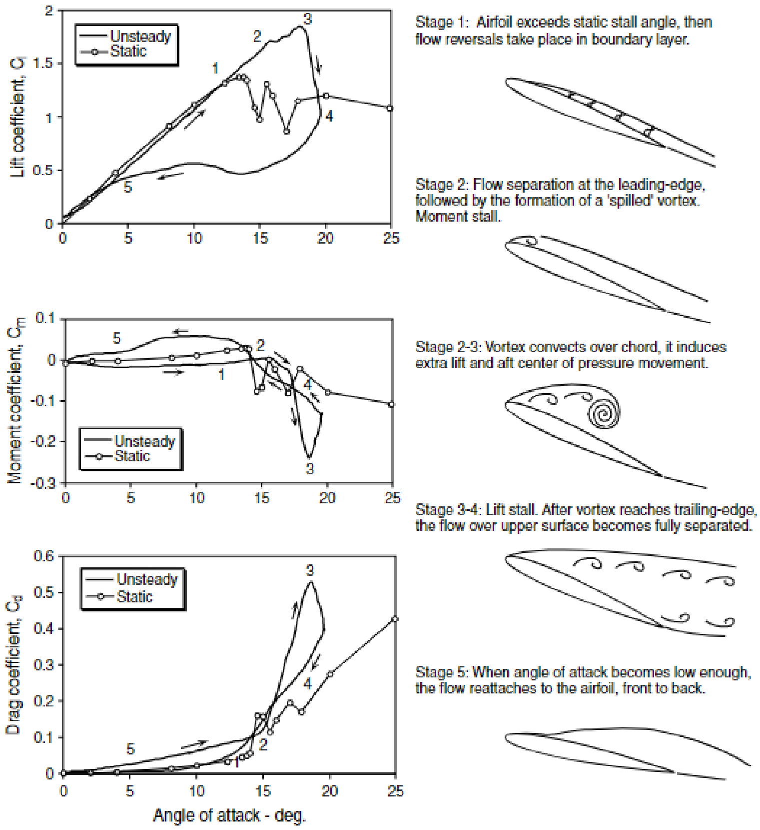

Figure 2.1: Forward Flow Dynamic Stall Physics [11]

In the past, distinctions have been made between light and deep stall. Light stall is used to refer to the stall motion in which the airfoil periodically moves in and out of stall, with a maximum pitching angle slightly over the critical static stall angle. Therefore, occurring when the pitching motion has a small mean angle of attack and pitching amplitude. This limited motion makes for mild flow separation, and leading edge vortex shedding at the end of the upstroke. In light stall, airfoil geometry, airfoil motion and flow characteristics are relevant to the airfoil behaviour.

In deep stall, the mean angle of attack and amplitude at which the pitching motion occurs exceed greatly the static stall angle of attack, making flow reattachment less likely. Therefore, vortex shedding becomes the most dominant phenomenon. The leading edge vortex is shed before the maximum angle of attack is reached, allowing for several vortices to be generated and shed in a single pitch up motion. As a result of the vortex shedding in deep stall, the viscous layer becomes significantly larger, generating severe and rapid changes and hysteresis of unsteady airloads. Deep stall is also less dependent on airfoil or flow characteristics compared to light stall.

Due to the differences between the flow phenomena occurring in light and deep stall, their modelling requirements and characteristics also differ. Reverse flow dynamic stall will be explored in the following section (Section 2.2), but it is worth mentioning that the vortex shedding characteristics of reverse flow dynamic stall are more similar to those of forward flow deep dynamic stall. Thus, it is interesting to study the formulation of vortex effects in forward flow deep stall, as they are more likely to represent reverse flow dynamic stall more closely than those designed for light stall.

2.2. Reverse Flow Dynamic Stall

HAWT are subjected to rapidly changing wind speeds and directions, therefore operating at high and rapidly changing angles of attack, even at angles around $\alpha = 180°$, when the airflow moves from the trailing edge (TE) of the blade to the leading edge (LE). These conditions will be referred as reverse flow. Literature about reverse flow is very limited, and has been mostly focused on the reverse flow region of helicopter rotors.

The characterization of reverse flow, as well the effects of Reynolds number, reduced frequency, mean pitch angle and pitch amplitude, will mostly come from the research carried out by A. Lind in the Department of Aerospace Engineering of the University of Maryland [10][12][13]. Prior to the development of this research, having the sharp geometrical trailing edge as the aerodynamic leading edge was known to cause early flow separation and multiple vortex formation for a NACA 0012 in reverse flow dynamic stall. However, there was no quantification of the effect of these phenomena on the unsteady airloads, nor the effect of Reynolds number (Re), reduced frequency, mean pitch angle and pitch amplitude on the development of reverse flow dynamic stall.

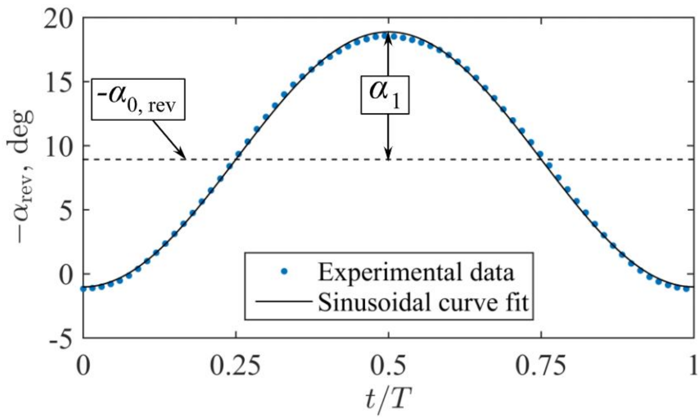

Figure 2.2: Pitch cycle with $\alpha_{m,rev} = -8.9°$, $\alpha_a = 9.9°$, $Re = 3.3 \times 10^5$, $k = 0.160$ [10]

Although the studies carried out by A. Lind were extremely detailed and covered many of the key parameters involved in reverse flow dynamic stall behaviour, its limitations reside in the few airfoil geometries studied. Reynolds number effects in static reverse flow were studied for a NACA 0012, a NACA 0024, an elliptical airfoil, and a cambered elliptical airfoil [13]. However, for reverse flow dynamic stall conditions, a thin symmetric airfoil (NACA 0012) was the focus of study [10][12], which is a disadvantage when trying to assess the possible effects of reverse flow dynamic stall in wind turbine applications where airfoil geometries vary greatly. Nevertheless, it is a good starting point to better understand the most relevant characteristics and the possible requirements when modelling reverse flow dynamic stall.

To better describe the main characteristics of reverse flow dynamic stall, as studied by A. Lind [10], a case with $\alpha_m = 171.1°$, $\alpha_a = 9.9°$, $Re = 3.3 \times 10^5$, $k = 0.160$. To ease the visualization a reverse flow angle of attack can be defined as $\alpha_{rev} \equiv \alpha - 180°$. Therefore, the case studied will have a mean angle of attack $\alpha_{m,rev} = -8.9°$. In addition, the cycle period is defined as T, being t/T the dimensionless cycle phase. The pitch cycle development follows the cycle phase and angle of attacks represented in Figure 2.2.

Reverse flow dynamic stall has a similar behaviour to deep stall as dynamic stall vortices convect along the chord starting at the aerodynamic leading edge and causing nonlinear airloads. The type of reverse flow dynamic stall is defined by the number of vortices generated throughout the pitching cycle. Figure 2.3 shows a type III reverse flow dynamic stall, as a primary dynamic stall vortex (PDSV), trailing edge vortex (TEV), and secondary dynamic stall vortex (SDSV) can be observed. Figure 2.3 shows the suction side of the airfoil in reverse flow, where the geometric trailing edge becomes the aerodynamic leading edge, which is defined as $x/c = 0$. Figure 2.3 (a) shows a contour of the velocity field normalized with the freestream velocity. Figure 2.3 (b) portrays the vorticity fields normalized using the chord length and the freestream velocity. Figure 2.3 (c) shows the chordwise unsteady pressure distributions with the grey shaded areas representing $\pm\sigma(c_p)$. In addition, the vortex centers are represented using triangular markers [10].

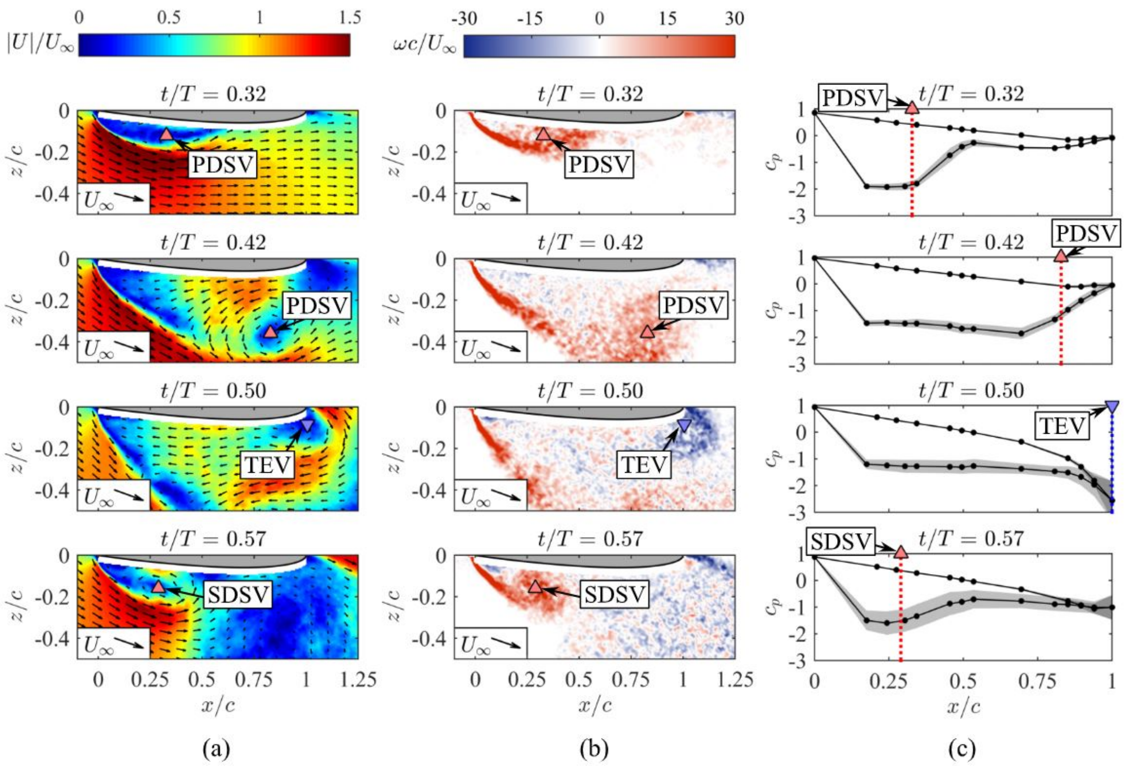

Figure 2.3: Evolution of reverse flow dynamic stall with $\alpha_{m,rev} = -8.9°$, $\alpha_a = 9.9°$, $Re = 3.3 \times 10^5$, $k = 0.160$. (a) Total velocity fields. (b) Vorticity fields. (c) Chordwise pressure distributions.[10]

During the initial phase of the pitching cycle (0 ≤ t/T ≤ 0.20, not depicted), the airflow remains attached but separates near the blunt aerodynamic trailing edge. For classical dynamic stall the formation of PDSV occurs close to t/T = 0.35 [12]. However, in reverse flow dynamic stall, the PDSV formation begins much earlier at around t/T = 0.23. The movement of the PDSV over the chord and its convection away from the blade, prompts the generation of a TEV at around $t/T = 0.5$, which is a similar timing to classical dynamic stall. The convection of the TEV into the wake allows for the generation of a SDSV from the roll up of the leading edge shear layer. The SDSV moves into the wake by $t/T = 0.67$ and does not develop to be as large as the PDSV. The flow does not reattach until $t/T \geq 0.85$, from the leading edge to the trailing edge [10].

Figure 2.4 portrays the phase-averaged pressure distributions in forward flow (bottom) and reverse flow (top), Figure 2.4 (a) representing the suction side of the airfoil, while Figure 2.4 (b) displays the pressure side. Measurements were not possible near the sharp geometric trailing edge, therefore, the measurements for the affected area were extrapolated and are displayed with a transparent black region. In the case of forward flow, the aerodynamic leading edge is the geometric leading edge. For reverse flow, the aerodynamic leading edge is the sharp geometric trailing edge [10].

In forward flow, the suction gradually builds up near the leading edge, later forming a dynamic stall vortex that causes a low pressure wave that convects chordwise as the cycle progresses. After the DSV is shed, the flow remains fully separated thus the pressure distribution along the chord is nearly uniform. On the pressure side, the pressure increases during the first half of the cycle and during the second half there is a decrease related to the translation of the stagnation point in the leading edge direction once the DSV convects into the wake [10].

Although no measurements are available for reverse flow conditions on the aerodynamic leading edge, the pressure is not steadily built up on the suction side as it is for forward flow. Instead, when the primary dynamic stall forms and convects along the suction side of the blade from $0.25 \leq t/T \leq 0.50$, the pressure declines along an increasing percentage of the chord.This demonstrates a key distinction between a dynamic stall in forward flow and one in reverse flow: in the latter, the principal dynamic stall vortex originates earlier in the cycle and convects more slowly than in the former [10].

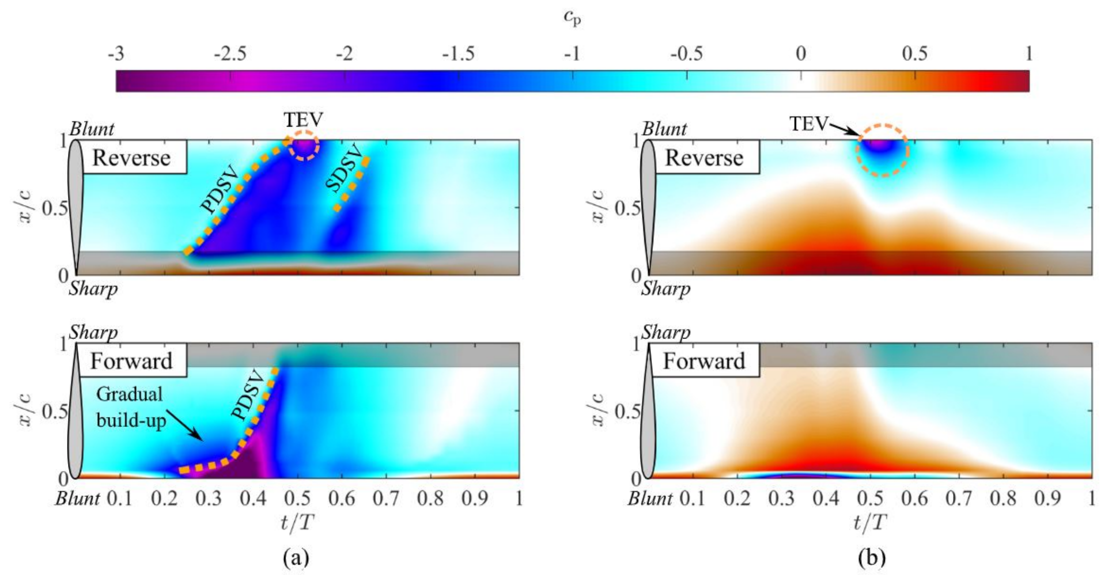

Figure 2.4: Phase-averaged pressure distributions in forward flow ($\alpha_m = 11°$, $\alpha_a = 9.9°$) and reverse flow ($\alpha_{m,rev} = -8.9°$, $\alpha_a = 9.9°$) for $Re = 3.3 \times 10^5$ and $k = 0.160$. (a) Suction side. (b) Pressure side. [10]

The convection speed in forward flow, can be measured by the linear parts of the slope of each pressure wave, is $u_w/U_\infty \approx 0.34$, which is 70% higher than the convection speed in reverse flow, $u_w/U_\infty \approx 0.20$ [10]. This variation in convection speed is thought to be related to the formation of the first vortex timing. In forward flow, the blunt leading edge allows for the vortex to form later in the cycle, when the angle of attack has reached higher values, forming a stronger vortex. The strong low pressure region close to the leading edge for $0.27 \leq t/T \leq 0.42$ shows the formation of the stronger vortex, which consequently convects faster over the chord than in reverse flow. In addition, while in the case of forward flow only a single DSV is formed, in reverse flow several vortex structure form [10].

Another interesting characteristic to study is the boundary layer transition from laminar to turbulent affect pressure fluctuations studied in Figure 2.5. While in forward flow these pressure fluctuations remain low during $0 \leq t/T \leq 0.3$. Afterwards the formation of the DSV generate large pressure fluctuations near the leading edge, which extend over the chord with time. Pressure fluctuations remain mostly constant between $0.5 \leq t/T \leq 0.7$, when the flow is fully separated, with high fluctuations near the leading edge that can be attributed to the unsteadiness of the separation point. However, as the cycle progresses the pressure fluctuations decrease, also at the leading edge as the separation point moves towards the leading edge, as the flow reattaches[10].

In the results obtained in reverse flow, pressure fluctuations from the boundary layer transition from laminar to turbulent are not visible. Therefore, it can be inferred that the transition occurs close to the sharp aerodynamic leading edge [10]. This is consistent with the results obtained in the study of static reverse flow that shows the generation of a small separation bubble near the sharp aerodynamic leading edge at low angles of attack [13]. However, it is still possible to track the pressure fluctuations generated by the PDSV, which first appear at $t/T = 0.25$ and reach the blunt trailing edge at $t/T = 0.41$. The TEV ($0.45 \leq t/T \leq 0.6$) and SDSV ($0.55 \leq t/T \leq 0.65$) show high levels of pressure fluctuations which might indicate aperiodicity [10].

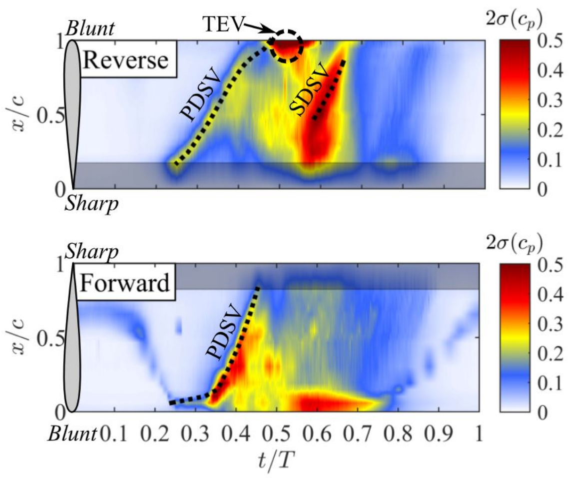

Figure 2.5: Pressure fluctuations on the suction side in forward flow ($\alpha_m = 11°$, $\alpha_a = 9.9°$) and reverse flow ($\alpha_{m,rev} = -8.9°$, $\alpha_a = 9.9°$) for $Re = 3.3 \times 10^5$ and $k = 0.160$. [10]

Unsteady airloads for forward and reverse flow are showcased in Figure 2.6. In forward flow both lift (C_l) and drag (C_d) coefficients increase linearly until the DSV forms, starting flow separation at around $t/T = 0.35$, causing a rapid increase in C_d.

In reverse flow, the lack of measurements near the sharp aerodynamic leading edge makes the C_l increase non-linearly, as the extrapolated pressure measurement is more likely higher than the actual value as the reverse flow DSV forms nearby. The early and fast increase in drag coefficient ($0.2 \leq t/T \leq 0.4$) is consistent with the earlier generation of the first DSV and its slower convection speed. The magnitude of the pitching moment coefficient (C_m) is greater in reverse flow as the center of pressure is acting close to the aerodynamic quarter chord, which creates an arm of $0.5c$.

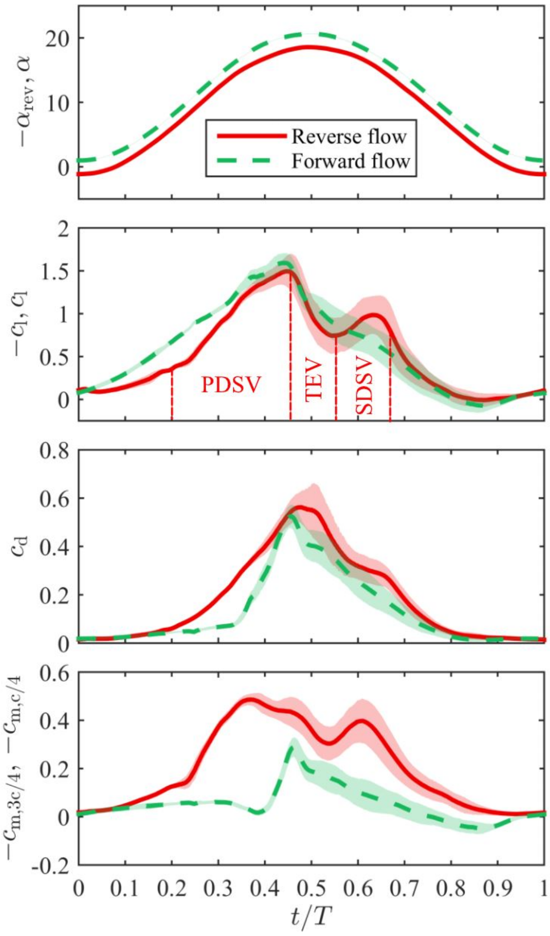

Figure 2.6: Kinematics and airloads in forward flow ($\alpha_m = 11°$, $\alpha_a = 9.9°$) and reverse flow ($\alpha_{m,rev} = -8.9°$, $\alpha_a = 9.9°$) for $Re = 3.3 \times 10^5$ and $k = 0.160$. [10]

To summarize, under the pitching and flow circumstances addressed in this section, forward and reverse flow dynamic stalls have different flow separation properties. In forward flow, flow separation and the resulting vortex formation happen when the negative pressure gradient caused by the suction peak close to the blunt leading edge surpasses a certain critical value. In reverse flow, the sharp aerodynamic leading edge causes a locally strong adverse pressure gradient leading to flow separation and vortex formation at significantly lower angles of attack. Furthermore, a trailing edge vortex and secondary dynamic stall vortex form. The trailing edge vortex reduces lift and pitching moment coefficients. Meanwhile, the secondary dynamic stall vortex generates a second pressure wave, which increases lift and pitching moment coefficients.

As mentioned at the end of Section 2.1, deep dynamic stall in forward flow has similar characteristics to the ones in reverse flow dynamic stall. Multiple vortex structures are generated and their shedding is the most predominant characteristic. Therefore, from a modelling point of view, a comparison between forward flow deep dynamic stall and reverse flow dynamic stall could provide insight about possible applicable dynamic stall modelling techniques. Furthermore, a wider understanding of reverse flow dynamic stall would be possible if multiple airfoil geometries were studied, such as thicker or cambered airfoils.

2.2.1. Reynolds Number effect

A NACA 0012 (“thin” airfoil) and NACA 0024 (“thick” airfoil) were studied in static conditions for Reynolds numbers ranging from $Re = 1.1 \times 10^5$ to $Re = 1.0 \times 10^6$ [13]. The NACA 0012 showed low sensitivity to the Reynolds number in reverse flow at angles of attack ranging from $-3° \leq -\alpha_{rev} \leq$

$30°$. This is associated to the flow separation due to the sharp leading edge that occurs early at moderate angles of attack ($-\alpha_{rev} \approx 7°$). Partial reattachment occurs further down the chord and slightly decreases with increasing Reynolds number, but this does not have much effect on the airloads. In the case of the thicker airfoil (NACA 0024), a light sensitivity is observed in moderate angles of attack $-3° \leq -\alpha_{rev} \leq 13°$. However, for lager angles of attack the Reynolds number does not seem to impact the measured airloads, suggesting full separation for $-\alpha_{rev} \geq 13°$ [13].

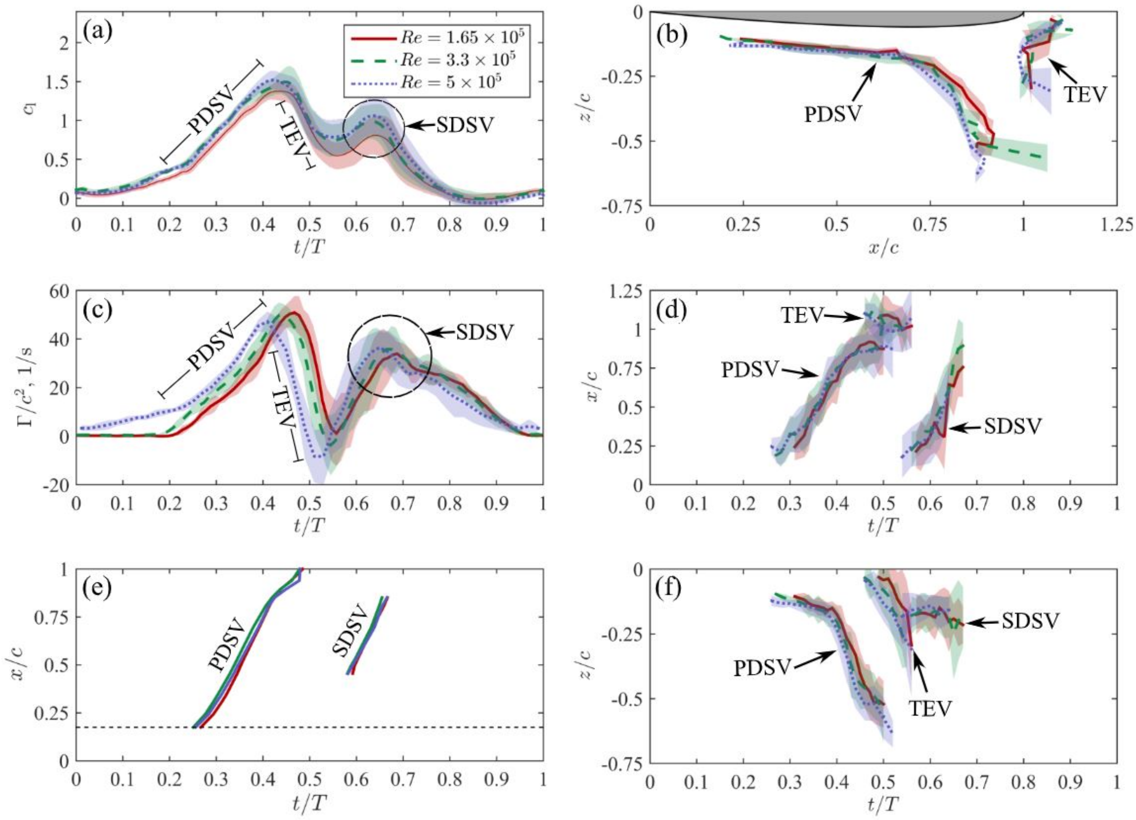

Figure 2.7: Reynolds number effect reverse flow for a NACA 0012 with $\alpha_{m,rev} = -8.9°$, $\alpha_a = 9.9°$ and $k = 0.160$. (a) Unsteady lift. (b) Blade-relative vortex tracks. (c) Suction side circulation. (d) Vortex tracks,x-coordinate. (e) Phase-averaged pressure waves. (f) Vortex tracks,z-coordinate.[10]

The case of dynamic stall in reverse flow was studied using a NACA 0012 airfoil. Similarly to the steady case, the unsteady lift curve, as well as the variation of the unsteady circulation in the suction side who no major dependency on the Reynolds number. Figure 2.7 clearly shows the limited effect the Reynolds number has on the various studied parameters, even showcasing the $\pm 2\sigma$ variations using shaded regions [14].

A similar case with a smaller amplitude was also studied supporting that for the studied ranges the unsteady loads are insensitive to Reynolds number variations [12]. As previously discussed, this can be attributed to the early flow separation occurring close and due to the sharp leading edge, thus avoiding the influence of the Reynolds number on the boundary layer transition or separation point.

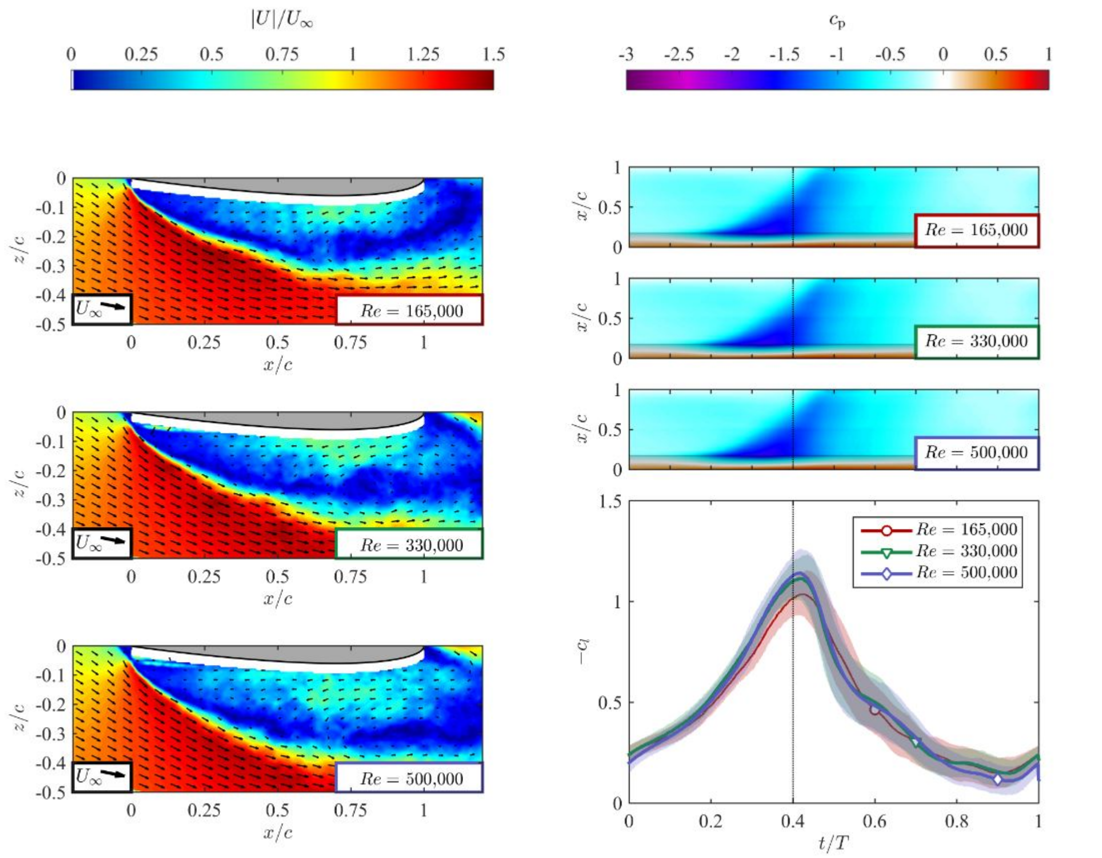

(a) Phase-averaged velocity fields at $t/T = 0.4$.

(b) Phase-averaged pressure distributions and unsteady lift.

Figure 2.8: Reynolds number effect reverse flow for a NACA 0012 with $\alpha_{m,rev} = -10°$, $\alpha_a = 5°$ and $k = 0.160$. [12]

2.2.2. Reduced frequency effects

Reduced frequency affects greatly dynamic stall in forward flow. Increasing the reduced frequency increases the effective induced camber delaying the formation of the dynamic stall vortex [15] and delays reattachment and recovery of the flow [8]. Furthermore, increasing k and its consequent reattachment delay lowers lift coefficient in the later phases of the pitching cycle [12].

Reverse flow dynamic stall reduced frequencies ranging from $k = 0.100$ to $k = 0.511$ were studied for different values of Reynolds number after determining that the effect of the Reynolds number on the airfoil performance in reverse flows is negligible. Nevertheless, three cases use a common $Re = 3.3 \times 10^5$. The type of dynamic stall reduces as the reduced frequency increases. Therefore, for $k = 0.100$, $k = 0.160$ and $k = 0.217$ a secondary dynamic stall vortex can be observed in Figure 2.9, but a type II dynamic stall takes place for $k = 0.309$ and a type I for $k = 0.511$. The change in type of dynamic stall also has an effect on the aerodynamic loads as it can be seen when observing the lift coefficient (C_l) behavior. In addition, a higher reduced frequency implies a shorter cycle time which leads the generated DSV to be over the blade for a longer portion of the pitching cycle [14].

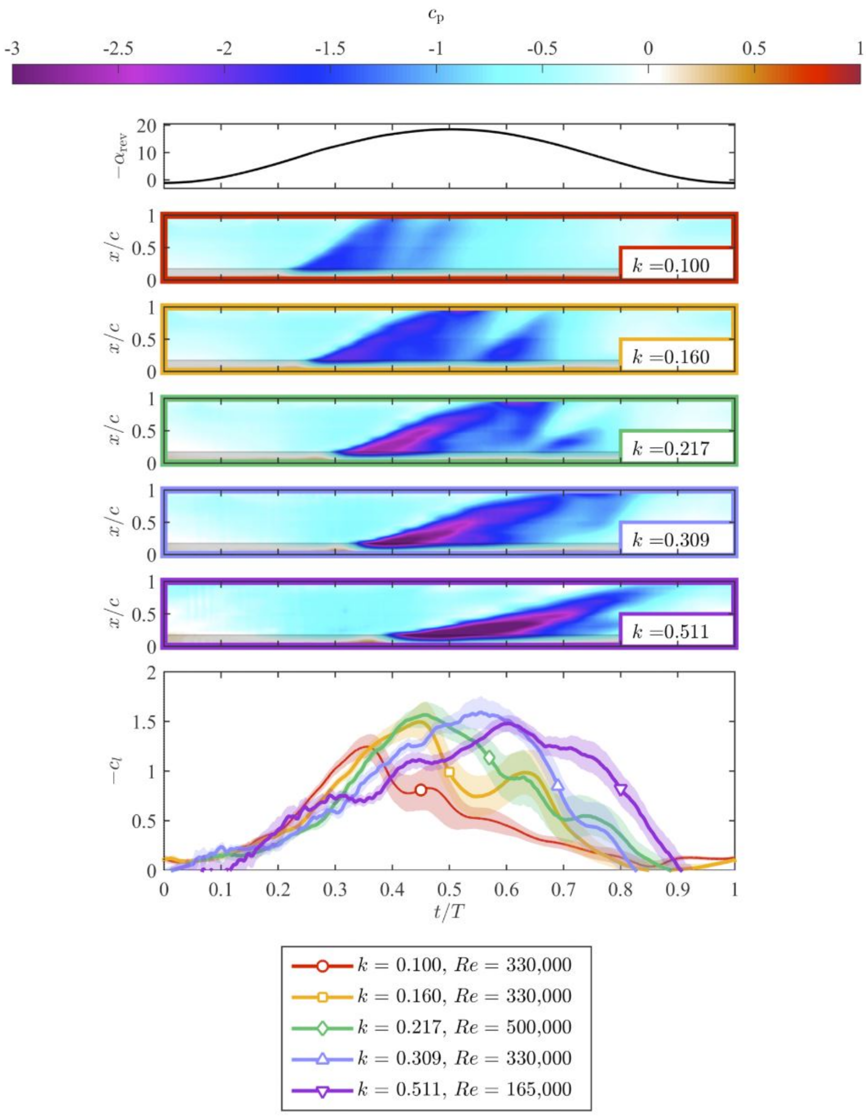

Figure 2.9: Reduced frequency effects on phase-averaged pressure distribution (suction side) and lift coefficient for a NACA 0012 with $\alpha_{m,rev} = -8.9°$, $\alpha_a = 9.9°$. [14]

Figure 2.10 also answers to a extremely interesting question from the modelling standpoint, the effect of the reduced frequency on the effective angle of attack. The effective angle of attack for reverse flow was calculated using the induced velocity at the leading edge ($w_{LE} = 0.75c\dot{\alpha}$) as:

$$-\alpha_{rev,eff} = -\alpha_{rev} + \tan^{-1}\left(\frac{w_{LE,z}}{U_\infty + w_{LE,x}}\right) \tag{2.1}$$

For the first half of the cycle the effective angle of attack decreases with the reduced frequency, with the difference reducing when approaching $t/T = 0.5$. This would suggest a delay in the dynamic stall onset, which is consistent with the results portrayed in Figure 2.9. The delay in the pressure wave initiation with increasing reduced frequency seems to indicate that the change in effective angle of attack is the cause of the delay in the dynamic stall onset [14].

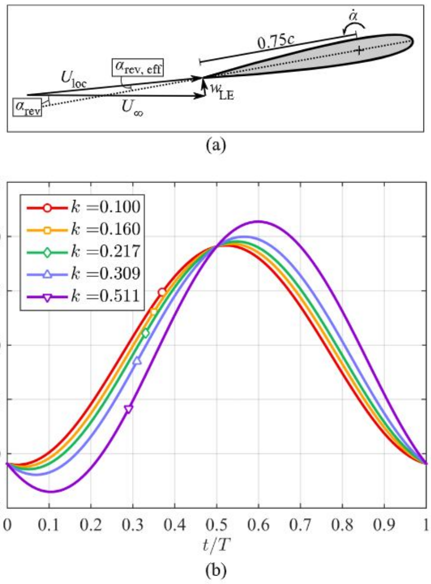

Figure 2.10: Analytical effective reverse flow angle of attack for a NACA 0012 with $\alpha_{m,rev} = -8.9°$, $\alpha_a = 9.9°$. (a) Sketch of airfoil and relevant angles. (b) Effective reverse flow angle of attack for several reduced frequency.[14]

Figure 2.11 studies the vortex strength and tracks of the PDSV. Figure 2.11 (a) shows that the PDSV remains closer to the blade for a longer part of the cycle as the reduced frequency increases. This is consistent with the expanded pressure distributions for the higher k showcased in Figure 2.9. Meanwhile, the vortex strength linearly increases with a lower slope when the reduced frequency is higher.

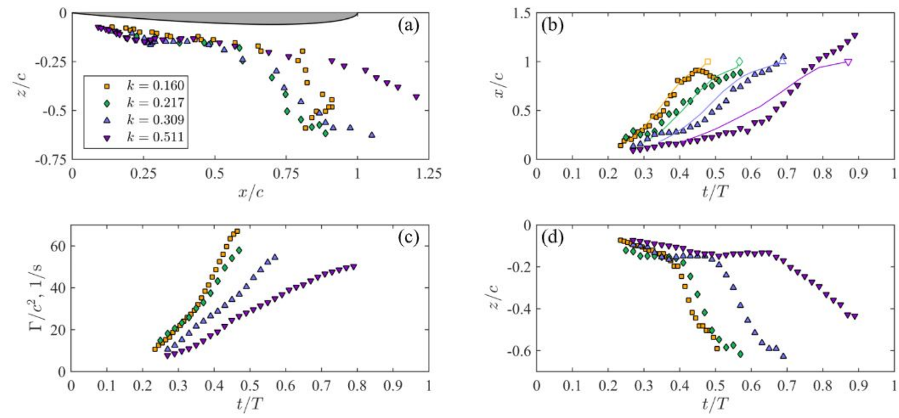

Figure 2.11: Reduced frequency effects on the evolution of the PDSV for a NACA 0012 with $\alpha_{m,rev} = -8.9°$, $\alpha_a = 9.9°$. (a) Blade-relative phase-averaged vortex tracks. (b) Vortex tracks (x-coordinate, symbols) and pressure waves (lines). (c) Primary dynamic stall vortex strength. (d) Vortex tracks (z-coordinate)[14]

In summary, the effect of reduced frequency on reverse flow dynamic stall is similar to classical dynamic stall. Firstly, the increase of reduced frequency keeps the main vortex responsible for reverse flow dynamic stall closer to the blade's surface for a longer period during each cycle. This causes a stronger suction near the front edge of the airfoil as the vortex grows in strength. Secondly, increasing reduced frequency means a reduced cycle time so that the primary dynamic stall vortex affects a larger portion of the cycle, even though the vortex convection speed moderately increases. This results in stretched-out pressure contours over the cycle and a broader peak of unsteady lift associated with the primary dynamic stall vortex. Lastly, the reduced frequency leads to a delay in the formation of the dynamic stall vortex. With higher reduced frequency, the effective angle of attack in reverse flow is lower during the first half of the cycle, so the stall angle is reached later in the cycle [14].

2.2.3. Mean pitch angle and pitch amplitude effect

The mean angle of attack (α_m) and pitching amplitude (α_a) greatly affect dynamic stall. In forward flow two types of dynamic stall were defined as a result, light and deep stall. Therefore, it can also be expected to have a significant effect in reverse flow. Different pitching cycles were tested for a reduced frequency $k = 0.160$ and a Reynolds number $Re = 3.3 \times 10^5$, as displayed in Figure 2.12. The different cases are also displayed in Table 2.1.

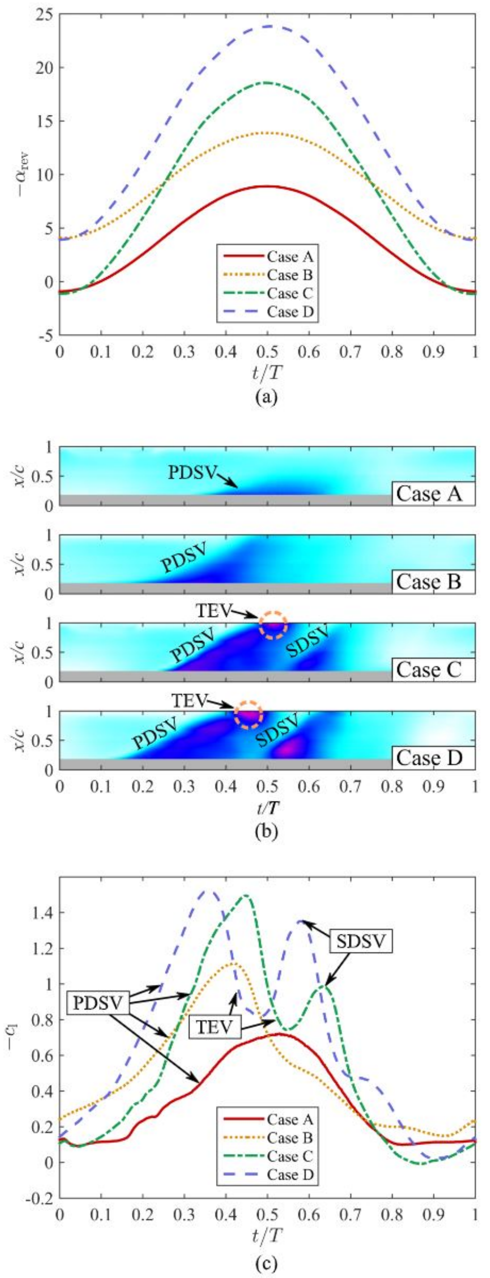

Figure 2.12: Pitch angle effects on reverse flow dynamic stall for a NACA 0012 with $k = 0.160$ and $Re = 3.3 \times 10^5$. (a) Angle of attack through the pitching cycle. (b) Phase-averaged pressure distribution (suction side). (c) Unsteady lift coefficient.[14]

While cases A and B generate a single vortex and therefore show a type I dynamic stall, both cases C and D lead to a dynamic III stall due to the larger pitch amplitude. Nevertheless, differences are still visible between both type I cases, for example case B produces a stronger vortex that forms earlier in the pitch cycle as the mean pitch angle is larger than in case A. Similarly, case D has a larger mean pitch angle than case C therefore, the dynamic stall onset in case D occurs earlier, and has a stronger trailing edge and secondary vortex than those of case C.

Case	$-\alpha_{m,rev}$ [deg]	α_a [deg]	$\|-\alpha_{rev,max}\|$ [deg]
A	4.1	4.9	9.0
B	9.1	4.9	14.0
C	8.9	9.9	18.8
D	14.1	10.0	24.1

Table 2.1: Pitching cycle case definition with $k = 0.160$ and $Re = 3.3 \times 10^5$. [14]

The pitch amplitude also has an effect on the reverse flow dynamic stall that can be observed from comparing cases A and B ($\alpha_a \approx 5°$) to cases C and D ($\alpha_a \approx 10°$). Cases with a greater amplitude (C and D) generate steeper lift coefficient curves during the formation of the PDSV. As coupling effects exist between the mean pitch angle and the pitch amplitude observing the effect of the maximum pitch angle can provide insight. Therefore, in Figure 2.13 shows the change in reverse flow dynamic stall type as a function of the reduced frequency as well as the maximum pitch angle. In addition, the values for the pitch amplitude and the studied cases (black dots) are also displayed.

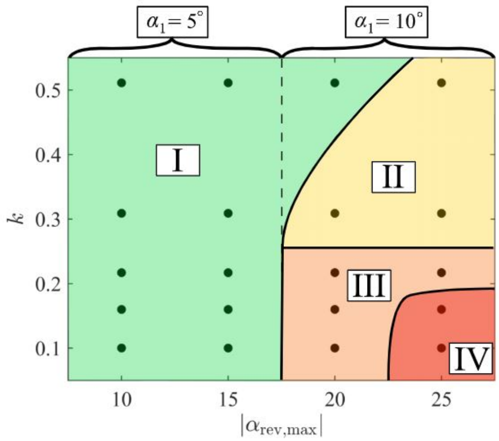

Figure 2.13: Dynamic stall type as a function of reduced frequency and maximum pitch angle.[14]

3
Dynamic Stall Modelling

The choice of the dynamic stall model and its parameters plays a crucial role in accurately predicting the load on a wind turbine. Hence, this section aims to examine several well-established dynamic stall models. The IStall2 [16] (Section 3.2) and Pierce [17] (Section 3.3) models have been used by GE to formulate their dynamic stall model. The presented models are all Beddoes-Leishman [18] type models, therefore, an overview of the Beddoes-Leishman model is presented first (Section 3.1). Although there are many other well-established models such as ONERA [19] [20][21] or Snel [22], these were disregarded as they use second order differential equations to represent vortex effects, and second order models were generating instabilities when tested with GE implemented models.

This chapter will provide an overview of the original Beddoes-Leishman (Section 3.1) to understand its complexity and limitations. It is important to pay special attention to its vortex effects implementation, as vortex generation and shedding is the most relevant flow phenomena in reverse flow dynamic stall, and its implementation will also be used in the IStall model 3.2) and minimally modified in Pierce's model 3.3). Both of these models aimed to expand the applicability of the Beddoes-Leishman model to the full $360°$ polar for wind turbine applications, while simplifying the original formulation, as compressibility effects are not significant in wind turbine applications. However, the model proposed by Sheng, Galbraith and Coton (Section 3.5), from now on referred to as "SGC", noted that the effect of weaker vortices could have been disregarded in the vortex effects formulation of the aforementioned models. Thus, it is interesting to explore their new formulation. Additionally, the GE2021 dynamic stall model (Section 3.4) will be introduced to assess possible improvements.

3.1. Beddoes-Leishman

The Beddoes-Leishman model is a semi-empirical model developed for dynamic stall in helicopter blades [18] and many adaptations have been developed, such as the one developed by Pierce (3.3) [17] aiming to simplify the model for wind turbine applications. In addition, it models the different occurring phenomena separately in different modules: attached flow, leading edge separation, trailing edge separation and dynamic stall.

3.1.1. Attached Flow

To model the attached flow behaviour a superposition of indicial aerodynamic responses is formulated. The indicial responses are the sum of a circulatory and a non-circulatory term. The non-circulatory term models the contribution from the airfoil's movement, and is calculated using a deficiency function D_n. A non-circulatory time constant ($T_I = c/a$) is defined using the chord (c) and the speed of sound (a), as well as a Mach number (M) dependent factor (K_α).

$$C^I_{N_n} = \frac{4K_\alpha T_I}{M}\left(\frac{\Delta\alpha_n}{\Delta t} - D_n\right) \tag{3.1}$$

$$D_n = D_{n-1}\exp\left(-\frac{\Delta t}{K_\alpha T_I}\right) + \left(\frac{\Delta\alpha_n - \Delta\alpha_{n-1}}{\Delta t}\right)\exp\left(-\frac{\Delta t}{2K_\alpha T_I}\right) \tag{3.2}$$

The circulatory contribution can be calculated to account for the circulatory loads generated by the wake.

$$C^C_{N_n} = C_{N_\alpha}(M)(\alpha_n - X_n - Y_n) = C_{N_\alpha}(M)\alpha_{E_n}$$

$$X_n = X_{n-1}\exp(-b_1\beta^2\Delta S) + A_1\Delta\alpha_n\exp(b_1\beta\Delta S/2) \tag{3.3}$$

$$Y_n = Y_{n-1}\exp(-b_2\beta^2\Delta S) + A_2\Delta\alpha_n\exp(b_2\beta\Delta S/2)$$

Where b_1 and b_2 are the time constants of the lag equations and A_1 and A_2 their respective coefficients. The time is non-dimensionalised using $S = \frac{2U_\infty t}{c}$. In addition, β^2 being $\beta = \sqrt{1-M^2}$ is used to account for compressibility effects. The effective angle of attack (α_{E_n}) can be calculated as $\alpha_{E_n} = \alpha_n - X_n - Y_n$. Thus, the total normal force coefficient ($C^p_{N_n}$) in attached flow conditions can be calculated as $C^p_{N_n} = C^I_{N_n} + C^C_{N_n}$. The chordwise ($C_{C_n}$) force coefficient is calculated, and can be simplified for small angles of attack, as $C_{C_n} = C_{N_n}\tan\alpha_{E_n} \approx C_{N_\alpha}(M)\alpha^2_{E_n}$.

3.1.2. Leading Edge Separation

One of the the most critical phenomena in dynamic stall is the leading edge separation. The onset criterion can be obtained from the studied airfoil's static data. The critical pressure for separation at the studied Mach number is obtained at $C_N(static) = C_{N_1}$, which corresponds to either the break in pitching moment or the chord force at stall. However, there is a lag in $C_N(t)$ that affects the pressure response at the leading edge with respect to $C_N(t)$, and therefore, the critical pressure is achieved at a higher value of C_N and consequently at a higher angle of attack.

In order to simplify this process, a first-order lag can be applied to C_N such that the onset of leading edge separation takes place when $C'_N(t)$ exceeds $C_{N_1}(M)$. In addition, $C'_N(t)$ can also be used to track flow reattachment, which would take place when $C'_N(t) < C_{N_1}(M)$.

$$C'_{N_n} = C_{N_n} - D_{p_n} \tag{3.4}$$

$$D_{p_n} = D_{p_{n-1}}\exp\left(-\frac{\Delta S}{T_p}\right) + (C^p_{N_n} - C^p_{N_{n-1}})\exp\left(-\frac{\Delta S}{2T_p}\right) \tag{3.5}$$

3.1.3. Trailing Edge Separation

Trailing edge separation is part of most types of dynamic stall, with progressive trailing edge separation causing circulation loss. The Beddoes-Leishman model uses a Kirchhoff equation to calculate the normal force coefficient during separation.

$$C_N = C_{N_\alpha}(M)\left(\frac{1+\sqrt{f_{stat}}}{2}\right)^2\alpha \tag{3.6}$$

Where C_{N_α} can be replied by 2π for incompressible flows. In addition, the trailing edge separation location f can be calculated as

$$f_{stat} = \begin{cases} 1 - 0.3\exp\left(\frac{\alpha-\alpha_1}{S_1}\right) & \text{if } \alpha \le \alpha_1 \\ \\ 0.04 + 0.66\exp\left(\frac{\alpha_1-\alpha}{S_2}\right) & \text{if } \alpha > \alpha_1 \end{cases} \tag{3.7}$$

S_1 and S_2 define the static stall characteristic while α_1 is the angle of attack corresponding to the breakpoint $f = 0.7$, and both can be computed from the airfoil static lift data at the corresponding Mach number.

However, an unsteady definition of the loading was defined in Equation 3.4, with which a new effective angle of attack can be defined as,

$$\alpha_f(t) = \frac{C'_N(t)}{C_{N_\alpha}(M)} \tag{3.8}$$

Using this newly defined α_f, a new effective separation point can be calculated using Equation 3.7, and its first-order lagged value (f'') can be computed using a Mach number dependent time costant (T_f).

$$f''_n = f'_n - D_{f_n} \tag{3.9}$$
$$D_{f_n} = D_{f_{n-1}} \exp\left(-\frac{\Delta S}{T_f}\right) + (f'_n - f'_{n-1}) \exp\left(-\frac{\Delta S}{2T_f}\right)$$

Therefore, the new computation of the normal and chordwise force coefficients can be formulated as,

$$C^f_{N_n} = C_{N_\alpha}(M)\left(\frac{1+\sqrt{f''_n}}{2}\right)^2 \alpha_{E_n} + C^I_{N_n} \tag{3.10}$$
$$C^f_{C_n} = \eta C_{N_\alpha} \alpha^2_{E_n} \sqrt{f''_n}$$

3.1.4. Dynamic Stall

The dynamic stall module aims to represent the effect of vortex on the unsteady loads of the airfoil. Vortex effects are onset when $C'_N > C_{N_1}$, and the vortex location is tracked using a nondimensional vortex time parameter (τ_v) such that $\tau_v = 0$ at the onset time, and $\tau_v = T_{vl}$ when the vortex reaches the trailing edge. A reset condition can be also applied so that multiple vortices can be modelled, $\tau_v = 0$ when the vortex reaches the trailing edge ($\tau_v = T_{vl}$) or after a Strouhal number related value such that $\tau_v = T_{vl} + T_{St}$.

$$T_{St} = \frac{2(1-f'')}{St} \tag{3.11}$$

The normal force coefficient for vortex effects can be computed using a vortex decay time constant (T_v) as follows,

$$C^v_{N_n} = C^v_{N_{n-1}} \exp\left(-\frac{\Delta S}{T_v}\right) + (C_{v_n} - C_{v_{n-1}}) \exp\left(-\frac{\Delta S}{2T_v}\right) \tag{3.12}$$

Where the increment in vortex lift (C_v) is determined using the difference between the unsteady circulatory lift and the corresponding unsteady nonlinear lift provided by the Kirchhoff approximation.

$$C_{v_n} = C^C_{N_n}(1 - K_{N_n}) \tag{3.13}$$

$$K_{N_n} = (1 + \sqrt{f''_n})^2/4 \tag{3.14}$$

It is interesting to mention that both T_v and T_{vl} were relatively Mach number independent, as well as insensitive to the airfoil shape, which is critical for wind turbine applications where a wide variety of flow conditions and airfoils are used in the same turbine blade.

3.2. IStall2

IStall2 or as previously called DYNSTALL, aimed to expand the Beddoes-Leishman model to the full $360°$ range of angles of attack [16]. The lift coefficient is calculated as an relation between the inviscid lift ($C_{L_{inv}}$) and the separation lift ($C_{L_{sep}}$). It also uses a rearranged version of the Kirchhoff separation equation so that the static separation point ($f_s tat$).

$$f_{stat} = \begin{cases} \left(2\sqrt{\frac{C_{L_{visc}}}{C_{L_{inv}}}} - 1\right)^2 & \text{if } |C_{L_{visc}}| \geq \frac{C_{L_\alpha}|\alpha-\alpha_0|}{4} \\ 0 & \text{if } |C_{L_{visc}}| < \frac{C_{L_\alpha}|\alpha-\alpha_0|}{4} \end{cases} \tag{3.15}$$

The C_{L_α} represents the lift coefficient slope at zero-lift at which the angle of attack is α_0 and $C_{L_{visc}}$ is the viscous lift coefficient. The inviscid lift $C_{L_{inv}}$ was computed as a piecewise combination of the linearlized lift coefficient equation up to a critical angle of attack ($\alpha_c = 30°$) and a sinusoidal curve:

$$C_{L_{inv}} = \begin{cases} C_{L_\alpha}(\alpha - \alpha_0) & \text{if } |\alpha| < \alpha_c \\ \frac{sin(d_1(\alpha-\alpha_0))}{d_1} + d_2 & \text{if } |\alpha| \geq \alpha_c \end{cases} \tag{3.16}$$

where $d_1 = 1.8$ and d_2 is used to ensure continuity at $|\alpha| = \alpha_c$,

$$d_2 = \begin{cases} C_{L_\alpha}\left(\alpha_c - \alpha_0 - \frac{sin(\alpha_c-\alpha_0)}{d1}\right) & \text{if } \alpha \geq \alpha_c \\ -C_{L_\alpha}\left(\alpha_c + \alpha_0 - \frac{sin(\alpha_c-\alpha_0)}{d1}\right) & \text{if } \alpha \leq -\alpha_c \end{cases} \tag{3.17}$$

However, some literature has pointed out that the equations in the DYNSTALL report might be faulty, as the addition of d_2 does not avoid the discontinuities at α_c [23]. The correct equations are believed to be

$$C_{L_{inv}} = \begin{cases} C_{L_\alpha}(\alpha - \alpha_0) & \text{if } |\alpha| < \alpha_c \\ \frac{C_{L_\alpha} sin(d_1(\alpha-\alpha_0))}{d_1} + d_2 & \text{if } |\alpha| \geq \alpha_c \end{cases} \tag{3.18}$$

$$d_2 = \begin{cases} C_{L_\alpha}\left(\alpha_c - \alpha_0 - \frac{sin(d_1(\alpha_c-\alpha_0))}{d1}\right) & \text{if } \alpha \geq \alpha_c \\ -C_{L_\alpha}\left(\alpha_c + \alpha_0 - \frac{sin(d_1(\alpha_c-\alpha_0))}{d1}\right) & \text{if } \alpha \leq -\alpha_c \end{cases} \tag{3.19}$$

The first order lag equation for the separation point is calculated using a non-dimensional time constant $\tau = f_\tau c/V_{rel}$, where $f_\tau = 4$ and V_{rel} is the relative velocity.

$$\frac{df}{dt} = -\frac{f_{dyn} - f_{stat}}{\tau} \tag{3.20}$$

which can be integrated and used to obtain f_{dyn_n} using the non-dimensional time $\Delta s = 2V_{rel}\Delta t/c$

$$f_{stat_n} - f_{dyn_n} = \left(f_{stat_{n-1}} - f_{dyn_{n-1}}\right) \exp\left(\frac{-\Delta s}{\tau}\right) + \left(f_{stat_{n-1}} - f_{stat_{n-1}}\right)\left(\frac{\tau}{\Delta s}\right) \exp\left(\frac{-\Delta s}{\tau}\right) \tag{3.21}$$

The separation lift can be calculated as

$$C_{L_{sep}} = \begin{cases} \frac{C_{L_{inv}}}{4} & \text{if } |C_{L_{stat}}| \geq \frac{C_{L\alpha}|\alpha-\alpha_0|}{4} \\ C_{L_{visc}} & \text{if } |C_{L_{stat}}| < \frac{C_{L\alpha}|\alpha-\alpha_0|}{4} \end{cases} \tag{3.22}$$

Therefore the dynamic lift and drag coefficients can be calculated as follows,

$$C_{L_{dyn}} = C_{L_{sep}} + \frac{C_{L_{inv}}(f_{dyn} + 2\sqrt{f_{dyn}})}{4} \tag{3.23}$$

$$C_{D_{dyn}} = C_{D_{stat}} + A_{cd}(C_{L_{visc}} - C_{L_{dyn}}) \tag{3.24}$$

Where the A_{cd} was determined for forward flow applications ($A_{cd} = 0.08$) and therefore, a new value might need to be searched for for reverse flow applications. Meanwhile, the vortex effect on the normal force coefficient is calculated as in the Beddoes-Leishman Model.

This model simplifies the Beddoes-Leishman model, disregarding compressibility effects as well as the formulation of attached and separated flows. This also reduces the number of flow and airfoil dependent constants throughout the whole process to just the ones necessary for vortex effects calculations, the critical angle of attack $\alpha_c = 30°$, $f_\tau = 4$ and A_{cd}, while as an example, the formulation of the separation point (Equation 3.7) uses three different coefficients that can be adapted depending on flow conditions as it can be seen in the SGC model (Equation 3.38).

3.3. Pierce

Pierce aimed to modify the Beddoes-Leishman model which, as previously mentioned in Section 3.1, considered angles of attack between $-10° \leq \alpha \leq 30°$, which do not cover wind turbines' operational range [17]. To begin, the angle of attack was modified (α_{mod}) (Figure 3.1) to compute the separation point such that,

$$\text{for} \begin{array}{ll} |\alpha| \leq 90° & \alpha_{mod} = \alpha \\ \alpha > 90° & \alpha_{\text{mod}} = 180° - \alpha \\ \alpha < -90° & \alpha_{\text{mod}} = -180° - \alpha \end{array} \tag{3.25}$$

The Beddoes-Leishman employed an exponential curve fitting approach to estimate the effective separation point based on static data. However, this method proved to be ineffective for certain airfoils that were tested, which is inconvenient for wind turbine applications.

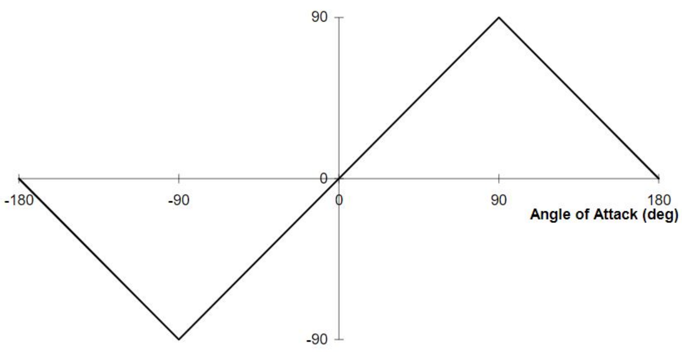

Figure 3.1: Modified angle of attack α_{mod} [17].

In addition, at certain angles of attack, the square root of the separation point in Equation 3.6 needs to be negative in order to replicate the values of the static aerodynamic coefficients. To avoid this, the normal coefficient was then computed as

$$q = 4\sqrt{\frac{C_{N_{stat}}}{C_{N_\alpha}(\alpha - \alpha_0)}} - 1$$
$$f = q^2 sign(q) \tag{3.26}$$

$$C_N = C_{N_\alpha}(\alpha - \alpha_0)\left(\frac{1 + sign(f)\sqrt{|f|}}{2}\right)^2 \tag{3.27}$$

Similarly, the chordwise force coefficient can be calculated as

$$q_C = \frac{C_C}{C_{N_\alpha}(\alpha - \alpha_0)\alpha}$$
$$f_C = q_C^2 sign(q_C) \tag{3.28}$$

$$C_C = C_{N_\alpha}(\alpha - \alpha_0)\alpha\sqrt{|f_C|}sign(f_C) \tag{3.29}$$

The last modification comes from the vortex effect on the chordwise force coefficient, disregarded in the Beddoes-Leishman model. The vortex contribution was computed adding the product of C_N^v and $(1 - \tau_v)$ to the C_C .

Pierce's model simplifies the Beddoes-Leishman model while improving the calculation of the separation point. However, it was only validated for a low range of reduced frequencies ($k < 0.1$).

3.4. GE2021

The denominated "GE2021" model is to remain confidential and will therefore only be made available to the TU Delft graduate supervisor and examiners, who can find the relevant information in Appendix GE2021.

3.5. SGC

As previously discussed in Section 3.1, the Beddoes-Leishman model was developed for helicopter rotors. These operate at high Mach numbers to which wind turbines are not exposed. This results in inaccuracies in the stall onset prediction, as well as the negative chordwise force representation. In addition, the stalled flow convection over the upper surface of the airfoil and into the freestream is disregarded during the return phase. Thus, this new model proposed by Sheng, Galbraith and Coton, denominated SGC, includes modifications such as a new stall onset criterion [24], a new return modelling [25], a new formulation of the chordwise force coefficient and a revision of the vortex formation and convection modelling [26].

3.5.1. Forcing

Similarly to the Beddoes-Leishman model, airloads are computed using indicial functions. To offer a more generic approach, forcing terms are expressed in terms of lift and pitching moment instead of angle of attack and pitch rate in both circulatory (η_N) and impulsive (noncirculatory) contributions (λ_N).

$$\eta_N(t) = \frac{1}{\pi}\int_0^{\pi}(1+\cos\theta)\frac{w_a(\theta,t)}{V}d\theta$$

$$\Delta\lambda_N(t) = \frac{1}{2}\int_{-1}^{1}\frac{\Delta w_a\left(x^*,t\right)}{V}dx^* \tag{3.30}$$

using the boundary condition

$$w_a(x,t) \equiv \frac{\partial z_a(x,t)}{\partial t} + V\frac{\partial z_a(x,t)}{\partial x} \tag{3.31}$$

In the case of a pure pitching motion around the $c/4$ axis,

$$w_a = V\alpha + \frac{c}{2}\dot{\alpha} \tag{3.32}$$

3.5.2. Attached Flow

To compute attached flow airloads induced by a step change in the forcing term, the circulatory normal force is,

$$\Delta C_N^C(s) = C_{N_\alpha}\Delta\eta_N(1 - A_1e^{-b_1s} - A_2e^{-b_2s} - A_3e^{-b_3s}) \tag{3.33}$$

and its impulsive counterpart

$$\Delta C_N^I(s) = \Delta\lambda_N\frac{4}{M}e^{-s/T_I} \tag{3.34}$$

3.5.3. Separated Flow

The effect on airloads of the trailing edge separation are calculated in the same way as the Beddoes-Leishman model,

$$C_N = C_{N_\alpha}(\alpha - \alpha_0)\left(\frac{1+\sqrt{f''}}{2}\right)^2 \tag{3.35}$$

While the chordwise force coefficient a term E_0 is added,

$$C_C = \eta C_{N_\alpha}(\alpha-\alpha_0)^2(\sqrt{f''} - E_0) \tag{3.36}$$

For most NACA airfoils can be assumed to be $E_0 = 0.2$.

The effective angle of attack is however computed differently using a time delay constant T_α [27] [24],

$$\Delta\alpha'(s) = \Delta\alpha(s)(1 - e^{-s/T_\alpha}) \tag{3.37}$$

The coefficients used in the Beddoes-Leishmann model (Equation 3.7) are modified, and the separation breakpoint at $f = 0.7$ (α_1) and the angle of attack shift ($\Delta\alpha_1$) are used to compute the new separation point.

$$f'(\alpha) = \begin{cases} 1 - 0.4\exp\left(\frac{\alpha'-\alpha_1-\Delta\alpha_1}{S_1}\right) & \text{if } \alpha' \leq \alpha_1 \\ 0.02 - 0.58\exp\left(\frac{-\alpha'+\alpha_1+\Delta\alpha_1}{S_2}\right) & \text{if } \alpha' > \alpha_1 \end{cases} \tag{3.38}$$

3.5.4. Stall-Onset

Dynamic stall onset linearly increases with the reduced pitch rate when the reduced pitch rate is larger than a certain r_0 ($r_0 = 0.01$ for most NACA series)[28][24][27][29].

The constant critical stall-onset angle of attack (α_{ds0}) can be obtained from fitting using the least square methods using ramp-up data. Stall will take place when $\alpha' \geq \alpha_{cr}$

$$\alpha_{cr} = \begin{cases} \alpha_{ds0} & \text{if } r \geq r_0 \\ \alpha_{ss} + (\alpha_{ds0} - \alpha_{ss})\frac{r}{r_0} & \text{if } r < r_0 \end{cases} \tag{3.39}$$

The angle shift from the static stall onset angle of attack, $\Delta\alpha_1$, can be calculated

$$\Delta\alpha_1 = \begin{cases} \alpha_{ds0} - \alpha_{ss} & \text{if } r \geq r_0 \\ (\alpha_{ds0} - \alpha_{ss})\frac{r}{r_0} & \text{if } r < r_0 \end{cases} \tag{3.40}$$

3.5.5. Dynamic Vortex

When dynamic stall is onset, an overshoot in normal force is expected, but for the studied cases with low Mach numbers, an additional increase in C_N is observed after stall initiation. This is caused due to the shear layer retantion above the airfoil surface as a dynamic stall vortex and its convection. Although modifications were introduced by Leishman, this are still insufficient when the vortex is not strong enough. Therefore, a new formulation of the vortex formation and convection was formulated, taking into account the following physical phenomena.

As the vortex forms and separates from the leading-edge region, it causes an increase in normal force, giving the impression that the flow is still attached to the upper surface. To account for this effect, a further delay in the boundary separation location can be considered.

At low Mach numbers, there is an additional surge in normal force due to the vortex moving across the chord. This extra normal force is assumed to be proportional to the difference between the delayed separation location and its corresponding value in the steady state [30].

The convection of the vortex over the chord and the resulting movement of the pressure center causes a significant nose-down pitching moment. Its magnitude is directly proportional to the normal force generated by the vortex, and its position can be tracked similarly to the Beddoes-Leishmann model [18].

The additional delay in separation location can be computed as

$$\Delta f''(s) = \Delta f'(s)(1 - e^{-s/T_v}) \tag{3.41}$$

Vortex shedding is calculated following a formulation proposed by Beddoes [30], depending on the vortex location (τ), being T_v the time constant of vortex traveling over chord and T_{VL} the vortex passage time constant.

$$V_x = \begin{cases} \sin^{3/2}\left(\frac{\pi\tau}{2T_v}\right) & \text{if } 0 < \tau < T_v \\ \cos^2\left(\frac{\pi(\tau - T_v)}{T_{VL}}\right) & \text{if } \tau > T_v \end{cases} \tag{3.42}$$

Therefore, the normal force coefficient induced by the dynamic stall vortex can be defined using a B_1 an airfoil dependent coefficient as,

$$\Delta C_{N_v} = B_1\left(f'' - f\right) \times V_x \tag{3.43}$$

A similar approach was considered by dos Santos and Marques [31] using the following formulation for the first DSV,

$$\left(\sin\left(\frac{\pi t_v}{2T_{v_{L1}}}\right)\right)^{(\mu_2+R'_{tv1})} \text{ if } 0<\tau<T_{v_{L1}} \qquad 0 \text{ otherwise} \tag{3.44}$$

and the following for the second and third vortices respectively,

$$V_{x_2}=\begin{cases}\frac{1}{2}\left\{1-\cos\left[\pi\left(\frac{t_v-g_vT_{v_L}}{T_{v_{l2}}}\right)\right]\right\} & \text{if } t_v>g_vT_{v_L} \text{ and } t_v\leq g_vT_{v_L}+2T_{v_{L2}}\\ 0 & \text{otherwise}\end{cases}$$

$$V_{x_3}=\begin{cases}\frac{1}{2}\left\{1-\cos\left[2\pi\left(\frac{t_v-g_vT_{v_L}-T_{v_L}/2}{3T_{v_{L2}}}\right)\right]\right\} & \text{if } t_v>g_vT_{v_L}+T_{v_{L2}}/2 \text{ and } t_v\leq g_vT_{v_L}+7T_{v_{L2}}/2\\ 0 & \text{otherwise}\end{cases} \tag{3.45}$$

The model presented by dos Santos and Marques [31] uses different formulations for the first, second and third vortex shed, with specific coefficients and constants for each one of them. This increases the model's complexity as these constants and coefficients are Mach and airfoil dependent, making it almost difficult to utilize in HAWT applications.

3.5.6. Return

Two different phenomena have been proved critical to the return from stall to attached flow: the convection over the upper side of the airfoil of the stalled flow, and the reestablishment of the boundary layer. The angle of attack at the onset of the convection process (α_{min0}) is used to compute the angle of attack at which the C_N has a local minimum (α_{min}) using a delay constant T_r.

$$\alpha_{min}=\alpha_{min0}+T_r r \tag{3.46}$$

After analyzing several possible dynamic stall modelling techniques throughout this chapter, and the better understanding gained of the flow physics of reverse flow dynamic stall in Chapter 2, a clear research gap was found. The research scope for this project is proposed in the next Chapter.

4 Research Scope

Dynamic stall has been thoroughly researched for over forty years. However, models have always been validated in a limited range of angles of attack ($-10^\circ \leq \alpha \leq 35^\circ$) while HAWTs operate at rapidly changing angles of attack that vary throughout the blade, including reverse flows. Therefore, there is a clear knowledge gap, as only a single abstract, but no paper or report, about reverse flow dynamic stall modelling has been published.

In the specific case of the GE2021 model, the results presented in Section 3.4 show that the currently implemented formulation that neglects vortex effects in not able of capturing the nature of reverse flow dynamic stall. Being the GE2021 a Beddoes-Leishman type model, and knowing second order modelling techniques have caused instabilities when combined with other GE simulation algorithms, it is important to assess the performance of the two types of vortex effects modelling options presented in Chapter 3.

The first modelling technique would be the one in the original Beddoes-Leishman model, similarly implemented in the IStall2 and Pierce model. The second, would be the sinusoidal implementation presented by Sheng, Gal (SGC), using Beddoes' formulation [30], which aims to include the effects of weaker vortices and better represent deep dynamic stall.

However, the limitations of studying the possible modelling techniques for reverse flow dynamic stall reside in the limited validation data that is available at the moment. For HAWTs, multiple airfoils are used in a single blade, making Lind's research somewhat limited [14] [12], as the reverse flow dynamic stall testing focuses on a NACA 0012, a symmetric thin airfoil, while HAWTs use a wide variety of airfoils of different thickness and shapes. Nevertheless, this research brings extremely valuable insight about the effects of the Reynolds number, reduced frequency, mean pitch angle and pitch amplitude, that can be a good start to approach the very much under-researched reverse flow dynamic stall.

Therefore, several research questions can be formulated:

- To what extent are the Beddoes-Leishman model and other models derived from it, suitable for effectively addressing the modelling challenges associated with reverse flow dynamic stall in the context of wind turbine applications?
  - Considering that the vortex effects in reverse flow dynamic stall are initiated at lower angles of attack due to the presence of a sharp aerodynamic leading edge, does the application of the Beddoes-Leishman vortex onset condition remains appropriate, or are different considerations such as a critical angle of attack, necessary to adequately define a vortex effect onset condition?
  - In light of the discernible disparities in vortex convection speed between forward and re-

verse flow dynamic stall phenomena, what adjustments of the relevant time constants are necessary when modelling reverse flow dynamic stall and vortex convection speed to ensure accurate representation of both conditions?

- Considering the great impact of vortex generation and convection in reverse flow dynamic stall, could the modelling of separation and vortex effects alone potentially serve as an adequate representation of reverse flow dynamic stall? What other phenomena would be necessary to more reliably model reverse flow dynamic stall?
- Being the SGC a modification of the Beddoes-Leishman model proposed by Sheng, Galbraith and Coton aiming to account for the effects of weaker vortices in deep stall, and knowing there is a strong similarity in flow behavior between forward flow deep dynamic stall and reverse flow dynamic stall, could the SGC model provide a more precise representation of reverse flow dynamic stall when compared to a conventional Beddoes-Leishman type model?
  - Among the approaches presented in the existing literature, is utilizing a deficiency function a suitable method for modeling vortex-generated loading? Additionally, should alternative approaches, such as employing a sinusoidal curve, be considered to accurately represent the vortex effects associated with reverse flow dynamic stall?
  - Is a great number of airfoil dependent constants and coefficients necessary to represent the vortex generated effects in reverse flow dynamic stall when implementing the vortex shedding formulation proposed by Beddoes [30] and implemented by Sheng, Galbraith and Coton in the SGC model?

The forthcoming MSc. Thesis will address these research questions by investigating the effectiveness of current dynamic stall modelling techniques under reverse flow conditions, while aiming to improve General Electric's dynamic stall model's performance in reverse flow conditions. Additionally, this study aims to evaluate the applicability of these techniques while ensuring computational efficiency and to determining their suitability to the wind energy sector, where a wide variety of airfoils and angles of attack are encountered.

5

Analysis of Established Models

Chapter 3 offered an overview of several dynamic stall models. An analysis of the performance of these models in reverse flow conditions is necessary to properly assess their potential to model this complex flow phenomena. To perform this analysis, GE2021 [23], an existing implementation of the model proposed by Pierce [17] and an interpretation of the denominated SGC model [26] developed by dos Santos and Marques [32], will be used to model some of the reverse flow dynamic stall cases available in the literature. The generated by these formulations will be compared with the experimental results obtained by Lind [14]. The defining parameters of the four available cases are described in Table 2.1.

Case	$-\alpha_{m,rev}$ [deg]		α_a [deg]		$\lvert -\alpha_{rev,max}\rvert$ [deg]		k [-]
	Lind (2016)	Modelled	Lind (2016)	Modelled	Lind (2016)	Modelled	
A	4.1	5	4.9	5	9.0	10	0.160
B	9.1	10	4.9	5	14.0	15	0.160
C	8.9	10	9.9	10	18.8	20	0.160
D	14.1	15	10.0	10	24.1	25	0.160
E	8.9	10	9.9	10	18.8	20	0.100
F	8.9	10	9.9	10	18.8	20	0.309

Table 5.1: Lind (2016) [14] and Modelled cases.

These experimental cases conducted by Lind showcased varying offsets with the intended simulated pitching motions, that were attributed to a calibration issue [14]. However, it was not possible to incorporate these offsets into the modelling of these cases. Consequently, there will be a disparity between the angles of attack presented by Lind (2016) and those modelled in this study. These offsets are minor and are not expected to have a significant impact. The parameters for the modelled cases were also included in Table 5.1. Cases A, B, C and D are also collected in Table 2.1. Cases E and F account for the first and fourth case displayed in Figure 2.9 respectively.

Although the influence of Reynolds number on reverse flow dynamic stall development has been found to be negligible, only cases with the same Reynolds number as Cases A, B, C, and D were considered, with Case C also being the second case depicted in Figure 2.9.

Cases C, E and F have the same mean angle of attack and pitching amplitude but different reduced frequencies and are therefore interesting to study as they provide insight about the capabilities the different models have to represent the delay observed with increasing reduced frequency (Figure 2.9). Figure 5.1 shows the results obtained for the modelling of the aforementioned cases. When modelling reverse flow dynamic stall using the SGC model, the obtained lift coefficient distribution varies around

$-C_L \approx 6.5$. The magnitude of these results is over three times higher than those obtained in the experiments developed by Lind [14]. The results obtained using the dynamic stall model proposed by Pierce and the GE2021 model yield results that are more representative of the reality of reverse flow dynamic stall. This overestimation using the SGC model is common to all the studied cases. Therefore, to ensure a proper analysis and visualization, these results will be studied separately from the ones produced by GE2021 or Pierce.

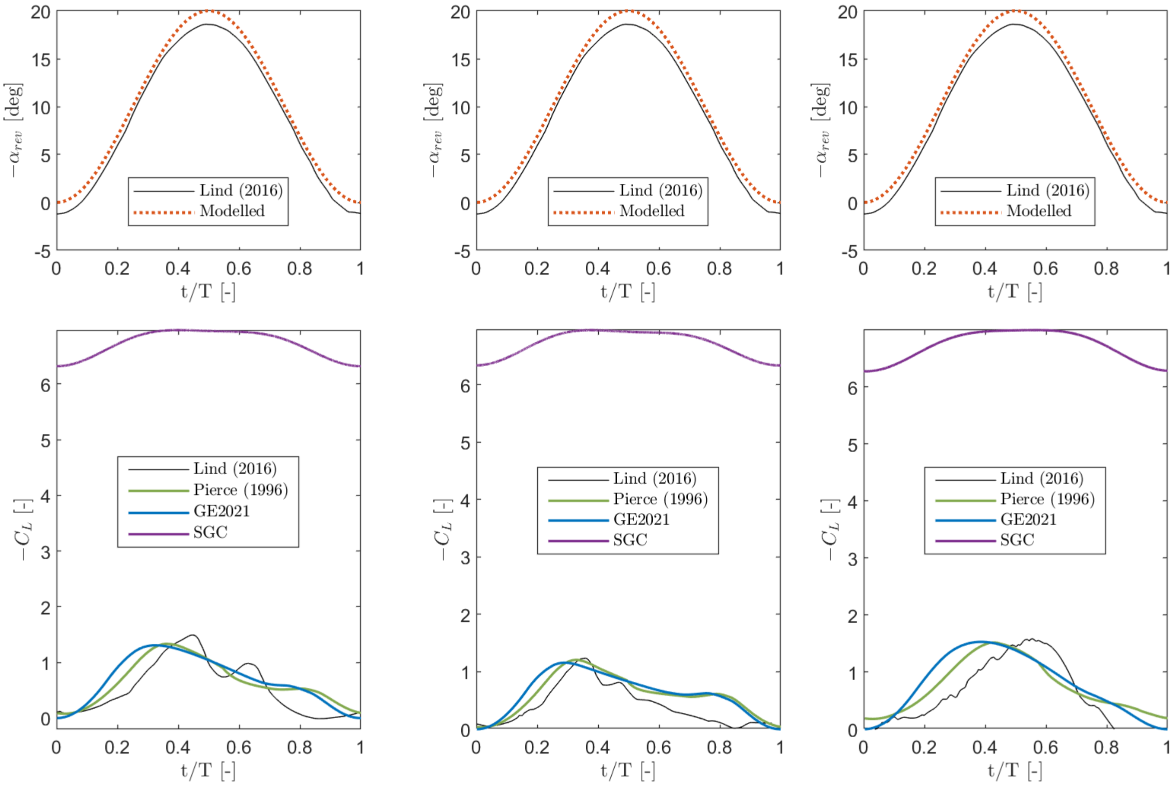

(a) Case C. **(b)** Case E. **(c)** Case F.

Figure 5.1: Angle of attack and $-C_L$ distributions obtained using different dynamic stall models compared to the experimental results from Lind (2016) [14].

Figure 5.2 focuses on the results provided by Pierce and GE2021 model. GE2021 is a simplified Beddoes-Leishman model and does not account for vortex effects. Therefore, it is not surprising that the peaks in $-C_L$ found in the experimental data that originate due to vortex effects are not properly represented for these cases. However, it is interesting to draw a relation between both models and to show their similarities.

Figures 5.2b and 5.2a show cases with $k = 0.160$ and $k = 0.100$ respectively. As observed in the literature, increasing reduced frequency delays the vortex onset, and creates an stretching visual effect that occurs because the vortex affects a longer portion of the shorter pitching cycle. Both models are able to moderately capture the delay of the first peak. However, Table 5.2 evidences that the obtained delay is not sufficient to accurately represent reverse flow dynamic stall. Table 5.3 includes the relative portion of the cycle between the peaks depending on the reduced frequency.

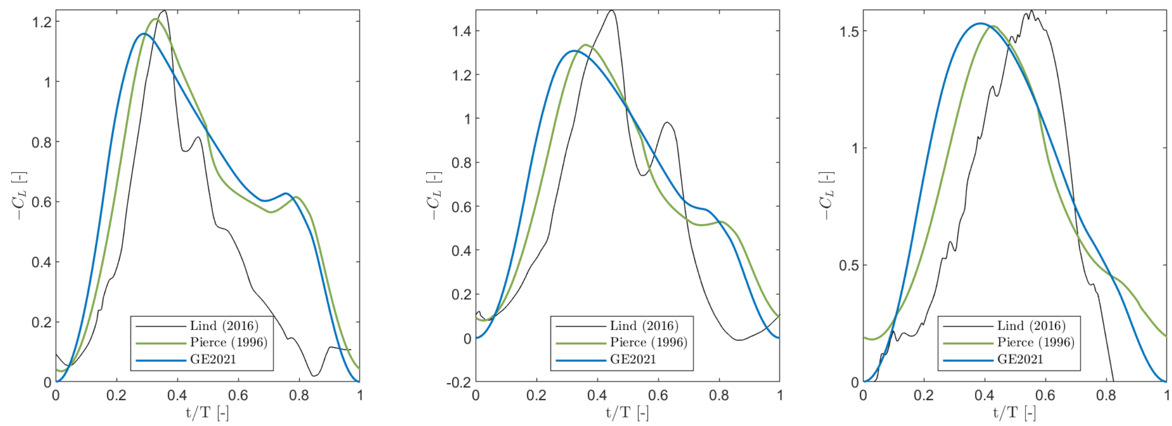

(a) Case E ($k = 0.100$). **(b)** Case C ($k = 0.160$). **(c)** Case F ($k = 0.309$).

Figure 5.2: $-C_L$ distributions obtained using Pierce and GE2021, compared to the experimental results from Lind (2016) [14].

Experimental data shows that the delay between the first peaks when the reduced frequency is $k = 0.160$ relative to the case where $k = 0.100$, is approximately of 25%. The delay between the first peaks when the reduced frequency is $k = 0.309$ relative to the case where $k = 0.100$ is approximately of 52.8%. However, the delay between the first peaks when the reduced frequency is $k = 0.309$ relative to the case where $k = 0.160$ is approximately of 22% which is close to the delay modelled using GE2021. Both the Pierce and GE2021 models exhibit limitations in accurately capturing the delay caused by the increasing reduced frequency.

	Case E ($k = 0.100$)	Case C ($k = 0.160$)	Case F ($k = 0.309$)
Pierce	0.32	0.37	0.43
GE2021	0.29	0.32	0.39
Lind (2016)	0.36	0.45	0.55

Table 5.2: Approximate t/T for which the first peak occurs using Pierce and GE2021 for the cases with different reduced frequencies.

	Relative Increase in t/T comparing case C to E [%]	Relative Increase in t/T comparing case F to E [%]	Relative Increase in t/T comparing case F to C [%]
Pierce	15.6	34.4	16.2
GE2021	10.3	34.5	21.9
Lind (2016)	25	52.8	22.2

Table 5.3: Approximate relative increase in t/T for which the first peak occurs using Pierce and GE2021 for the cases with different reduced frequencies.

Figure 5.3 is displayed to better assess the representation of delay caused by the increasing reduced frequency obtained using Pierce and GE2021. Although delays in the location of the peaks are visible in Figure 5.2, experimental results also show a slower growing $-C_L$ with increasing reduced frequency. Meanwhile, the results obtained using GE2021 all have the same slope and those obtained using Pierce do offer a slight decrease in growth rate.

However, it is worth to note that a partial representation of the delay is achieved, which is generally acceptable considering the inherent limitations of modelling processes. In addition, the growing magnitude of the first peak with reduced frequency is also partially captured with Pierce and GE2021. Although the discrepancies are most notable for Case C, $k = 0.160$, which is the reduced frequency used for the rest of the cases.

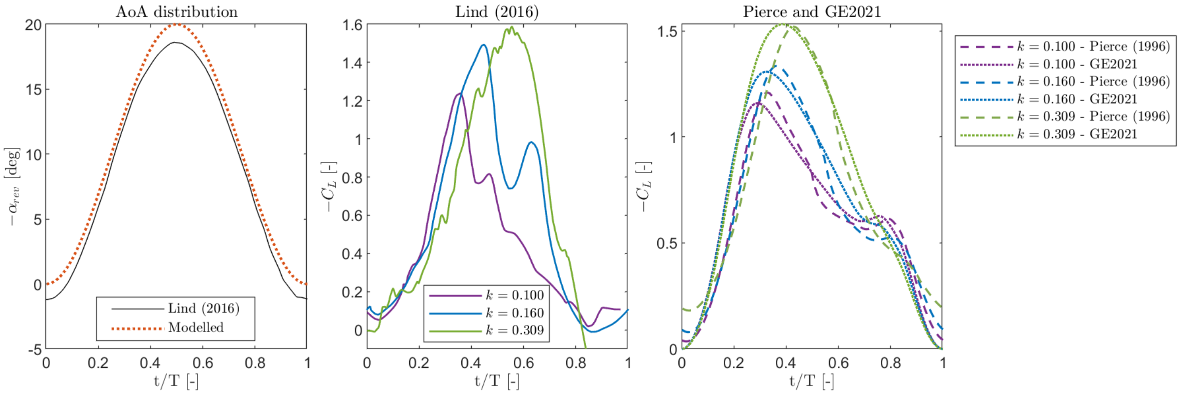

Figure 5.3: Angle of attack and $-C_L$ distributions obtained using the model proposed by Pierce and GE2021 compared to the experimental results from Lind (2016) [14].

Using Cases E and C, it is also possible to discern what behaviours can be possibly attributed to separation or vortex effects. Acknowledging that the GE2021 does not account for vortex effects, the second peaks at $t/T \approx 0.8$ in Figures 5.2a and 5.2c, it becomes clear that these are caused by the separation effect modelling. Sharing GE2021 common traits with both Pierce and IStall2 models, it can be assumed that the second peaks resulting from the Pierce modelling are also caused my separation effects, not by vortex effects.

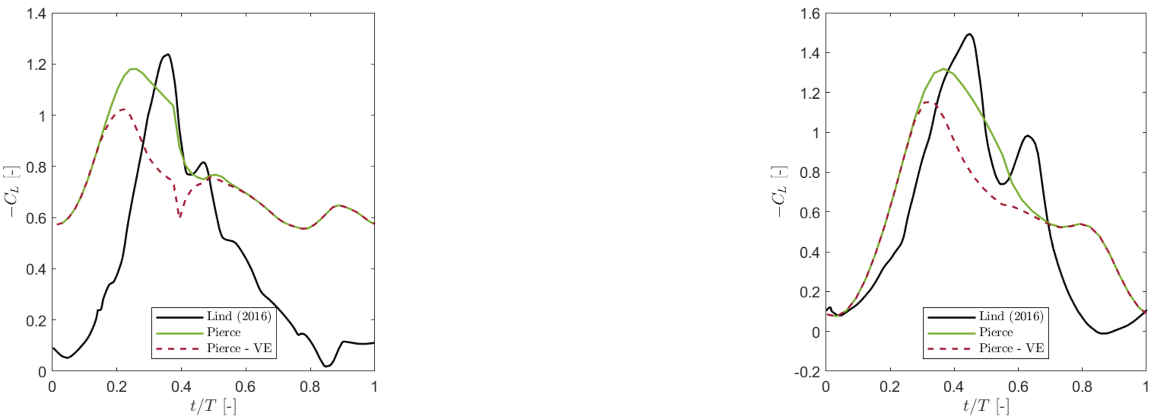

(a) Case E ($k = 0.100$).

(b) Case C ($k = 0.160$).

Figure 5.4: $-C_L$ distributions obtained using Pierce and Pierce with no vortex effects, compared to the experimental results from Lind (2016) [14].

However, this can be verified observing Figure 5.4, which shows the results generated by the Pierce implementation, and the Pierce implementation without vortex effects ("Pierce - VE"). These clearly prove the secondary peak at around $t/T \approx 0.8$ is a result of separation effects.Therefore, it can be concluded that contrary to what can be observed from the empirical data, a single vortex structure is modelled. Thus, the formulation of vortex effects implemented by Pierce does not seem effectively capture the vortex generation in reverse flow dynamic stall.

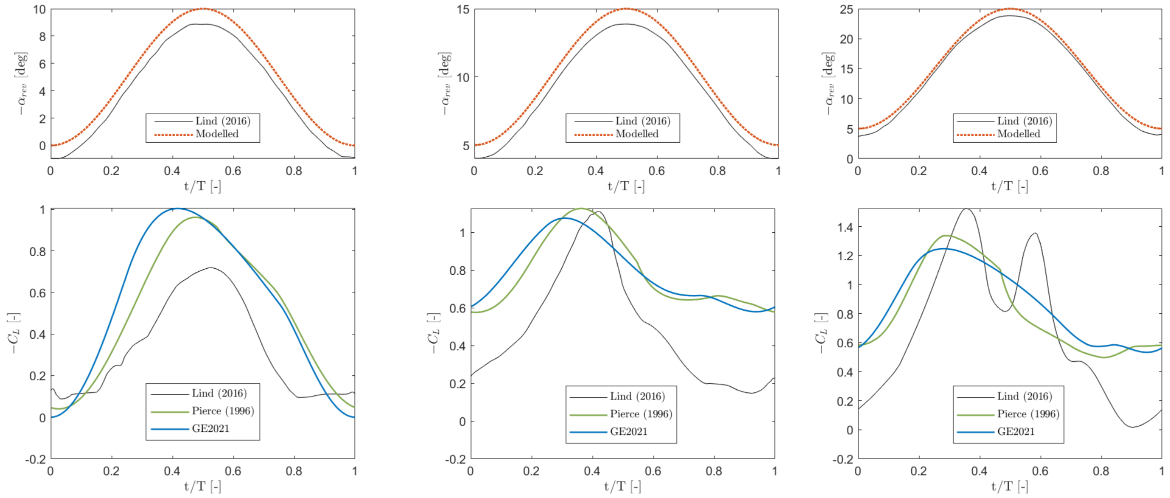

(a) Case A. **(b)** Case B. **(c)** Case D.

Figure 5.5: Angle of attack and $-C_L$ distributions obtained using Pierce and GE2021, compared to the experimental results from Lind (2016) [14].

In addition to the previous remarks, it is also crucial to pay further attention to Cases B and D, which display values of $-C_L$ almost triple to those observed in the empirical data for angles of attack close to $-\alpha_{rev} \approx 5°$. After further examination, it was concluded that this discrepancy roots on the use of the static polar to determine the inviscid lift, and consequently the separation lift. Figure 5.6 showcases the values for the inviscid lift at $-\alpha_{rev} \approx 5°$, where the flow remains mostly attached. For Cases B and D these discrepancies between the modelled results and the empirical data will remain a limitation throughout the study.

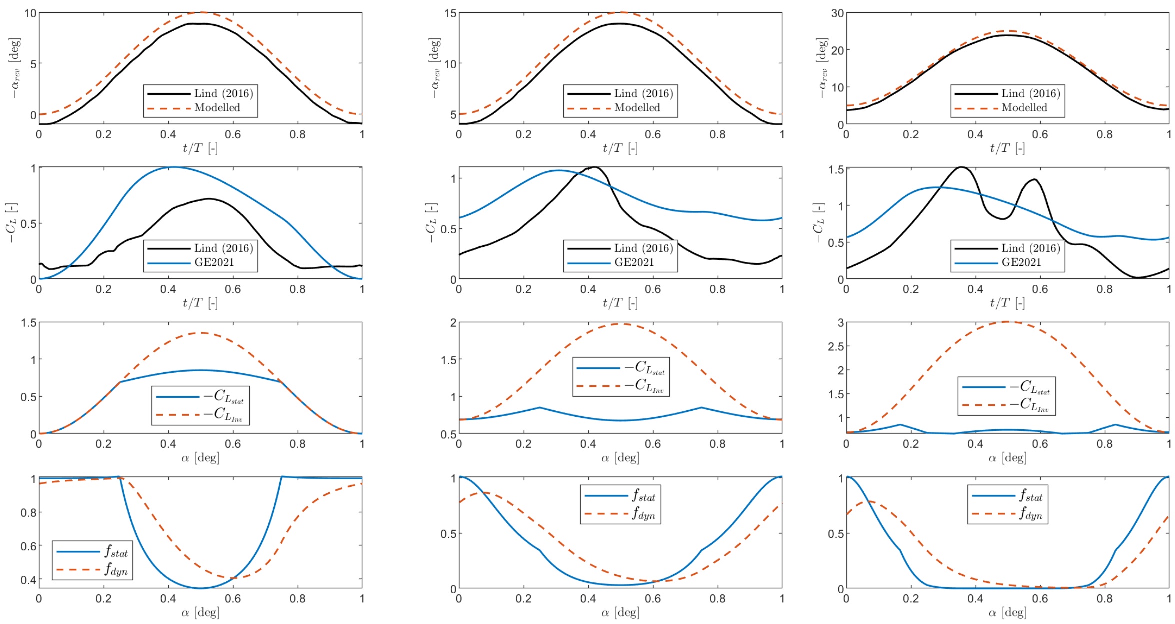

(a) Case A. **(b)** Case B. **(c)** Case D.

Figure 5.6: Angle of attack and $-C_L$ distributions obtained using GE2021, compared to the experimental results from Lind (2016) [14]. $-C_{L_{stat}}$ and $-C_{L_{stat}}$, and separation point f_{stat} and f_{dyn} distributions of obtained with GE2021.

Figure 5.5, showcases the other cases with reduced frequency $k = 0.160$ which have varying mean angles of attack and amplitudes, as displayed in Table 2.1. Cases C (Figure 5.2b) and D (Figure 5.5c) have a higher maximum angle of attack which, as supported by the experimental results, allows for the formation of multiple dynamic stall vortices. The formulation proposed by Pierce shows a concave vortex decay that help match the lift decay rate after the first peak, while ignoring the second peak. These vortices are not properly captured by Pierce's formulation, which follows the Beddoes-Leishman formulation for vortex effects, for which the magnitude is not sufficient for some of the studied cases, and excessive in others, and is not able to represent the several vortices generated during the pitching motion.

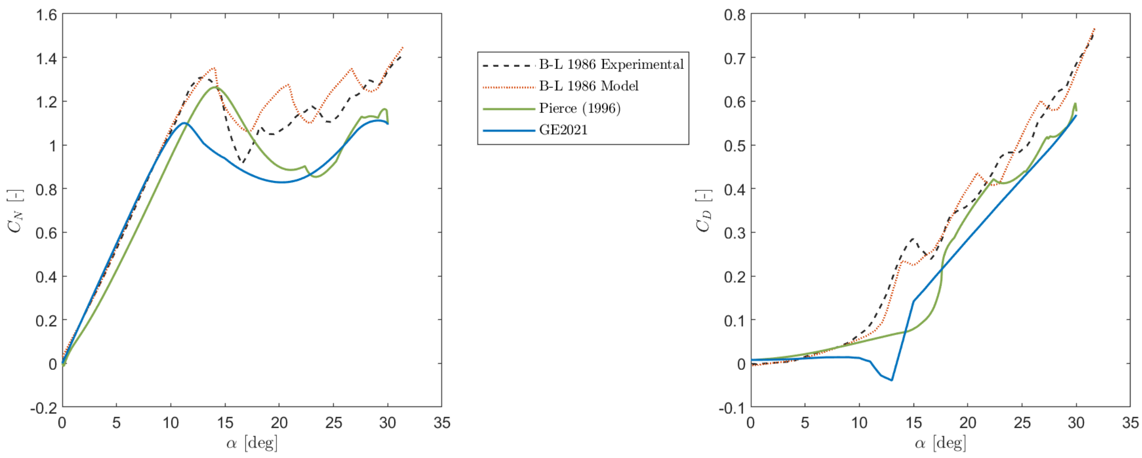

Figure 5.7: C_N for $M = 0.496$ and $\omega = 1493 deg/s$ using data from the Beddoes-Leishman [18], the Pierce and the GE2021.

Figures 5.7 and 5.8, showcase the results of two ramp-up cases, comparing the loads computed by Beddoes and Leishman [18], as well as the experimental data used to validate their model, with Pierce and GE2021. From these Figures, it becomes clear that none of these models are able to capture the stabilization at higher angle of attack, with a slow increase in C_N and the oscillatory nature most probably generated by the vortex structures. The Beddoes-Leishman model is able to capture the slower but steady increase in C_N while simulating the oscillatory trend around the growing C_N.

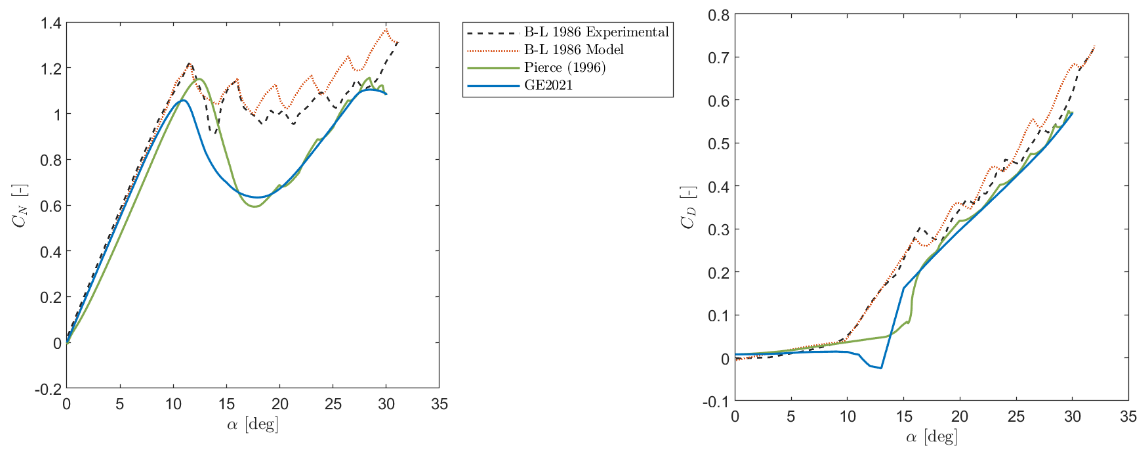

Figure 5.8: C_N for $M = 0.501$ and $\omega = 802 deg/s$ using data from the Beddoes-Leishman [18], the Pierce and the GE2021.

Due to the lack of vortex modelling, the inability of the GE2021 model to accurately capture the nature of the studied cases was foreseeable. In the case of the Pierce model, the modelling of the drag coefficient allows to understand the potential of this model. The peaks that clearly appear in the drag coefficient results coincide with the location of the peaks on the lift coefficient distribution. However, these oscillations become clearly visible when $\alpha > 20°$, which is inconsistent with the experimental data. Vortex effects are onset at lower angles of attack thus, this can be an indication that the first vortex affects an excessive portion of the cycle. Therefore, vortex speed tuning could be beneficial but a compromise with the performance of the vortex effects modelling at higher angles of attack would be necessary. In addition, the amplitude of these oscillations or peaks could be studied, as their magnitude is small compared to those observed in the experimental results.

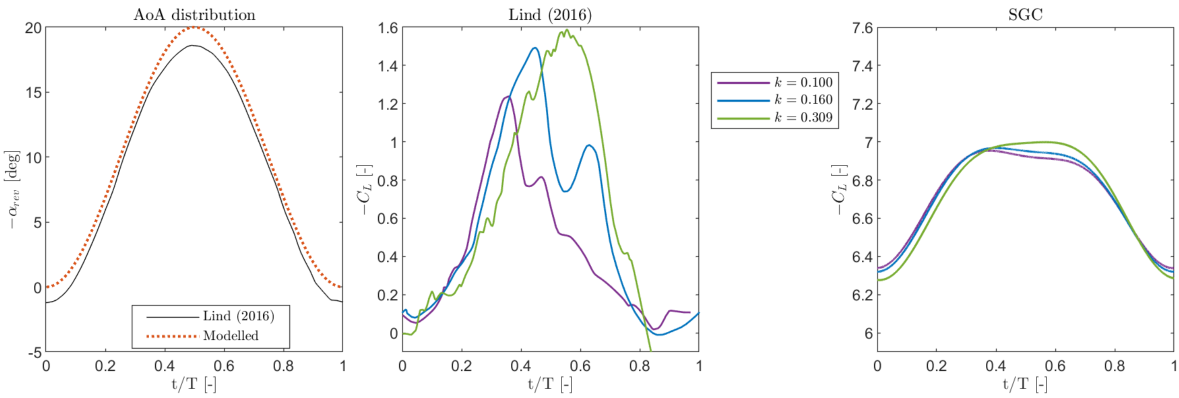

Figure 5.9: Angle of attack and $-C_L$ distributions obtained using the model proposed by Sheng, Galbraith and Coton compared to the experimental results from Lind (2016) [14].

The results for Cases E, C and F, obtained using the model formulated by Sheng, Galbraith and Coton are available in Figure 5.9. The figure in the center shows the results obtained by Lind, and the figure on the right are the the results obtained running these cases using the formulation by Sheng, Galbraith and Coton To ensure an appropriate assessment, the difference between the maximum and minimum values in the axis is of 1.7 for both experimental and modelled results. The results obtained using the formulation proposed by Sheng, Galbraith and Coton do not represent the peaks caused by vortex structures. However, it does slightly represent the delay caused by the increasing reduced frequency. The $-C_L$ distribution close to the start of the cycle ($t/T \approx 0$) vaguely resembles the effective angle of attack variation with reduced frequency showcased in Figure 2.10.

None of the studied cases activates the stall onset condition proposed by Sheng, Galbraith and Coton [26]. Therefore, revisiting the onset condition is necessary to allow for proper representation of the studied cases for which the vortex structures cause the greater part of the loading.

6 Vortex Effects Implementation

Chapter 5 provided a brief analysis of the capabilities of some of the well-established models discussed in Chapter 3. The focus of this project lies on reverse flow dynamic stall modelling, for which there is no available literature for possible modelling approaches. However, Section 2.2 made clear that vortex effects are the most relevant phenomenon in reverse flow dynamic stall. General Electric's current model, GE2021, neglects the loads generated by vortex effects. Therefore it is crucial to focus on the modelling techniques formulated to quantify vortex effects in the previously outlined models.

The semi-empirical model for dynamic stall presented by Beddoes and Leishman in 1986 uses a Kirchhoff approximation to compute vortex lift and a deficiency function to model the normal force generated by the vortex while tracking the vortex position and setting a reset condition to enable several vortices to be modelled. Pierce further expands upon this model by incorporating a chordwise vortex effect that had previously been disregarded [17] . More recent models that focus on HAWTs and low Mach number applications such as the one proposed by Sheng, Galbraith and Coton [26] or dos Santos and Marques [31], model vortex effects using sinusoidal functions.

Therefore, this chapter will focus on applying and analyzing the possible vortex effect implementations in combination to the separation effects obtained using GE2021. These formulations will be shortly outlined and their limitations will be discussed and compared to the data for reverse flow dynamic stall available in the literature. The studied cases are the same as the ones studied in Chapter 5 and available in Table 5.1. It is important to remind the reader that these cases were conducted with varying offsets due to a calibration issue. However, it was not feasible to incorporate this offset into the modelled cases.

6.1. Pierce Type Vortex Effects

The model proposed by Pierce offers modelling techniques for both separation and vortex effects, which are the main phenomena involved in reverse flow dynamic stall. The vortex effects implemented in the available Pierce model heavily rely on the Beddoes-Leishman vortex effects, which have been thoroughly validated and studied, as well as widely implemented in the industry to model dynamic stall for moderate angles of attack. Therefore, vortex effect and onset condition were defined for forward flow applications, as explained in Section 3.1.4.

Although this modelling method offers great reliability, combining the GE2021 separation effects formulation with the vortex effects computation from Pierce is not the most efficient approach, since it requires computing the circulatory loads using Equations 3.12 to calculate the vortex feed using Equations 3.13 and 3.14. This increases the computational time as additional loads that were used by Pierce also in the calculation of separation effects, are calculated solely for the computation of vortex effects in this new formulation, making this process somewhat redundant.

The only differences found in this available implementation when comparing the original Pierce model [17] to the Beddoes-Leishman [18] model, are the addition of chordwise vortex effects and the definition of the vortex tracking variable τ or τ_v. The original model does not offer a clear procedure of the calculation process for τ and defines T_{v_l} as the vortex passage time constant [18]. This definition implies that $\tau = 0$ at the time of the dynamic stall onset when the vortex is at the leading edge, and $\tau = T_{vl}$ when the vortex has reached the trailing edge. The work by Pierce, lacks again a clear procedure to calculate τ_v but defines T_{vl} as the "nondimensional time of transit for the vortex moving across the airfoil surface" [17], while mentioning $\tau_v = 0$ at the time of stall onset when the vortex is located at the leading edge, and $\tau_v = 1$ when the vortex reaches the trailing edge. Therefore, the implemented definition for τ_v is,

$$\tau_{v_n} = \tau_{v_{n-1}} + \frac{\Delta s}{T_{VL}}, \tag{6.1}$$

for which Δs is the increase in nondimensional time computed as $\Delta s = \frac{2\Delta t U}{c}$. This definition is likely to be the same as the one proposed by Beddoes and Leishman, normalizing it by dividing by T_{VL}, allowing a clearer study of the effect of the vortex convection speed over and past the airfoil.

Pierce extends the formulation of the Beddoes-Leishman vortex effect by introducing a chordwise vortex effect, which is discussed in Section 3.3. While this approach provides a more comprehensive model to account for dynamic stall effects, including those attributed to vortex effects, it comes with increased computational cost. Additional components of the normal force coefficient are required to compute the vortex effects, but the assessment of separation effects is calculated using the GE2021 model is neglected.

Nevertheless, the Pierce model has gained wide recognition as a highly established method for computing dynamic stall effects, particularly those associated with vortex effects.

6.1.1. Forward Flow Ramp-up

Two ramp-up cases were studied in the original Beddoes-Leishman model paper [18]. To compare the performance of the proposed models and the experiments, Figures 6.1 and 6.2 represent these two cases that were modelled using the model proposed by Pierce [17], GE2021 [23] and the new proposed combination, as well as the experimental and model results included in the Beddoes-Leishman paper [18].

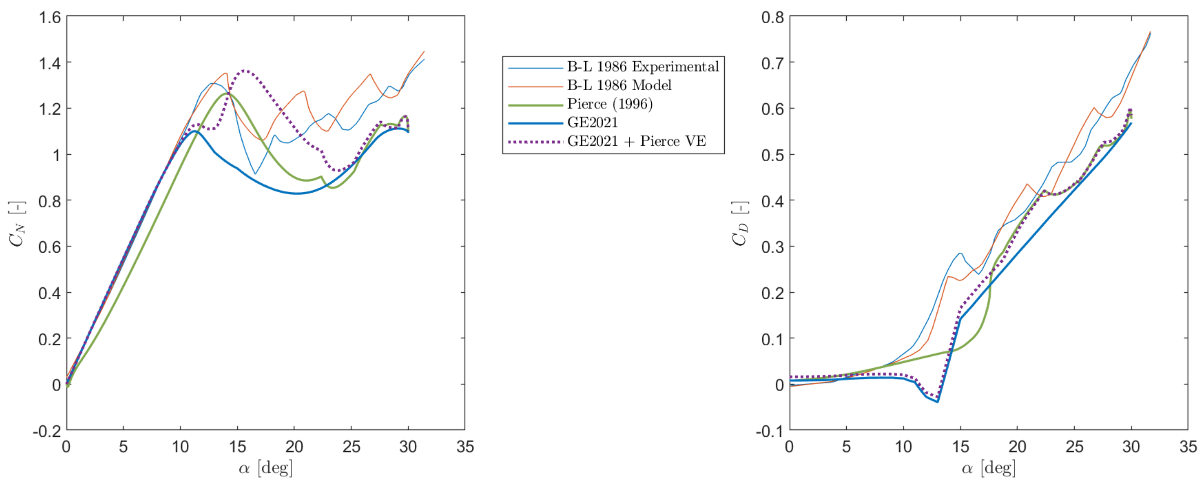

Figure 6.1: C_N for $M = 0.496$ and $\omega = 1493 deg/s$ using data from the Beddoes-Leishman [18], the code proposed by Pierce and the GE2021 with Pierce's formulation of vortex effects.

In both of the investigated cases, the model proposed by Pierce demonstrates a lower slope of the normal force coefficient (C_N) prior to stall. As the vortex effect onset condition for both Pierce and the "GE2021 + Pierce VE" model remains the same, the inception of vortex effects occurs at the same angle of attack. While this may be challenging to visualize, in Figure 6.1, a noticeable deviation between the "GE2021 + Pierce VE" model and the GE2021 model occurs at $\alpha \approx 8°$, indicating the onset of vortex effects. Thus, the disparity between these two models primarily stems from the calculation of vortex effects based on Pierce's implementation.

The implementation of the GE2021 shares similarities with Pierce's model and IStall2. This helps explain why, for higher angles of attack within the studied range ($20° \leq \alpha \leq 27°$), the C_N curves for "GE2021 + Pierce VE" and Pierce exhibit similar trends, and for $\alpha \geq 27°$, the results become nearly identical. A similar pattern is also evident in Figure 6.2. The early decay of C_N observed in the combination of GE2021 and Pierce is a consequence of the decay modelled by the GE2021 component. However, neither GE2021, Pierce, nor the combination accurately capture the stabilization of C_N at approximately $C_N \approx 1.1$, accompanied by vortex-induced oscillations evident in the experimental data, which is effectively captured by the Beddoes-Leishman model.

Furthermore, it is worth noting that for both the studied cases, the experimental results for the drag coefficient at angles of attack $\alpha \geq 15°$, follow a linearly increasing trend while oscillating. This oscillation is best captured by the Beddoes-Leishman model. However, the inclusion of the chordwise effect introduced by Pierce produces superior results compared to the original GE2021 model.

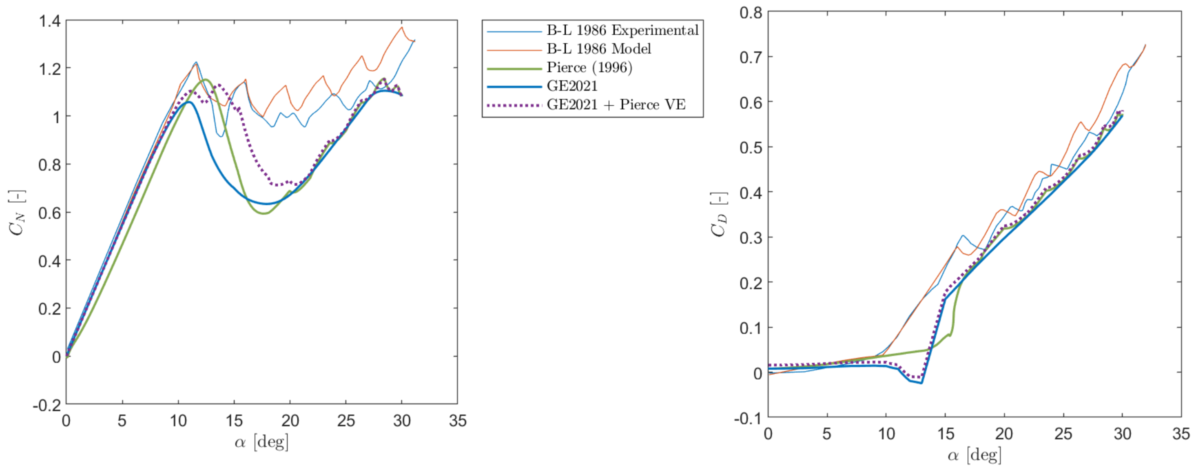

Figure 6.2: C_N for $M = 0.501$ and $\omega = 802deg/s$ using data from the Beddoes-Leishman [18], the code proposed by Pierce and the GE2021 with Pierce's formulation of vortex effects.

6.2. SGC Type Vortex Effects

Sheng, Galbraith and Coton present an alternative Beddoes-Leishman type model [26] that uses a formulation of vortex effects based on previous work carried out by Beddoes [30]. Access to the original work by Beddoes was not possible therefore, the implementation followed was that of Sheng, Galbraith and Coton. Throughout the implementation of the vortex effects following the SGC model, several questions arose.

Firstly, τ is defined as non-dimensional time ($s = \tau = 2Vt/c = Vt/b$), for which $\tau = T_v$ at the trailing edge, similar to the definition by Beddoes and Leishman. Additionally, as observed in Figure 6.3, this vortex tracking method combined with the formulation to compute the shape function V_x (Equation 3.42), allows a single vortex to generate more than one sinusoidal curve and therefore normal force peaks, before the vortex has shed. In addition, the use of the instantaneous separation point to compute the vortex effect on the normal force coefficient (Equation 3.43), allows for these secondary peaks to have a larger amplitude than the previous ones. The increase and decay in C_N due to effects generated by a single vortex before it has even vortex shed is already unphysical considering the studied literature but, also having the second generated peak being larger than the first also seems unrealistic and problematic.

Secondly, the definition of the shape function of normal force due to vortex effects (V_x) using Equation 3.42 causes sudden declines when the stall onset condition is not met anymore and τ is reset. These two issues are more easily recognisable in Figure 6.3b, where the focus is on the 'GE2021 + SGC VE'. SGC uses T_V as a reset condition however, no values for this constant is provided, and therefore, proper assessment of this method becomes challenging. Nevertheless, a sinusoidal representation of the vortex normal force seems to provide a good description of the vortex effects on the normal and lift coefficients. Therefore, a set of simple modifications were applied to test this approach further.

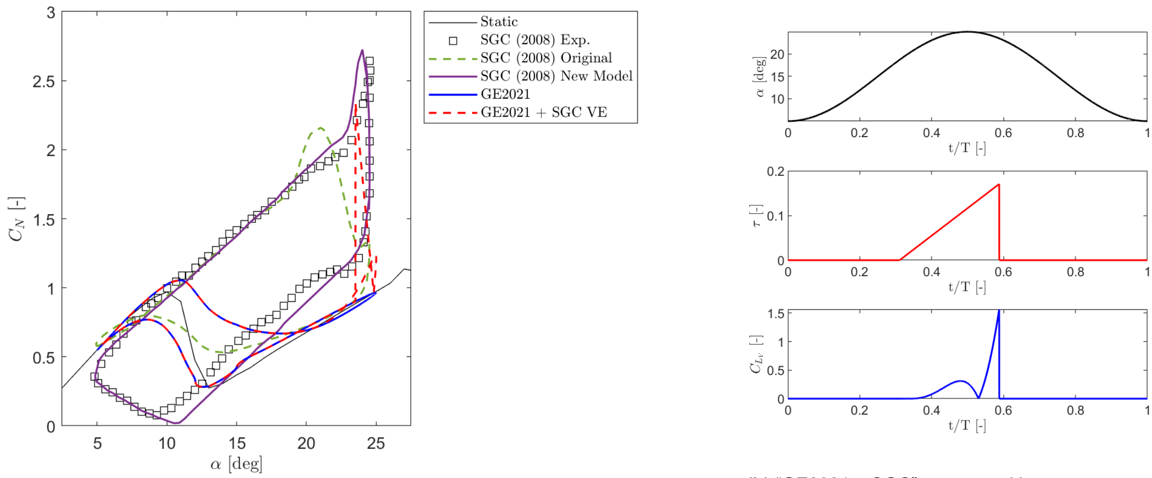

(a) C_N Comparison

(b) "GE2021 + SGC" vortex tracking constant τ and C_{L_v}

Figure 6.3: Comparison between SGC model [26] and the GE2021 with added vortex effects based on the SGC model. Case with M=0.12, k=0.124, $\alpha_m = 15°$ and $\alpha_a = 10°$.

6.2.1. Modified SGC Vortex Effects

In order to tackle the previously discussed issues, slight modifications in vortex tracking and calculation of C_{N_v}. The new definition of the vortex tracking variable τ_v was defined as shown in Equation 6.1. Therefore, the shape function of normal force due to vortex effects V_x was modified to reflect this, substituting T_v by 1.

$$V_x = \begin{cases} \sin^{3/2}\left(\frac{\pi\tau_v}{2}\right) & \text{if } 0 < \tau_v < 1 \\ \cos^2\left(\pi(\tau_v - 1)\right) & \text{if } 1 < \tau_v < T_{res} \end{cases} \tag{6.2}$$

It can be observed in experimental data obtained by Lind [14], that decay of the vortex effects occurs at a higher rate that the initial load increase. Therefore, the use of $sin^{3/2}$ to model the effect of the vortex when it moves over the airfoil, while using cos^2 to model the decay after the vortex is shed, allows to more accurately model this phenomenon. Figure 6.4b compares a sin curve to the shape that would produced by Equation 6.2. However, three more comments about the performed modifications need to be made.

Firstly, in order to keep the decay rate faster than the $|C_L|$ increase due to vortex effects the division by T_{VL} to compute V_x for the decay was eliminated from the original formulation. The division by T_{VL}

slowed the decay rate and the vortex convection velocity is accounted for when computing the vortex position τ_v, using Equation 6.1. The effect of the vortex speed will be further studied in Section 6.2.1.3.

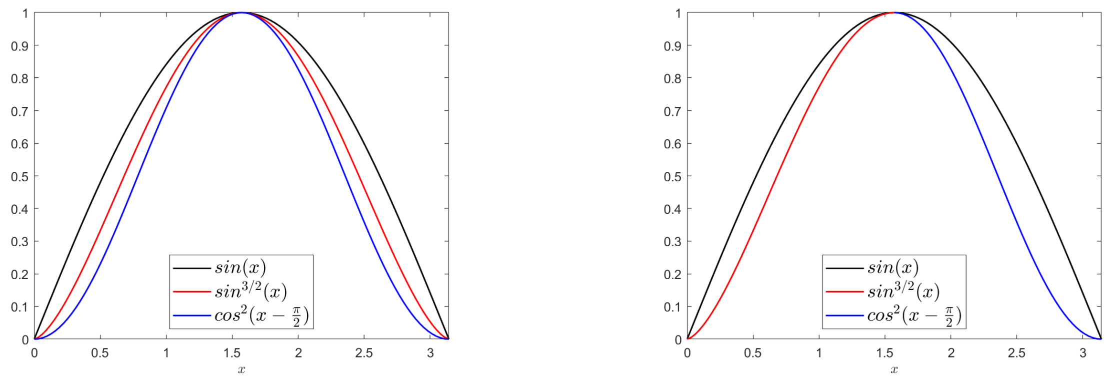

(a) Explored sinusoidal curves.

(b) Sinusoidal and actual distributions.

Figure 6.4: Sinusoidal curves comparison.

Secondly, as previously discussed and explained by the literature, a single vortex increases $|C_L|$ while convecting over the airfoil, and forces a decay in $|C_L|$ when the vortex is shed from the airfoil. Therefore, a single vortex only generates a single $|C_L|$ peak, which is inconsistent with the original SGC formulation previously discussed. Thus, to properly model this, the cos^2 decay is only allowed if $1 < \tau_v < T_{res}$ until V_x reaches a zero value, further oscillations are not allowed to avoid possible jumps and oscillations of the same or larger amplitude as the initial curve generated by the same vortex. Nevertheless, after the reset condition T_{res} has been reached, if the airfoil continues to pitch up and the stall onset condition still applies, a new vortex is modelled.

Lastly, separation effects are computed using GE2021, therefore, the used values of f'' and f used in Equation 3.43 to compute C_{N_v} are those of f_{dyn} and f_{stat} from GE2021 respectively. However, while the the SGC model uses the instantaneous value of $f_{dyn} - f_{stat}$, the maximum difference in the portion of the cycle affected by the vortex was used to ensure the maximum possible impact of the modelled vortex is represented.

Figure 2.9, provided some valuable insights about the effects of the reduced frequency in the vortex generation. Lower reduced frequencies imply longer pitching cycles, allowing for a larger number of vortices to be generated in said pitching cycle than in those where the reduced frequency is higher. In addition, increasing reduced frequency delays the generation of vortices, and a delayed effective angle of attack distribution was presented in Figure 2.10. Therefore, the addition of a reduced frequency delay in the effective angle of attack is necessary to accurately capture this phenomenon.

The angle of attack distribution in a pitching cycle was previously determined using a sinusoidal motion described by

$$\alpha(t) = \alpha_m + \alpha_a \sin\left(\frac{2\pi t}{T}\right) \tag{6.3}$$

To account for the delay in the effective angle of attack caused by the increasing reduced frequency, a term is added based on the ratio of the reduced frequency to a baseline reduced frequency that was set to $k_0 = 0.2$. This term also makes use of a proportionality constant d, allowing to tune the impact of this delay. The resulting modified angle of attack distribution equation is

$$\alpha(t) = \alpha_m + \alpha_a \sin\left(\frac{2\pi t}{T} + d\frac{k}{k_o}\right) \tag{6.4}$$

In order to effectively model the effects of dynamic stall in reverse flow, various parameters and conditions must be carefully considered:

- **Vortex effects onset conditions:** The onset conditions for vortex effects are of crucial importance when modelling dynamic stall phenomena. By examining the available literature, particularly studies on reverse flow, where sharp aerodynamic leading edges are encountered, using airfoils such as the NACA 0012 and NACA 0024 [13] (as discussed in 2.2.1), it becomes evident that these airfoils demonstrate consistent behavior characterized by the separation of airflow at low angles of attack. This observed separation phenomenon serves as a valuable starting point for determining the vortex onset condition. It is reasonable to assume that a critical angle of attack at which separation occurs can be regarded as the threshold for the onset of vortex effects. Therefore, the vortex effects on loading will be onset if the airfoil is pitching up, and the defined critical angle of attack is surpassed.

- **Reduced frequency delay effect:** It has been observed in the literature, particularly in Figure 2.9, that the onset of vortex effects is delayed with increasing reduced frequency. One possible approach to address this delay is to modify the stall onset angle using a delay proportional to the reduced pitch or reduced frequency. However, this approach would limit the occurrence of vortex effects to a smaller portion of the aerodynamic cycle, which contradicts the observations seen in the data depicted in Figure 2.9. Alternatively, the incorporation of a delay in the effective angle of attack was selected to tackle this (Equation 6.4). This adjustment closely corresponds to the observed behavior illustrated in Figure 2.10. Nevertheless, this approach overlooks the increase in amplitude of the effective angle of attack with reduced frequency also evident in Figure 2.10.

- **Vortex Strength:** The pressure coefficient distributions shown in Figure 2.9 might suggest that higher reduced frequencies result in stronger vortices. However, it is noteworthy that the maximum lift coefficient observed in the different studied cases does not vary significantly, except for the case with $k = 0.100$. Consequently, a constant vortex strength coefficient will be employed to calculate the corresponding effects in order to simplify the modelling process.

- **Vortex Reset condition:** In the Beddoes-Leishman model (Section 3.1.4), two different formulations are proposed for the vortex reset condition, which allow for the modelling of secondary or subsequent vortices. The first approach uses a constant as the reset condition. Meanwhile, the second approach calculates the reset constant based on the Strouhal number, as presented in Equation 3.11. Since the available information about vortex shedding frequency is limited, and considering the observations in Figure 2.12 where the generation of the secondary dynamic stall vortex in cases C and D appears to occur shortly after the shedding of the first vortex, utilizing a constant reset condition seems to be a suitable initial approach.

- **Vortex speed (T_{VL}):** In reverse flow dynamic stall (Section 2.2), it has been established that the vortex speed is generally slower compared to its forward flow counterparts. This difference in speed implies that a tuning of the vortex speed may be required to accurately model these effects.

Each of these parameters is related to a physical reality of vortex behavior and its effects on the airfoil loading. Therefore, these parameters and their effects on the flow modelling will be now studied.

6.2.1.1. Delay (d)

The delay in the effective angle of attack with increasing reduced frequency observed and discussed in Section 2.10 and Figure 2.9 has a significant impact on the load generation. It affects the portion of the cycle for which load peaks will occur and is therefore important to model its effect.

As the GE2021 model, used to compute the separation effects in this proposed model, has been widely validated, it is worth analyzing whether the delay needs to be applied solely to the vortex effects computed using the discussed modified SGC, or to the whole flow model. This was further analysed for the simpler sinusoidal approach in Section 6.3.1, from which it was concluded the delay in the effective angle of attack should affect both separation and vortex effects. This aligns with Lind's observation regarding the impact of reduced frequency on the effective angle of attack, emphasizing that it encompasses more than just vortex effects. The impact and selection of the most suitable value for the delay proportionality constant d that appears in Equation 6.4 will therefore be the focus of this section.

Cases A, B, C and D have a common reduced frequency $k = 0.16$ while Case E has a $k = 0.100$ and Case F a $k = 0.309$. Cases C, E and F share the same pitching distribution, with a mean angle of attack $-\alpha_{m,rev} \approx 10°$ and a pitching amplitude $\alpha_a \approx 10°$. As mentioned in discussed in Chapter 5, an error in calibration impacted the cases studied by Lind [10] and there is therefore a mismatch in between the experimental data and the modelled results. Although the impact of these differences is expected to be small, it was deemed important to mention them regardless.

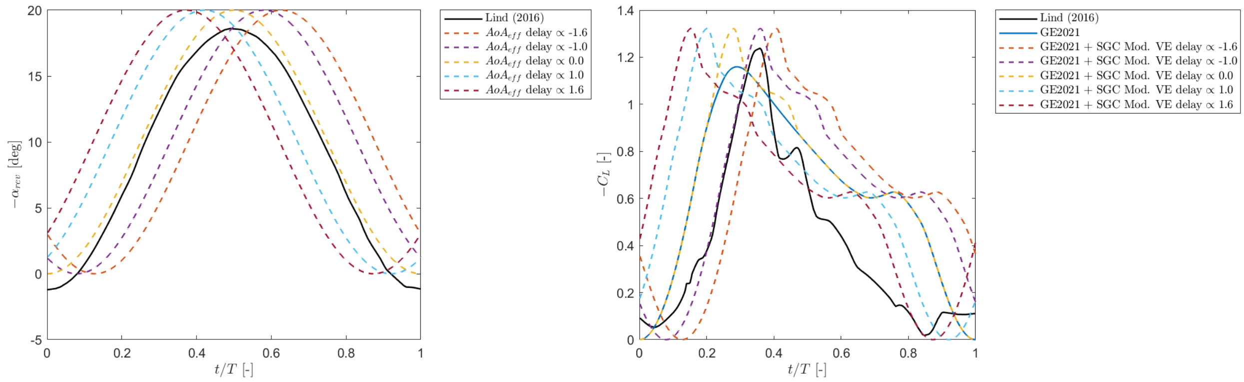

(a) Case E ($k = 0.100$).

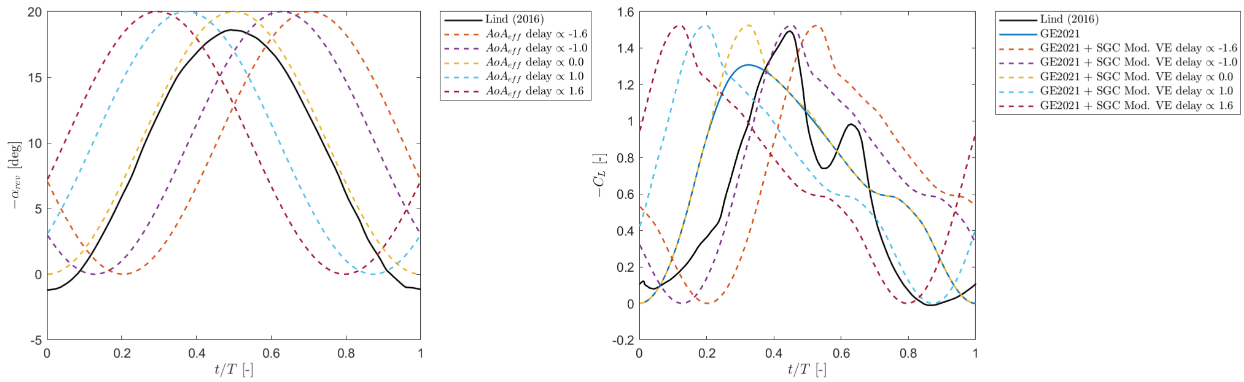

(b) Case C ($k = 0.160$).

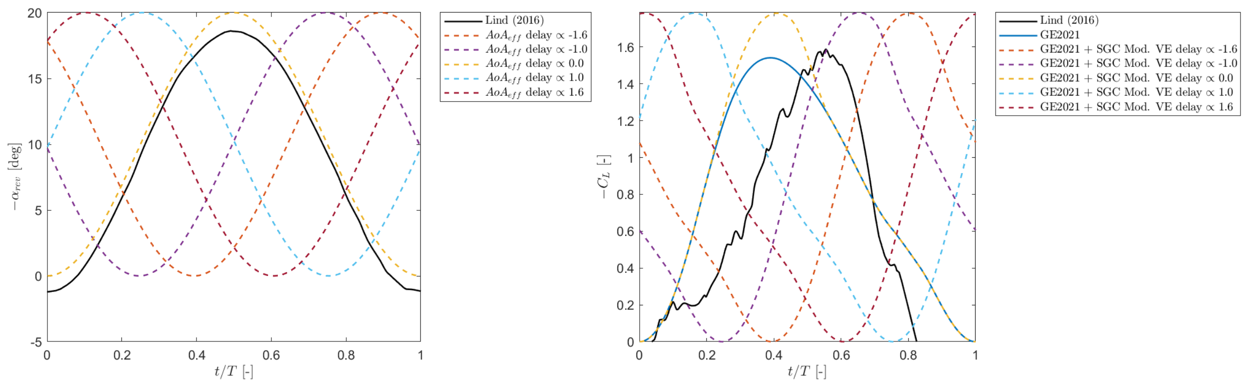

(c) Case F ($k = 0.309$).

Figure 6.5: Cases E, C and F. Experimentally with $\alpha_{m,rev} = 8.9°$ and $\alpha_a = 9.9°$ [14]. Modelled cases with $\alpha_{m,rev} = 10°$ and $\alpha_a = 10°$.

Several values for the proportionality constant d, from equation 6.4, were tested to assess the value that produced the best match between experimental data and modelling results. From the literature, a delay is expected, and therefore, the defined d is expected to be negative. A positive value of d would mean an anticipation of the angle of attack distribution, that would be contrary to the flow physics. However, both positive and negative values of d were tested to enable visualization of the implications associated with various d values and their signs.

Figure 6.5 shows the effect of varying d for different reduced frequencies. As k_0 is set to $k_0 = 0.2$, a lesser impact is observed for Case E, an impact that increases with increasing reduced frequency. Although the delay is overcompensated for Case F for which the reduced frequency is the highest, a significant improvement when comparing to the original GE2021 is still obtained. The steep increase in $-C_L$ and the timing of loading increments due to the vortex effects align closely with the ones observed in the experimental data for Cases E and C.

GE2021 is used to model separation effects and therefore acts as a baseline, this limits the extent that vortex effects are able to impact the modelled results. An illustration of this issue is clear in the results showcased in Figure 6.5, where although the initial increase in $-C_L$ is better matched with the use of the delayed angle of attack, the modelled decay is slower than the one observed in the experimental data. This also occurs for Cases B and D, which results are found in Figures A.1 and A.2 in Appendix A.1.1. It is important to note that the issues rooted on the computation of separation effects with GE2021, will remain unaffected regardless of the tuning of the vortex effect parameters. Therefore, comments regarding the coming analysis will focus on assessing the performance of the proposed modelling of vortex effects.

6.2.1.2. Dynamic stall onset (α_{vortON})

In the context of reverse flow dynamic stall, flow separation typically occurs at low angles of attack due to the presence of a sharp aerodynamic leading edge. The available literature on reverse flows shows that flow separation for a NACA 0012 occurs at low angles of attack of around $\alpha_{rev} \approx 7°$ [13]. Therefore, a critical angle of attack (α_{vortON}) was defined at which vortex effects are onset. Various onset angles of attack were tested to capture the one that yielded the closest results to those obtained experimentally.

The results for the studied cases show strong performance using $\alpha_{vortON} = 7°$ and $\alpha_{vortON} = 8°$. Cases C and D are showcased in Figures 6.6 and 6.7 respectively. The use of a lower α_{vortON} implies an earlier onset of vortex condition, meeting the vortex reset condition earlier in the cycle and enabling a possible secondary dynamic stall vortex to be generated.

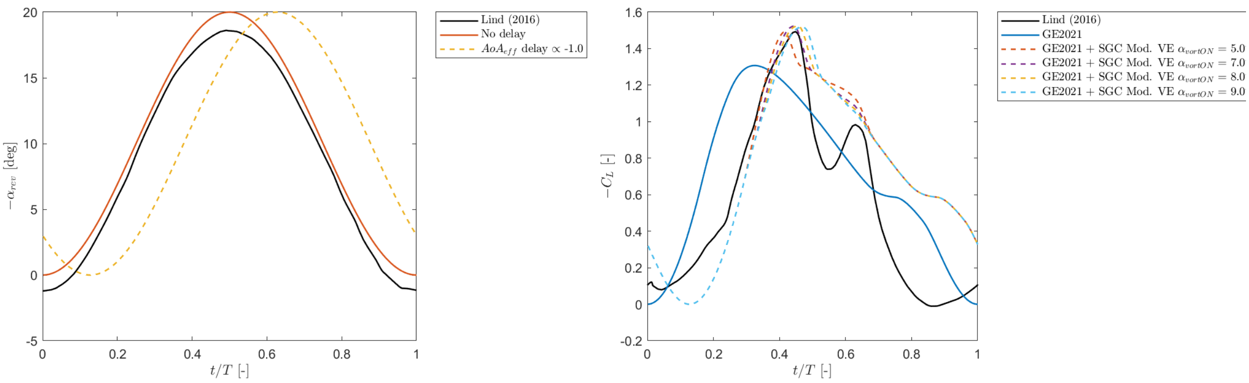

Figure 6.6: Case C results for $-C_L$ for with $d = -1$ and different vortex effects onset angle of attack α_{vortON}.

Case C showed good timing for the first and second vortex effects. When using $\alpha_{vortON} = 7°$, both vortices occur slightly earlier in the cycle than in the experimental data. When applying an $\alpha_{vortON} = 8°$ the effect of the secondary dynamic stall vortex is insufficient. However, although its impact is limited, the reality is that the separation effects after the decay of the first vortex exceed the experimentally obtained $-C_L$.

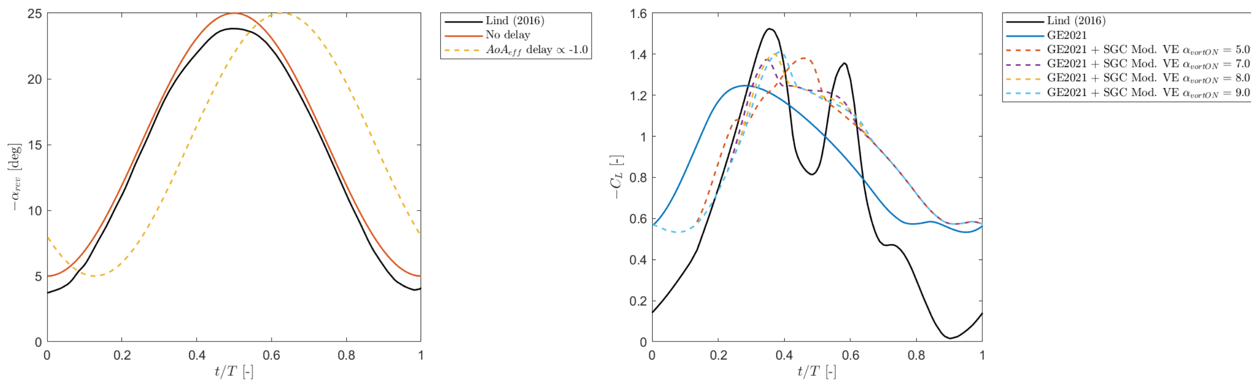

Figure 6.7: Case D results for $-C_L$ for with $d = -1$ and different vortex effects onset angle of attack α_{vortON}.

Case D yields similar results as the previously discussed for Case C. In addition to prior comments on vortex effects timing and amplitude, the modelled results for cases D and B (Figure A.3) double and triple the experimental data when the angle of attack has its lowest magnitude. The cause for this discrepancy was further explored in Chapter 5, and rooted on the use of the static polar to obtain the inviscid lift, impacting the lift derived from the flow separation effects.

6.2.1.3. Vortex Velocity (T_{VL})

The vortex location is tracked using τ_v, which is computed using Equation 6.1. This equation utilizes the parameter T_{VL} to modify how fast τ_v increases, thus, it can be set to control vortex convection rate. Vortex velocity over the airfoil in reverse flow dynamic stall is critical to determine the number of vortices developed throughout a pitch cycle.

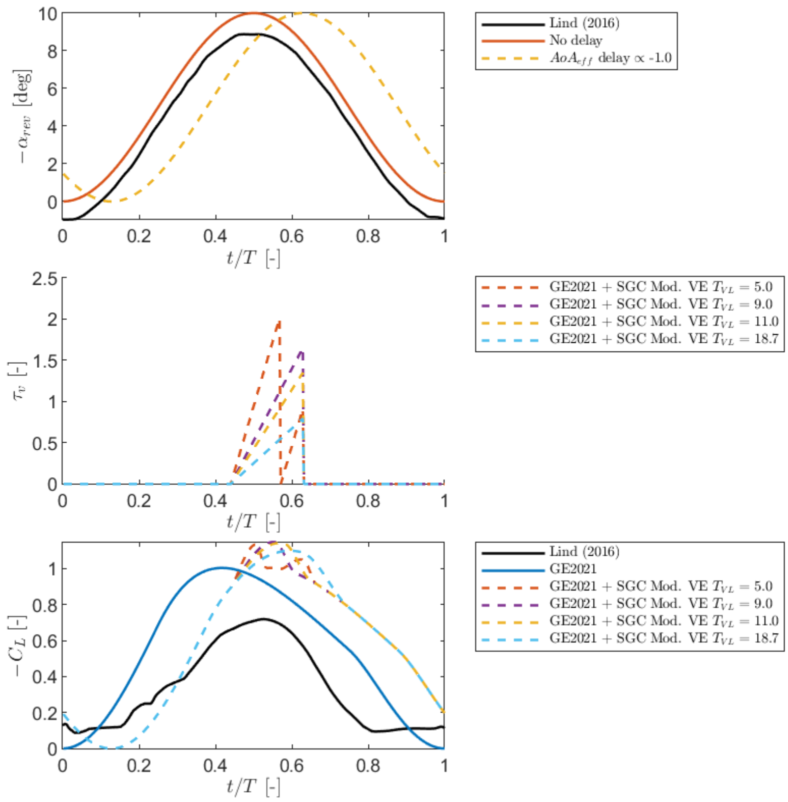

Figure 6.8: Case A results for τ_v and $-C_L$ with $d = -1$ and different vortex velocities T_{VL}.

In addition, the magnitude of the loads generated by these vortices are also affected by the value of T_{VL}, as covering a wider range of the cycle also implies having more separation point values f_{stat} and f_{dyn}, which directly impact the calculation of C_{N_v}, possibly varying the maximum difference used in Equation 3.43.

Case A, represented in Figure 6.8, exemplifies the effect of having slower ($T_{VL} = 18.7$) or faster ($T_{VL} = 5.7$) convecting vortices. The use of $T_{VL} = 5$ allows for multiple vortices to be generated, which is contrary to the results in the available literature for Case A. Therefore, slower convection and thus higher values of T_{VL} are necessary to obtain a more similar resemblance between modelled results and experimental data.

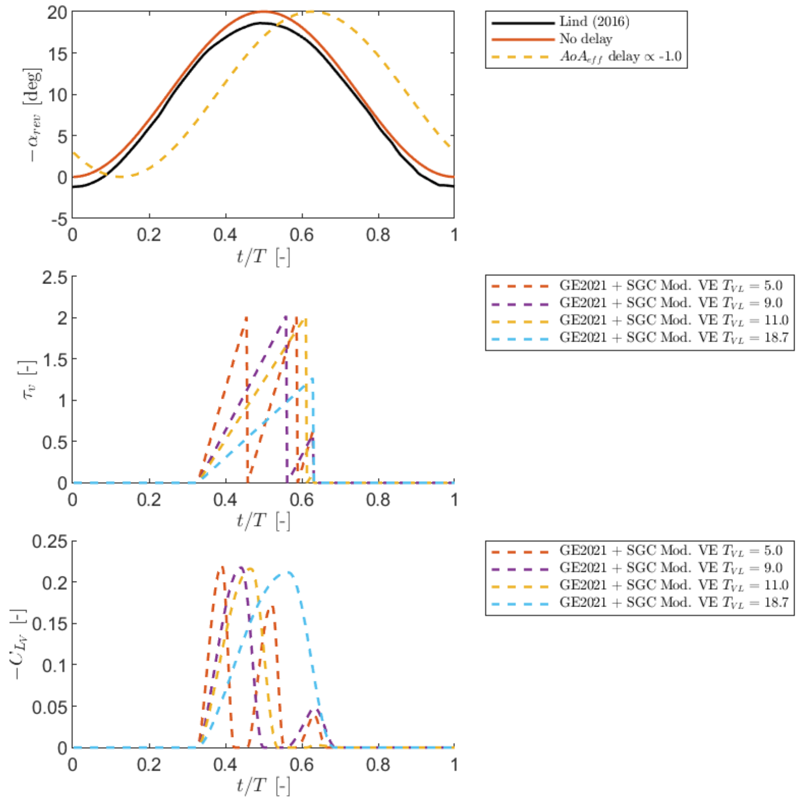

Figure 6.9: Case C results for τ_v and $-C_{L_V}$ with $d = -1$ and different vortex velocities T_{VL}.

Figure 6.10 portrays the results for Case C, for which the literature results show a primary and secondary dynamic stall vortex. This case is more appropriate to showcase that the vortex convection speed not only determines the number of vortices allowed in the cycle, but a proper T_{VL} tuning allows to properly represent the portion of the cycle influenced by each individual vortex. As made visible in Figure 6.9, the use of $T_{VL} = 5$ allows for a third dynamic stall vortex to be form which occurs close to the onset of the second dynamic tall vortex when using $T_{VL} = 9$. Although their onset is closely timed, the magnitude of the C_{L_V} generated by the SDSV when using $T_{VL} = 9$ has a higher magnitude than the one obtained when using $T_{VL} = 5$.

Figure 6.10, is also a great portrayal of the importance of a good definition for T_{VL} as this allows to control not only the increase rate of $-C_{L_V}$, but also the decay speed that is also a function of τ_v. The use of $T_{VL} = 11$ in accordance of the previously available Pierce model, has a lower $-C_L$ growth and decay rates than that of the experimental data. Additionally, the slower convection limits the formation of the SDSV. Therefore, an intermediate $T_{VL} = 9$ seems to produce results with greater similarity to the empirical observations.

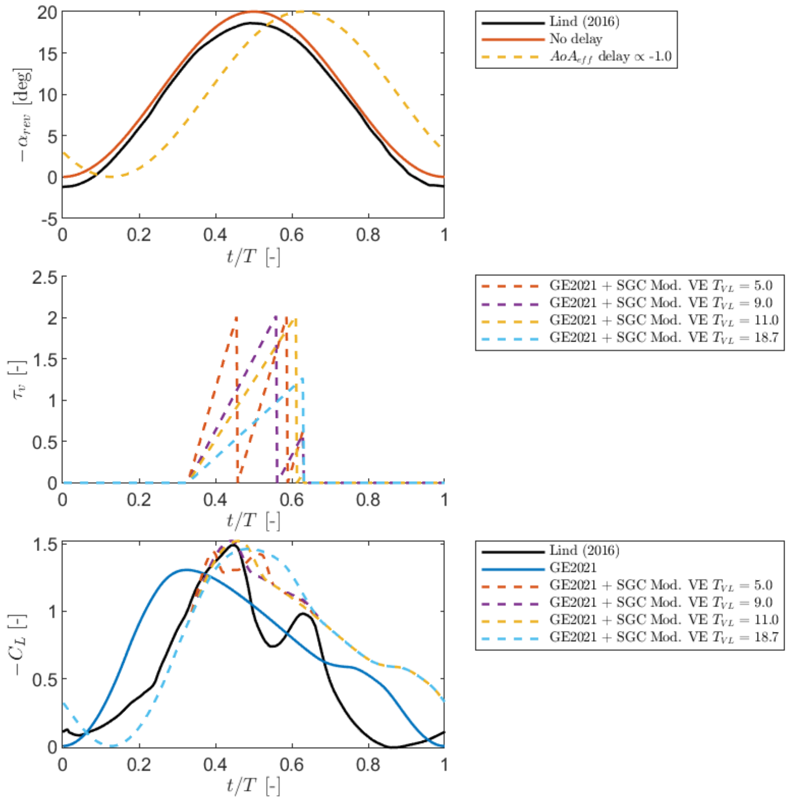

Figure 6.10: Case C results for τ_v and $-C_L$ with $d = -1$ and different vortex velocities T_{VL}.

6.2.1.4. Vortex Reset condition (T_{res})

Throughout a pitching cycle, several dynamic stall vortices can be generated. In some of the studied cases such as A and F, a single vortex is convected while for others a secondary dynamic stall vortex can be observed. In order to properly model the possible multiple dynamic stall vortices, a reset condition for which τ_v becomes zero, and a secondary vortex begins to be tracked is necessary.

As previously discussed, although in the Beddoes-Leishman model proposes a reset condition based on the Strouhal number [18], the lack of data on the shedding frequency in reverse flow dynamic stall does not allow to follow this procedure. Therefore, a constant T_{res} was used as a vortex tracking reset condition.

If the primary dynamic stall vortex has been shed, $\tau_v = T_{res}$ and the magnitude of the angle of attack continues to grow, τ_v is set to zero and a new vortex is now tracked, until either the reset condition is met again, or the magnitude of the angle of attack begins to decay.

The value of T_{res} does however not affect the onset or development of the first vortex. This is clear for Case F shown in Figure 6.11, where for both results for τ_v and $-C_L$ overlap with each other regardless of the reset condition. Regardless of the value for T_{res}, the vortex velocity remains unchanged, and therefore, there is an overlap in τ_v and therefore the resulting $-C_L$. In addition, the lowest studied value for the reset condition T_{rest} is not met, and therefore the results are the same.

Figure 6.12 shows again that the first peak generated by the first vortex overlaps regardless of the T_{res}. This verifies that the sinusoidal curve grows until $\tau_v = 1$ or the stall onset condition does not apply anymore, and decays at the same rate independently from the value of T_{res}. Once the defined value for the reset condition is achieved ($\tau_v = T_{res}$), the following vortex is allowed to develop.

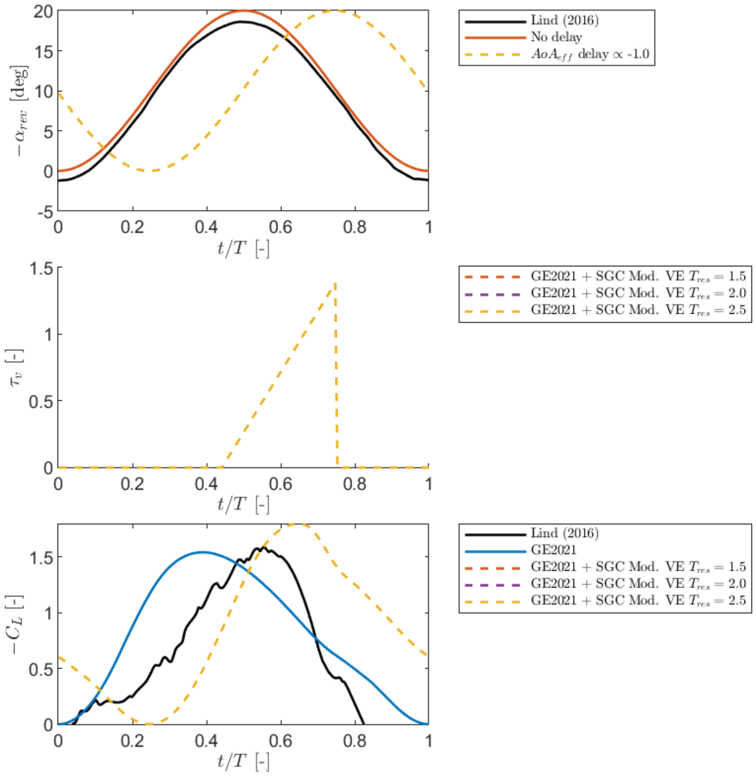

Figure 6.11: Case F results for τ_v and $-C_L$ with $d = -1$ for different reset vortex condition T_{res}.

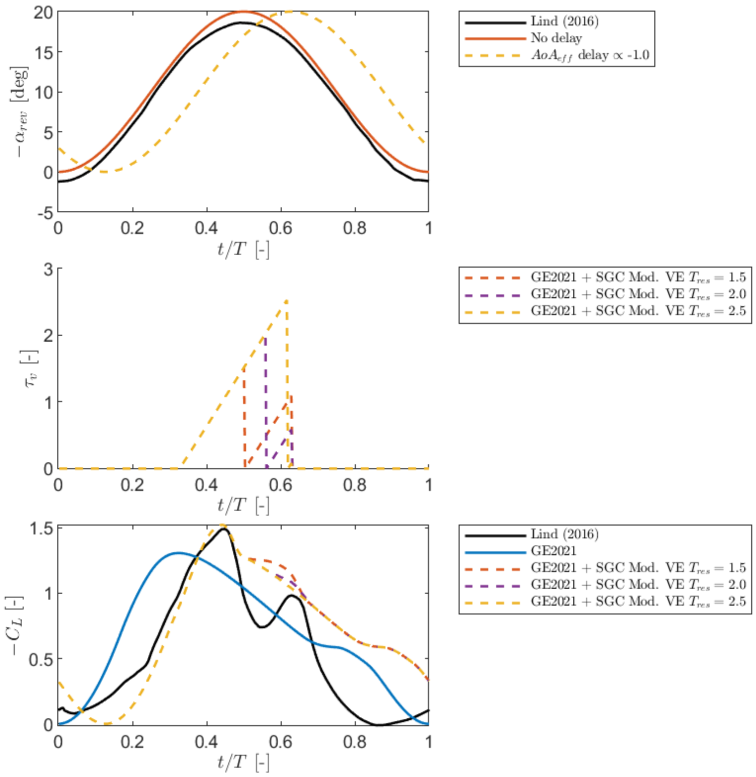

Figure 6.12: Case C results for τ_v and $-C_L$ with $d = -1$ for different reset vortex condition T_{res}.

From the obtained results, the fitter value for the vortex tracking constant was found to be $T_{res} = 2$, which allows for secondary vortices to be generated close to the time in the cycle for which the experimental data shows the impact of a SDSV, although having a smaller magnitude. Nevertheless, Section 6.2.1.5 tackles the use of the constant B_1 found in Equation 3.43 to adjust the magnitude of C_{N_v}.

6.2.1.5. Vortex Strength (B_1)

The formulation proposed by Sheng, Galbraith and Coton for C_{N_v} (Equation 3.43) used the coefficient B_1 to adjust the impact of the vortex generated loading. However, as every constant tuning procedure, trade-offs are necessary to obtain the optimal results to effectively model the diverse range of cases available. Vortex strength is defined by several parameters, including the separation point and the sinusoidal distribution V_x (Equation 6.2). However, a final tuning using B_1 as a proportionality coefficient is still necessary.

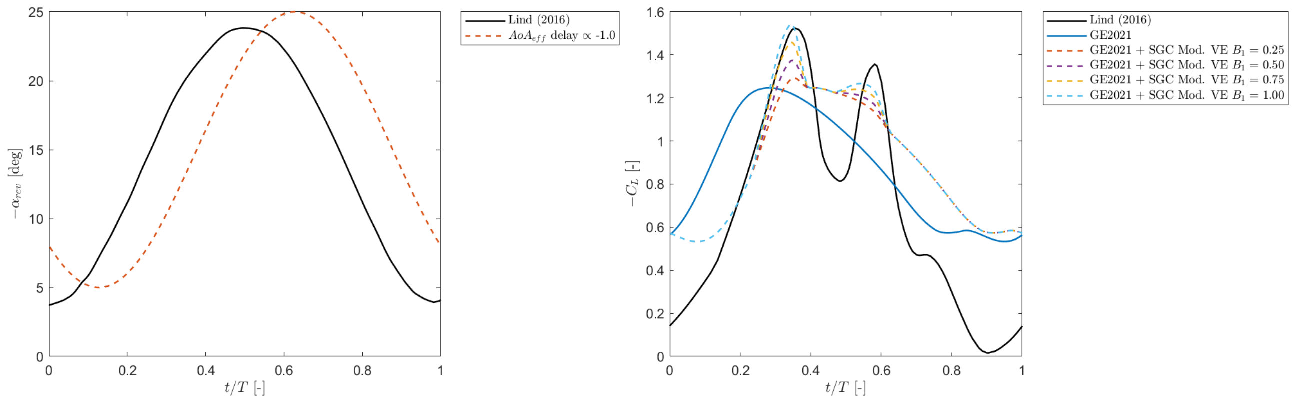

Figure 6.13: Case D results for $-C_L$ with $d = -1$ and different vortex intensity proportionality coefficients B_1.

Cases D and E showcase the extremes in the tuning of B_1. Having Case D (Figure 6.13) the largest pitching amplitude of all the studied cases, the proposed model returns higher overall values of separation lift C_{L_f}, that consist on the delayed results of GE2021. The GE2021 results for Case E (Figure 6.14), and therefore separation loads (C_{L_f}), are closer to the experimental lift distribution although decay is slower.

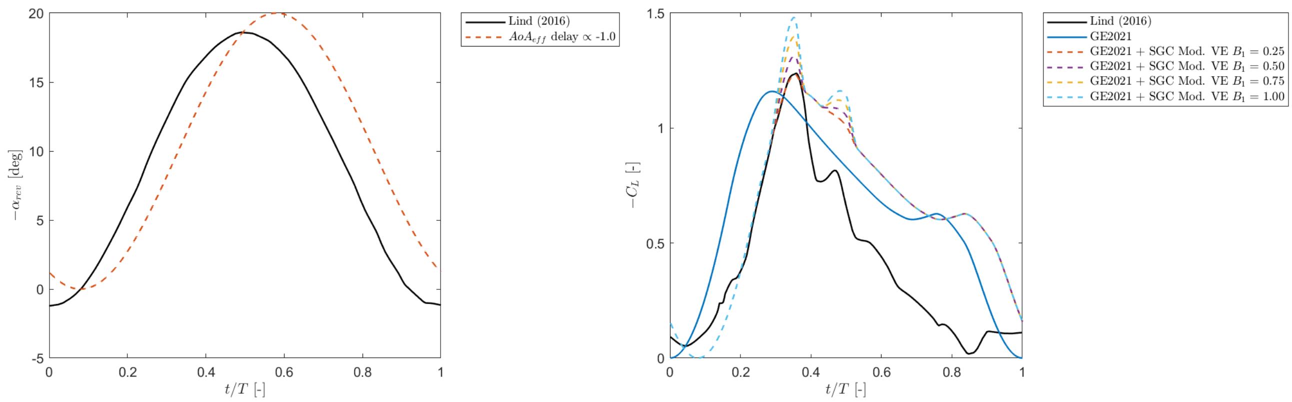

Figure 6.14: Case E results for $-C_L$ with $d = -1$ and different vortex intensity proportionality coefficients B_1.

On the other hand, the amplitude of the vortex generated lift C_{L_V} has a similar amplitude on all the six explored cases (Figures A.4, A.5 and A.6). Figure 6.15, showcases the $-C_{L_V}$ and the separation points from used in Equation 3.43 to compute C_{N_v}. This combined with the C_{L_f} distributions generates a discrepancy between empirical data and modelling results, as well as the need to find a value for B_1 that allows a trade-off between all the studied cases. Case E benefits for a lower value of $B_1 \approx 0.25$, as the modelling due to separation exceed those measured, while Case D would need a $B_1 \approx 1.0$ to yield results closer to those of the experimental data set. Therefore, a $B_1 \approx 0.5$ was finally selected as a middle ground.

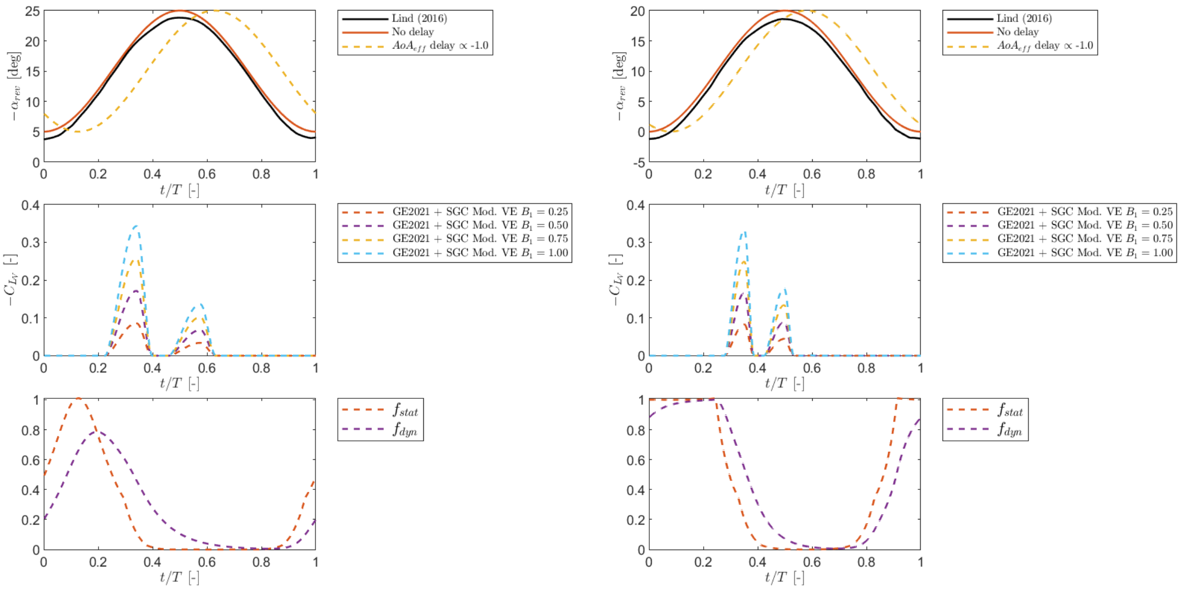

(a) Case D. **(b)** Case E.

Figure 6.15: Results for $-C_{L_V}$, τ_v and separation points with $d = -1$, using different vortex intensity proportionality coefficients B_1.

6.2.2. Forward Flow Ramp-up

This model needs to effectively capture both forward and reverse flow conditions. To validate its performance in forward flow, two ramp-up cases used in the validation of the Beddoes-Leishman model [18] were investigated. Although most of the best performing values of previously assessed parameters were maintained, a forward flow critical angle of attack for vortex effect onset needed to be set. In addition, the effective angle of attack delay was disregarded, therefore $d = 0$.

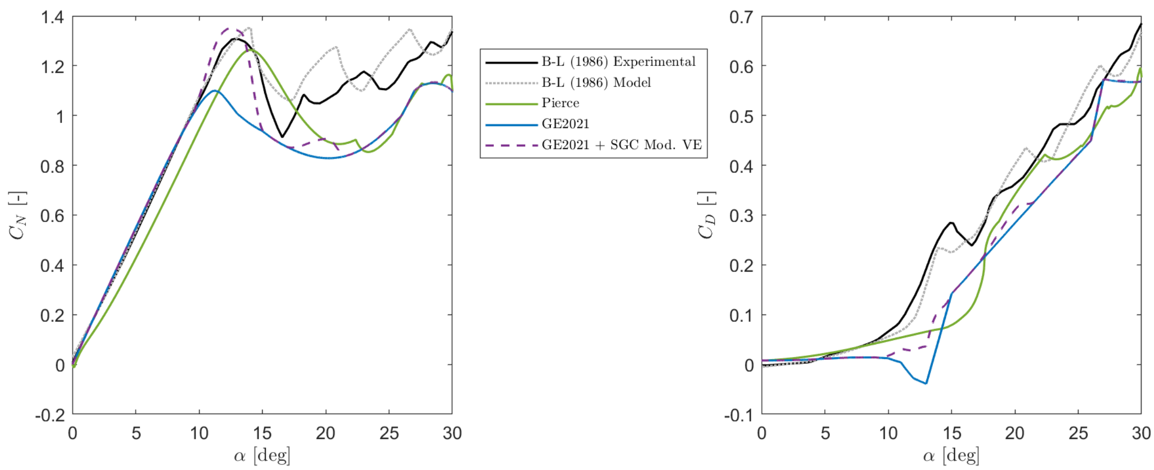

Figure 6.16: C_N and C_D for ramp-up case with $M = 0.496$ and $\omega = 1493 deg/s$ [18].

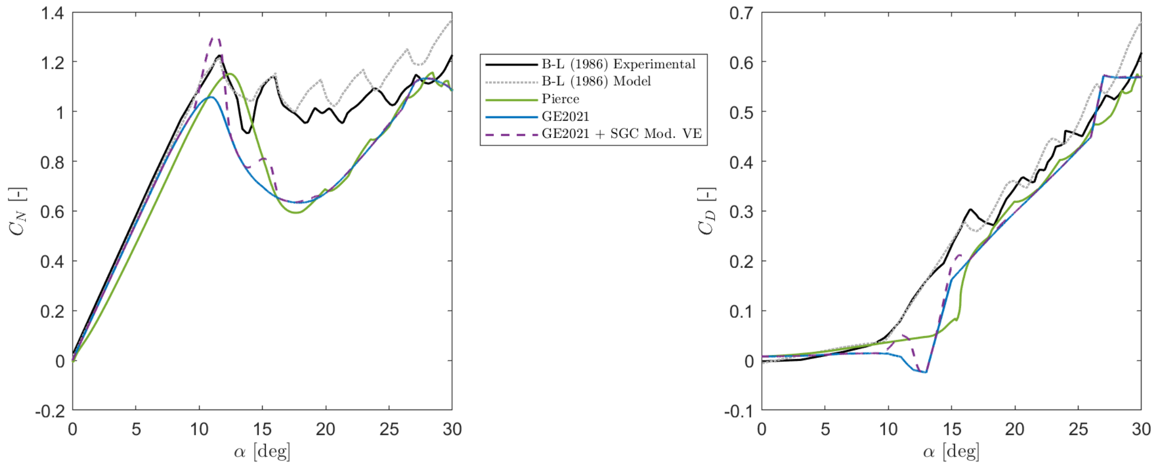

Figure 6.17: C_N and C_D for ramp-up case with $M = 0.501$ and $\omega = 802 deg/s$ [18].

The results offered by "GE2021 + SGC Mod. VE", showcased in Figures 6.16 and 6.17, showed the benefits of the addition of vortex effects when compared to those of GE2021 at low angles of attack. However, for angles of attack higher than $\alpha \approx 15°$ and $\alpha \approx 20°$ the generated vortex normal force C_{N_v} comes close to zero. This occurs because the difference between f_{stat} and f_{dyn} becomes close to zero as it is made evident in Figure 6.18. It is interesting to note that although no vortex effects are added in the chordwise direction, there is still a clear impact of the C_{N_v} on the drag coefficient. Further validation would be necessary to properly assess if the addition of C_{C_v} is necessary.

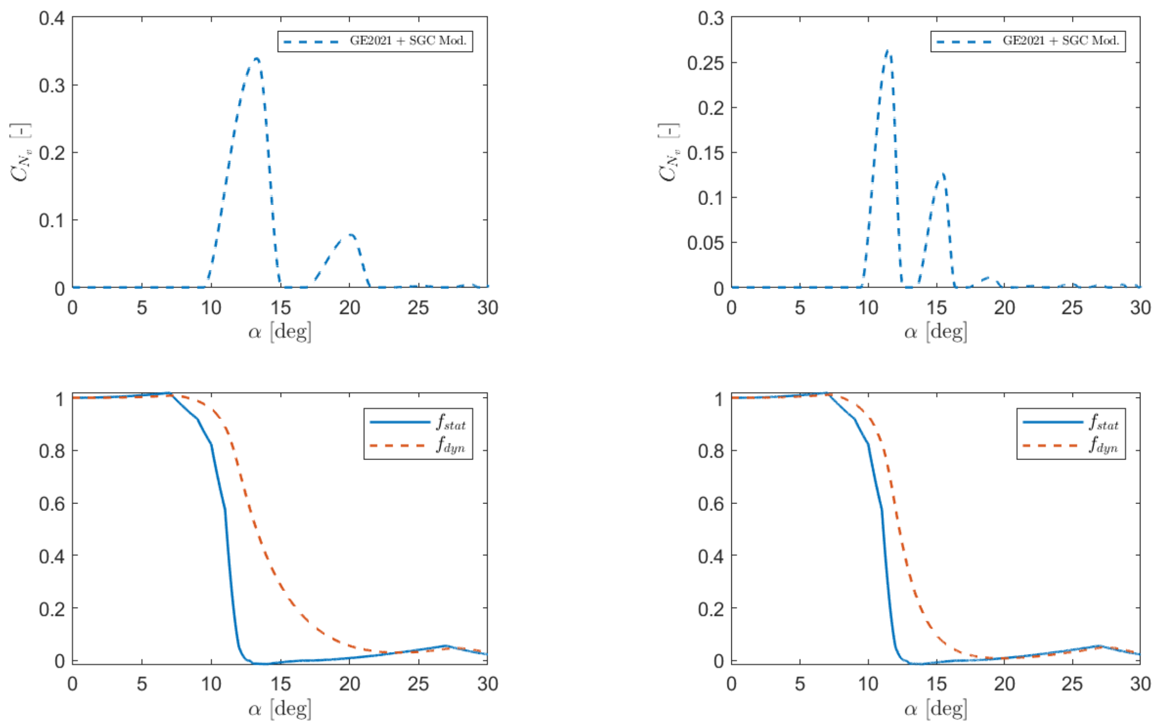

(a) C_{N_v} and separation points for $M = 0.496$ and $\omega = 1493 deg/s$.

(b) C_{N_v} and separation points for $M = 0.501$ and $\omega = 802 deg/s$.

Figure 6.18: Ramp-up cases using different vortex effects onset angle of attack.

6.3. Sinusoidal Type Vortex Effects

In order to effectively model the effects of dynamic stall in reverse flow, various parameters and conditions must be carefully considered. While the SGC [26] and Beddoes [30] vortex effects implementations offer detailed approaches, a simpler alternative in the form of a sinusoidal vortex effect was explored. This alternative also makes use of the parameters and conditions of the Modified SGC model discussed in Section 6.2.1, including the definition of the delayed effective angle of attack presented in Equation 6.4.

The computation of the vortex normal force will follow a similar procedure to the one presented in Equations 3.42 and 3.43, as well as the formulation of the modified inviscid lift curve of the GE2021 model (Section 3.4). The vortex strength will be represented by a piecewise function consisting of sinusoidal segments.

To determine the start and end of each sinusoidal segment, the position of the vortex, τ_v, is tracked using Equation 6.1. It is important to note that this simplification comes with limitations. In reality, the vortex strength tends to increase as it convects over the airfoil ($\tau_v < T_{VL}$) and decreases when it sheds into the wake. However, in this formulation, the sinusoidal function grows and decays between the vortex onset condition and the vortex reset condition, or between reset conditions. As a result, some of the physical realism is compromised, as the maximum amplitude of the sinusoidal curve is unlikely to be attained precisely when the vortex reaches the trailing edge ($\tau_v = 1$). This scenario would only arise if the reset condition were defined as $T_{res} = 2$.

The amplitude of the sinusoidal curve is calculated based on the maximum difference between the dynamic and static separation points throughout the affected sinusoidal segment, along with a proportionality constant B_1, inspired by the work of Sheng, Galbraith and Coton [26] and Beddoes [30]:

$$A = B_1 max(f' - f)\frac{T}{2\pi} \tag{6.5}$$

where f' and f represent the dynamic (f_{dyn}) and static (f_{stat}) separation points respectively,computed using GE2021 .

The reset condition is defined as $\tau_v = T_{res}$, with T_{res} being greater than or equal to 1. Hence, the normal force coefficient generated by the vortex is given by:

$$C_{N_v} = \left| A \sin\left(\frac{2\pi}{T}\left(\alpha(\tau_v = 0) - \alpha(\tau_v = T_{res})\right)\right)\right| \tag{6.6}$$

6.3.1. Delay (d)

As previously discussed in Section 6.2.1.1, the observed delay in the effective angle of attack with increasing reduced frequency (k) has significant implications for the load generation (Section 2.10 and Figure 2.9) and therefore the modelling approach. In the previously discussed formulation, this delay has been incorporated proportionally to a predefined baseline reduced frequency ($k_0 = 0.200$). However, it is crucial to consider whether this delay should exclusively impact the computation of vortex effects or also extend to the calculation of separation lift using the GE2021 model.

By applying the delay solely to the vortex effects, the separation lift, which is determined by the GE2021 model, would remain unaffected by the delayed angle of attack. This approach assumes that the separation characteristics and lift generation mechanisms remain consistent regardless of the magnitude of the reduced frequency and its consequent effective angle of attack delay.

On the other hand, an alternative approach would involve applying the delay to the calculation of separation lift as well. This implies that the delayed effective angle of attack would directly influence the separation behavior and subsequent lift generation predicted by the GE2021 model. This approach acknowledges that the delayed angle of attack affects the flow dynamics as a whole , both separation phenomena and the vortex effects, consequently influencing the resulting lift characteristics.

In order to determine the most appropriate approach, a comparison with the experimental data, including the effects of varying reduced frequency on separation behavior and lift generation, are necessary. Therefore, investigation and validation of the proposed delay model modifications are crucial to ascertain their accuracy and effectiveness in capturing the complex dynamics of reverse flow dynamic stall.

The substantial impact of reduced frequency on the nature of dynamic stall and pressure distribution has been clearly demonstrated (Section 2.2.2). Therefore, the proposed delay was introduced to effectively account for the influence of reduced frequency on reverse flow dynamic stall. To gain deeper insights into the impact of the proposed delay on changing reduced frequencies (k), Cases E ($k = 0.100$), Cases C ($k = 0.160$) and F ($k = 0.309$) were examined.

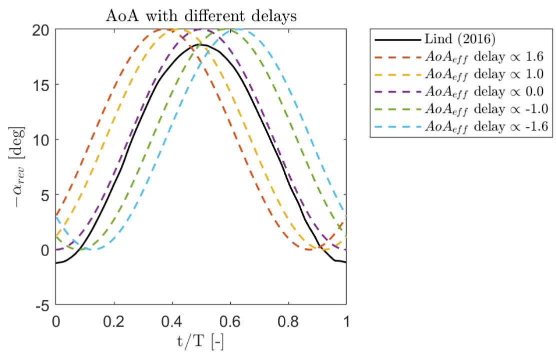

(a) AoA with E delay with different proportionality constants (d).

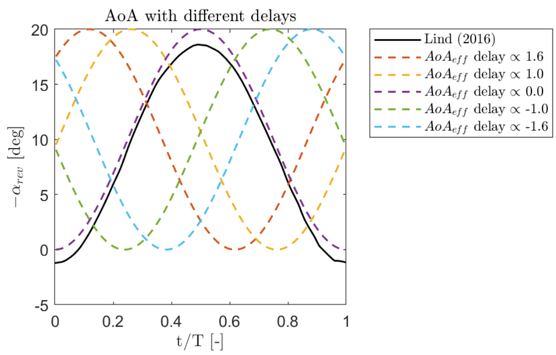

(b) AoA with F delay with different proportionality constants (d).

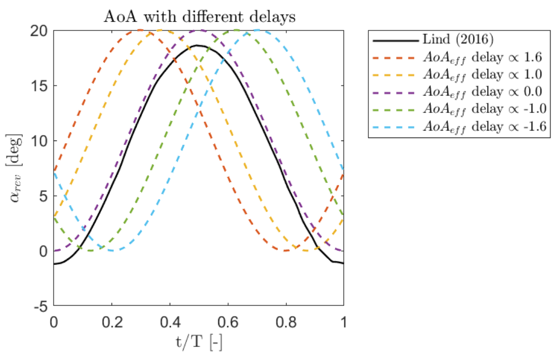

(c) AoA with C delay with different proportionality constants (d).

Figure 6.19: Angle of attack distributions for different values of d.

Observing Figure 6.19, the impact of the reduced frequency and the value for k_0 become evident. As Case F possesses a higher reduced frequency, the angle of attack experiences a more pronounced shift when the delay is applied compared to Case E or C. This was expected as it follows the definition of the new angle of attack distribution.

The use of a full delay, shifts the whole distribution, allowing a closer resemblance to the increment in $-C_L$ caused by the different vortices. However, both grow and decay are delayed, yielding higher loading during the pitch down motion than the one observed in the empirical data. Therefore, the use of a partial delay might be able to provide a lower average error overall, but would not be able to provide a proper qualitative description.

For Cases E and C in Figures 6.20 and 6.21 respectively, the decay in between primary dynamic stall vortex (PDSV) and secondary dynamic stall vortex (SDSV), is limited by the $-C_{L_f}$ value obtained using GE2021. In the literature, the decay between PDSV and SDSV is aggravated by a trailing edge vortex (TEV) that is shed between them. The TEV is not modelled and its modelling could aid in the proper representation of the $-C_L$ drop in between dynamic stall vortices.

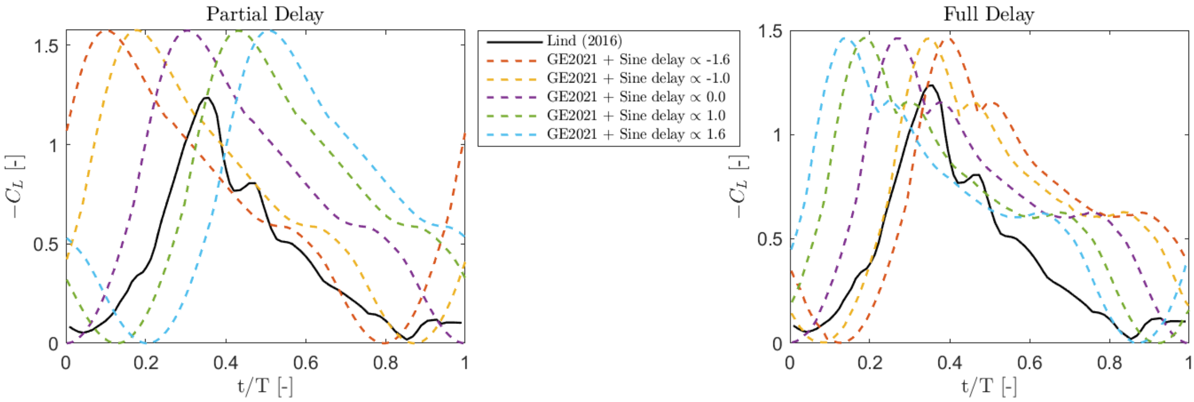

Figure 6.20: Case E ($k = 0.100$) $-C_L$ distribution for Partial (left) and Full delay (right).

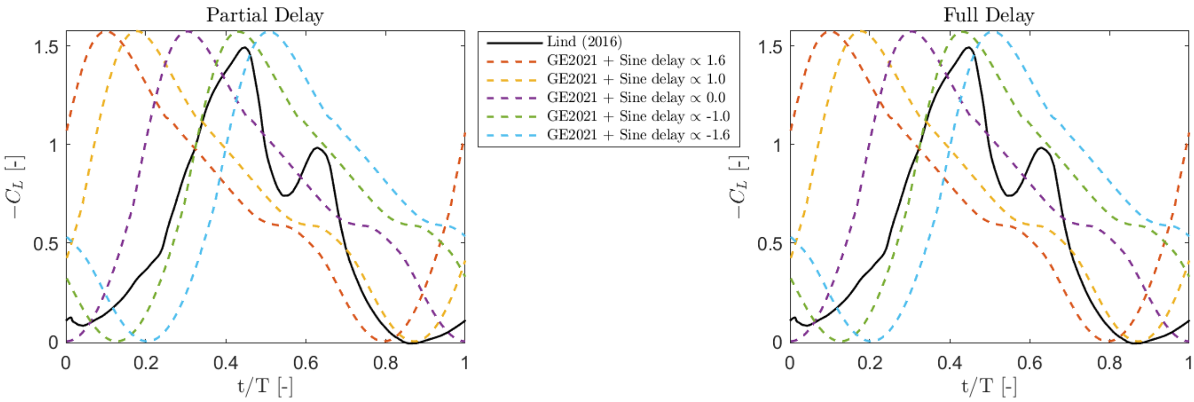

Figure 6.21: Case C ($k = 0.160$) $-C_L$ distribution for Partial (left) and Full delay (right).

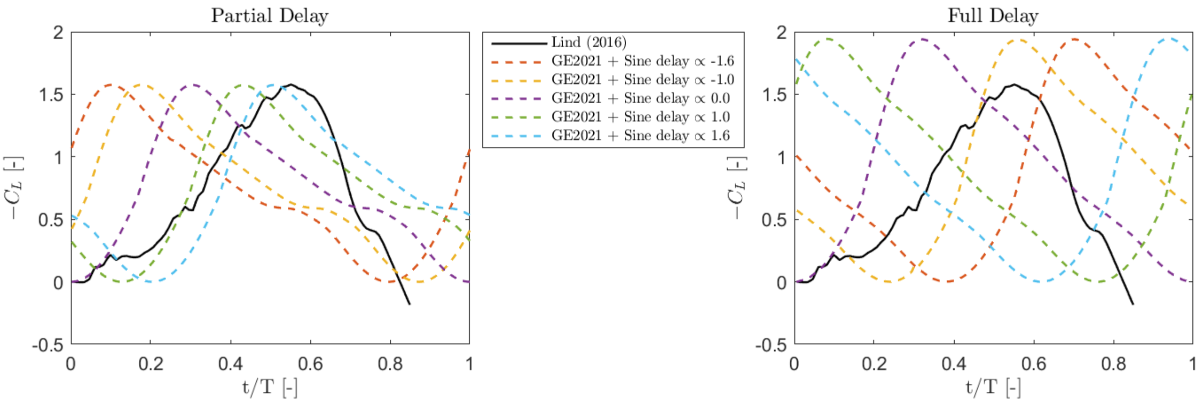

Figure 6.22: Case F ($k = 0.309$) $-C_L$ distribution for Partial (left) and Full delay (right).

In Figure 6.22, Case F is examined, with a higher reduced frequency of approximately $k \approx 0.3$. As mentioned earlier, the impact of delay is anticipated to be more pronounced for this particular case.

When applying a delay constant of $d = -1.0$, the location of the vortex peak is adequately captured. However, the slope during the initial increase in $-C_L$ is not accurately represented, as it occurs at a slower rate than what the model can capture. Conversely, the decay phase happens much more rapidly in the experimental data compared to the results obtained using the model.

To summarize, certain limitations of this simplified vortex effect modelling approach become evident when analyzing the effects of reduced frequency. Specifically, the decay between the primary and secondary dynamic stall vortices is not adequately depicted. This is apparent in Case D (Figure A.10), where the potential decay is constrained by the computation of the separation effect based on the GE2021 model. Moreover, while the absence of a time interval between vortices is not necessarily contradictory to existing literature, it is important to note that the model's failure to account for the TEV occurring between the PDSV and SDSV contributes to the disparity between the model's results and empirical data. Nevertheless, these limitations were already acknowledged in the context of this simplified model. The inclusion of a proportional delay based on reduced frequency provides valuable insights into the behavior of the model.

Appendix A also encompasses the results obtained for Case A and Case D in Section A.2.1. From these results, it appears that a delay proportionality constant of approximately $d = -1.0$ when applied to both separation and vortex effects, allows to capture the number of vortices generated. By considering these findings and the observed model behavior, it becomes clear that further refinement is necessary to address the limitations associated with vortex decay and the temporal spacing between vortices. These improvements are crucial for enhancing the accuracy and fidelity of the model, aligning it more closely with experimental observations and the existing knowledge on reverse flow dynamic stall.

6.3.2. Dynamic Stall Onset (α_{vortON})

In reverse flow, the dynamic stall and flow separation typically occur at low angles of attack due to the presence of a sharp aerodynamic leading edge. As discussed in Section 6.2.1.2, a critical angle of attack (α_{vortON}) at which vortex effects are onset if the airfoil is pitching up was set. For the cases described earlier, several onset angles of attack were examined.

Let's consider Case C, which is depicted in Figures 6.23 and 6.24. Figure 6.23 illustrates the original angle of attack distribution used by Lind, the angle of attack used by GE2021, and the delayed angle of attack applied either partially to the vortex strength or to the overall lift calculation.

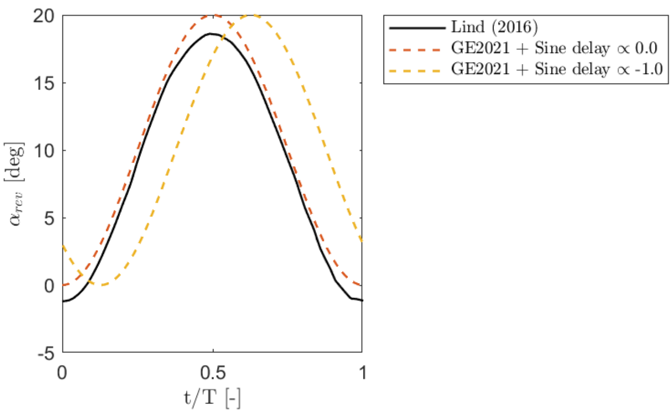

Figure 6.23: Original and delayed AoA for Case C.

Consistently with the experimental data, when applying a full angle of attack delay as observed in Figure 6.24b, if the vortex effects onset condition is set to $\alpha_{vortON} \approx 7.0°$ the model showcases its best performance. However, it is important to note that the model's vortex strength is higher than that observed in the experimental data, indicating a need for tuning.

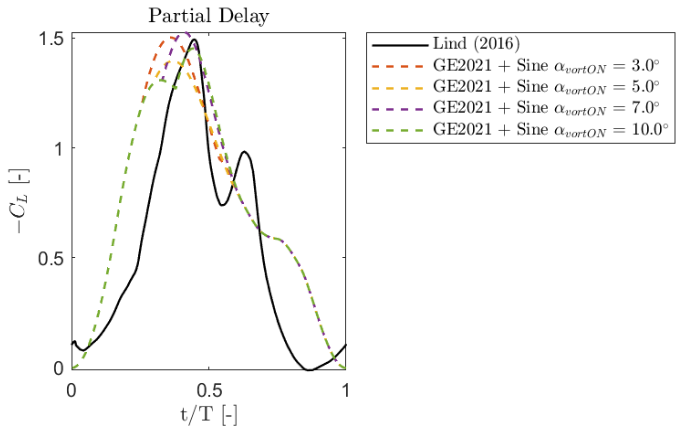

(a) $-C_L$ with Delayed Vortex Effects

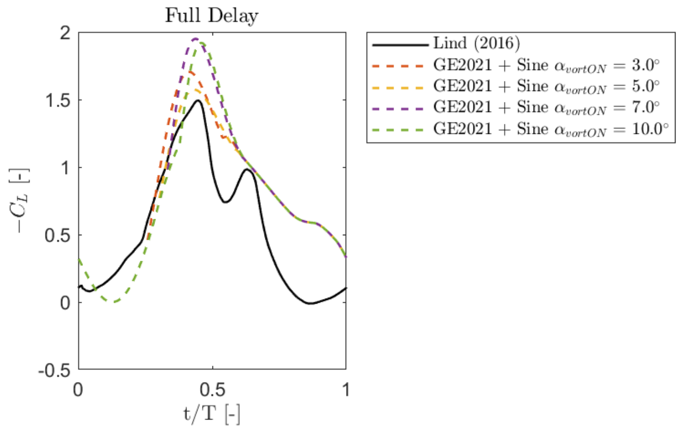

(b) $-C_L$ with Full Delay

Figure 6.24: Case C with different vortex effect onset angle of attack.

It is also important to note that the velocity at which the vortex convects is not fast enough to accurately represent the secondary dynamic stall vortex. However, this can be further tuned using different values of T_{VL} as discussed for the modified SGC model in Section 6.2.1.3. In addition, the lift coefficient resulting from separation effects, which as previously discussed limits the decay, is already higher than the peak generated by the secondary dynamic stall vortex.

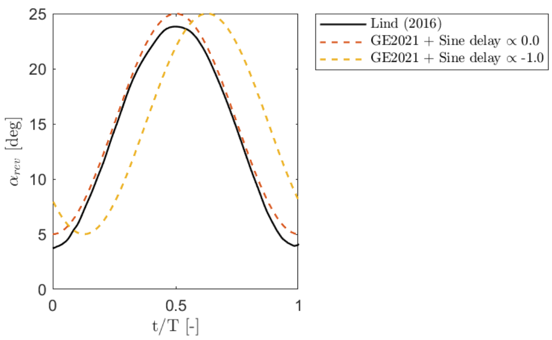

(a) Original and delayed AoA for Case D.

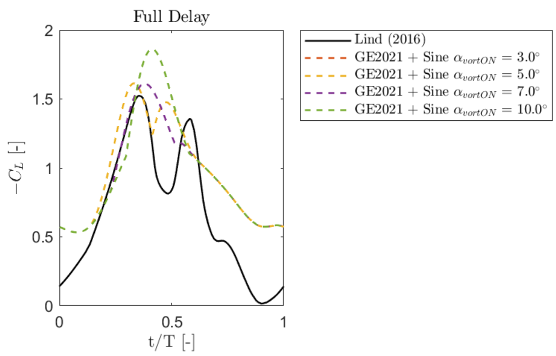

(b) $-C_L$ with Full Delay

Figure 6.25: Case D with different vortex effect onset angle of attack.

To increase the number of generated vortices for a single cycle, the vortex onset condition can be reduced to a lower α_{vortON}. Allowing for earlier development of vortex effects aids in modelling the decay between primary and secondary dynamic stall vortices, and even permits a slight growth in the strength of the secondary vortex in the case of $\alpha_{vortON} = 3.0°$.

Case D presents a similar issue. When the onset angle of attack is set close to $\alpha_{vortON} = 7.0°$, the model captures the increase in lift due to vortex effects more effectively. However, to enable the formation of the secondary dynamic stall vortex, the use of an earlier onset condition becomes necessary. By using $\alpha_{vortON} = 5.0°$ or $\alpha_{vortON} = 3.0°$, the model can represent the presence of the secondary vortex. It is important to note that accommodating the formation of the secondary vortex also means that the decay phase will occur earlier unless adjustments are made to the secondary vortex onset condition.

6.3.3. Vortex Reset condition (T_{res})

The next parameter explored in this study is the vortex reset condition (T_{res}). The angle of attack delay constant was set to $d = -1$ and the vortex onset angle of attack at $\alpha_{vortON} = 5.0°$. The vortex location is tracked using τ_v, defined in Equation 6.1, where T_{VL} allows to regulate the vortex convection speed, which results in a linear variation of the vortex location.

When the vortex location exceeds the reset condition ($\tau_v > T_{res}$) or the airfoil starts pitching down, the vortex is reset to $\tau_v = 0$. If the airfoil is still pitching up and maintains an angle of attack greater than the vortex effect onset angle of attack ($\alpha(t) \geq \alpha_{vortON}$), a second vortex is modelled. It is important to note that in this simplified model, no time is allowed between vortices, which does not accurately depict the loads observed in the empirical data. However, this simplification still provides an overview of the vortex effects observed in a dynamic stall cycle

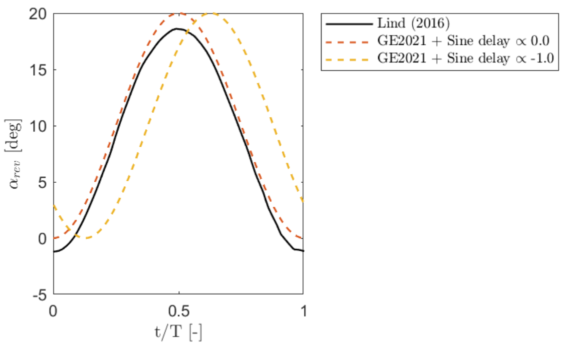

(a) Original and delayed AoA for Case D.

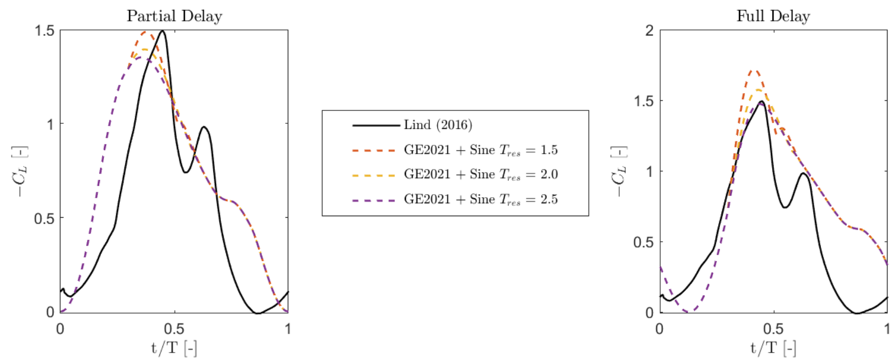

(b) $-C_L$ with Partial (left) and Full Delay (right).

Figure 6.26: Case C with different vortex effect reset condition.

Varying the reset condition can also result in a change in the amplitude of the sinusoidal vortex effect curve. Although the amplitude can be adjusted using the proportionality constant B_1, it is initially defined based on the maximum difference between the dynamic and static separation points in the portion of the cycle affected by the specific vortex. Therefore, modifying the limits of the sinusoidal curve will impact its amplitude.

To properly represent the flow reality of the studied Case C (Figure 6.26), it is necessary to reproduced both primary and secondary dynamic stall vortices in a timely manner. Setting $T_{res} = 2.0$ allows to do so but using a lower T_{res} such as $T_{res} = 1.5$ implies the generation of these vortices earlier in the cycle and limiting their impact.

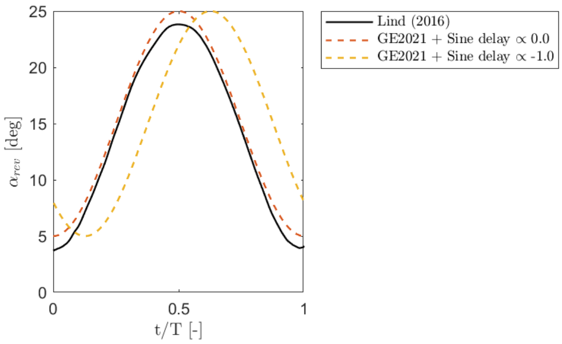

(a) Original and delayed AoA for Case D.

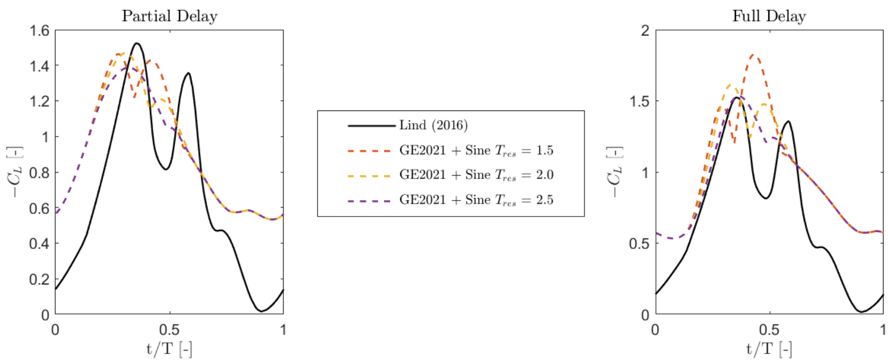

(b) $-C_L$ with Partial (left) and Full Delay (right).

Figure 6.27: Case D with different vortex effect reset condition.

In Case D (Figure 6.27), the limitations of the simplified reset condition become more evident. When using a full delay ($d = -1.0$) and $T_{res} = 2.0$, the amplitudes of the primary dynamic stall vortex (PDSV) and secondary dynamic stall vortex (SDSV) are closer to those displayed by the experimental data but, amplitude can be further tuned using the vortex strength constant B_1. However, the delay between PDSV and SDSV and the stronger decay caused by a trailing edge vortex are nonexistent.

For Case B (Figure 6.28), a larger T_{res} such as $T_{res} = 2.5$, offers results closer to the experimental data as only a single vortex is generated for that pitching cycle. This setting successfully captures the primary dynamic stall vortex and exhibits a small increase in lift coefficient occurring later in the cycle, around $t/T = 0.55$.

The current definition of T_{res} allows for the modelling of multiple vortices while being a simple and computationally efficient. Furthermore, with the appropriate tuning, it has proven its ability to match the number of vortices and generate a similar amplitude of vortex effects when compared to the experimental data. However, the decay phase between vortices is limited by the separation lift values obtained from the GE2021 model, which can impact the accuracy of the vortex effect computation. Moreover, the formulation does not account for the time interval between the primary and secondary dynamic stall vortices. These limitations highlight the need for further improvements and refinements in the modelling approach to capture the complete dynamics of vortex effects in dynamic stall simulations.

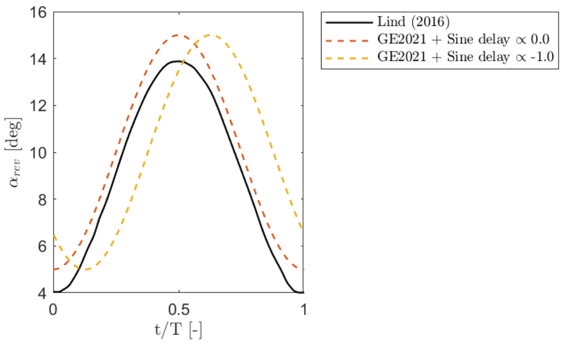

(a) Original and delayed AoA for Case B.

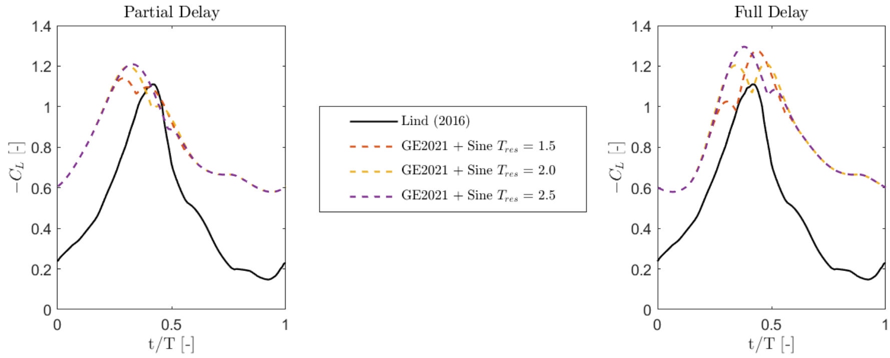

(b) $-C_L$ with Partial (left) and Full Delay (right).

Figure 6.28: Case B with different vortex effect reset condition.

6.3.4. Vortex Strength (B_1)

The initial vortex strength is determined by the maximum difference between the dynamic and static separation points within the defined limits of the sinusoidal curve. However, a proportionality constant B_1 can be used to adjust the modelled strength of the normal force coefficient generated by vortex effects. To study the impact of B_1, the other parameters are set to, an angle of attack delay constant as $d = -1$, a vortex onset angle of attack as $\alpha_{vortON} = 5.0°$, and the reset condition set to $T_{res} = 2$.

In Case C (Figure 6.29), when applying a partial delay, or delay solely to the vortex effects, the vortex effect is improved by using a higher value of B_1, specifically $B_1 = 0.50$. This adjustment yields results in closer alignment with the experimental data, enhancing the representation of the vortex behavior. On the other hand, in the full delay case, a lower value of B_1 is more effective in achieving a closer match to the experimental data. It suggests that the full delay captures the vortex dynamics more accurately, requiring a smaller adjustment to the vortex strength.

Moving on to Case D (Figure 6.30), both the partial and full delay options demonstrate better results when employing an intermediate value of B_1. This indicates that the optimal value of B_1 for modelling vortex effects can depend on the specific case and the degree of delay applied, which would become extremely complex.

These findings highlight the importance of appropriately tuning the proportionality constant B_1 to achieve the desired performance in vortex effects modelling. It is a crucial parameter that allows for tuning the strength of the vortices to align with experimental observations.

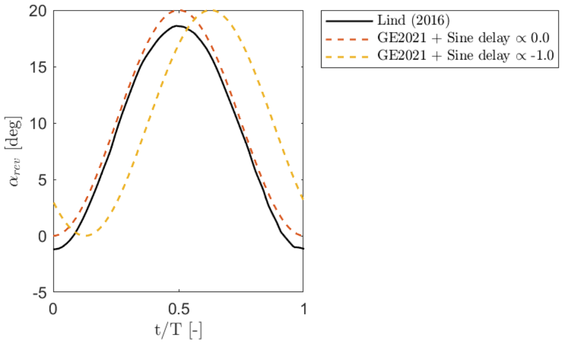

(a) Original and delayed AoA for Case C.

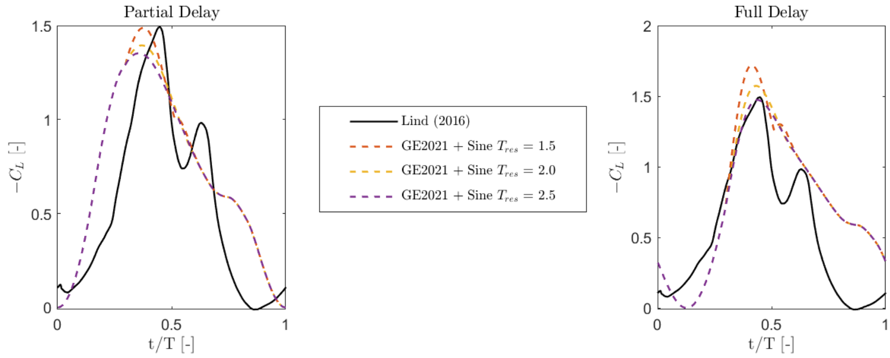

(b) $-C_L$ with Partial (left) and Full Delay (right).

Figure 6.29: Case C with different B_1.

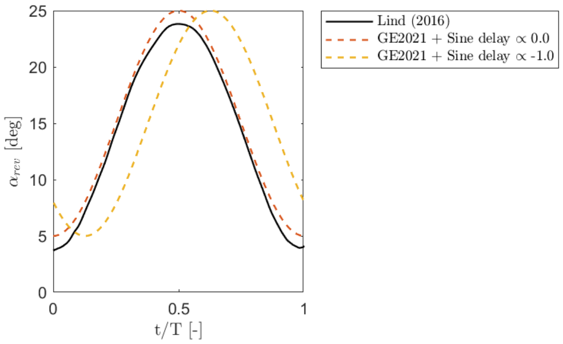

(a) Original and delayed AoA for Case D.

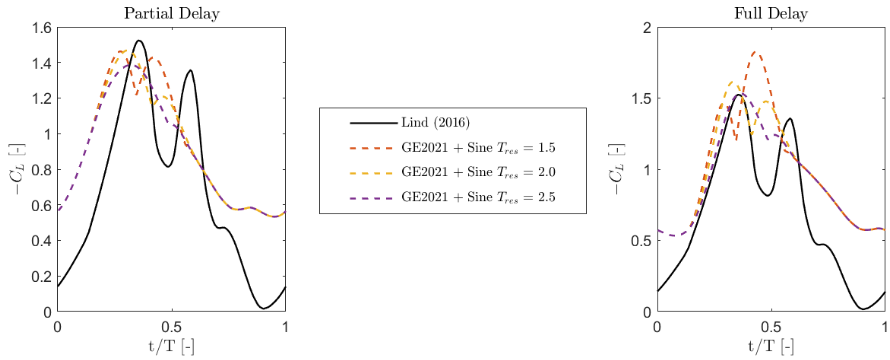

(b) $-C_L$ with Partial (left) and Full Delay (right).

Figure 6.30: Case D with different B_1.

6.3.5. Forward Flow Ramp-up

Similarly to the study performed in Sections 6.1.1 and 6.2.2, the application of the sinusoidal vortex effect in forward flow conditions is now assessed, with an specific focus on the two ramp-up cases used for validation by Beddoes and Leishman [18]. However, in order to determine the parameters that offer optimal performance of this effect in forward flow, it is essential to study the impact and appropriate magnitudes of the delay (d) and vortex onset condition (α_{vortON}). This analysis will ensure that the sinusoidal vortex effect accurately captures the dynamic behavior observed in forward flow applications.

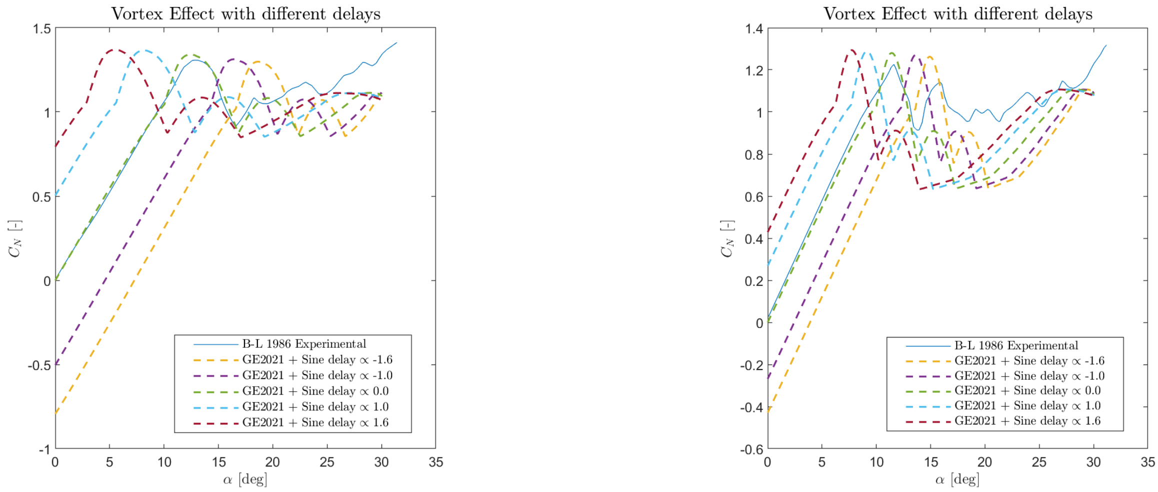

(a) C_N for $M = 0.496$ and $\omega = 1493deg/s$.

(b) C_N for $M = 0.501$ and $\omega = 802deg/s$.

Figure 6.31: Ramp-up cases using full delay with different d.

Figure 6.31 illustrates the impact of the full delay, revealing that the value for the delay that most accurately matches the experimental data is no delay. By using a vortex reset condition of $T_{res} = 1.5$, the angle of attack at which the first and second peaks occur is effectively represented. In addition, when focusing on the vortex effect onset angle of attack α_{vortON}, seen in Figure 6.32, the results that most closely resemble the empirical data are observed at $\alpha_{vortON} = 10°$ for both studied cases. When $\alpha_{vortON} = 10°$, a desirable amplitude and alignment of the first and second C_N peaks are achieved.

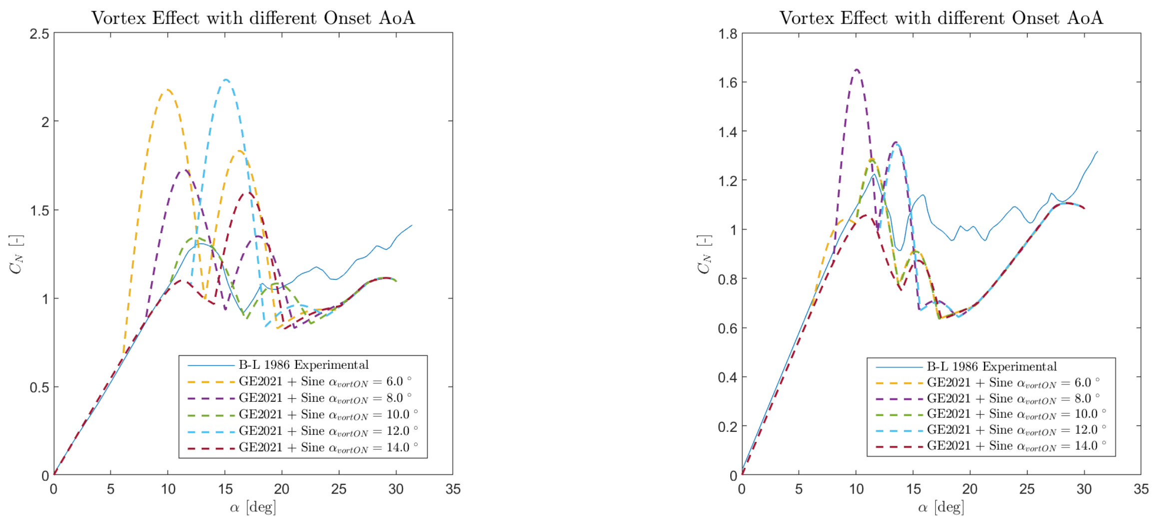

(a) C_N for $M = 0.496$ and $\omega = 1493deg/s$.

(b) C_N for $M = 0.501$ and $\omega = 802deg/s$.

Figure 6.32: Ramp-up cases using different vortex effects onset angle of attack.

Setting a delay proportionality constant of $d = 0$, the vortex effect onset angle of attack to $\alpha_{vortON} = 9°$, a reset condition of $T_{res} = 2.0$, and a vortex effect proportionality constant of $B_1 = 0.7$, the two ramp-up cases were compared to the Beddoes-Leishman model and the experimental data presented in their paper [18]. These parameter values offer a balance between a realistic amplitude for the first peak and accurately capturing the angle of attacks at which both the first and second peaks occur.

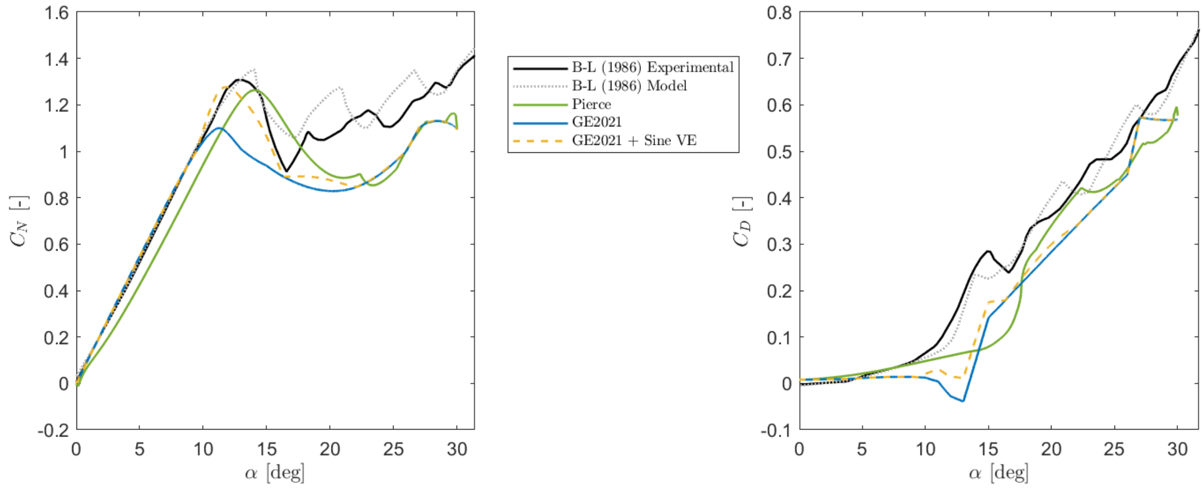

Figure 6.33: C_N for $M = 0.496$ and $\omega = 1493deg/s$ using data from the Beddoes-Leishman [18], the code proposed by Pierce and the GE2021 with sinusoidal formulation of vortex effects.

However, while the magnitude of the first peak is reasonably represented, the magnitude of the second peak remains limited by the baseline magnitude due to separation effects computed using GE2021. Nevertheless, this approach offers results that resemble the experimental results more closely than both GE2021 and Pierce models. In addition, Pierce's formulation of the vortex chordwise effect proves helpful in capturing the oscillations in the drag coefficient more effectively.

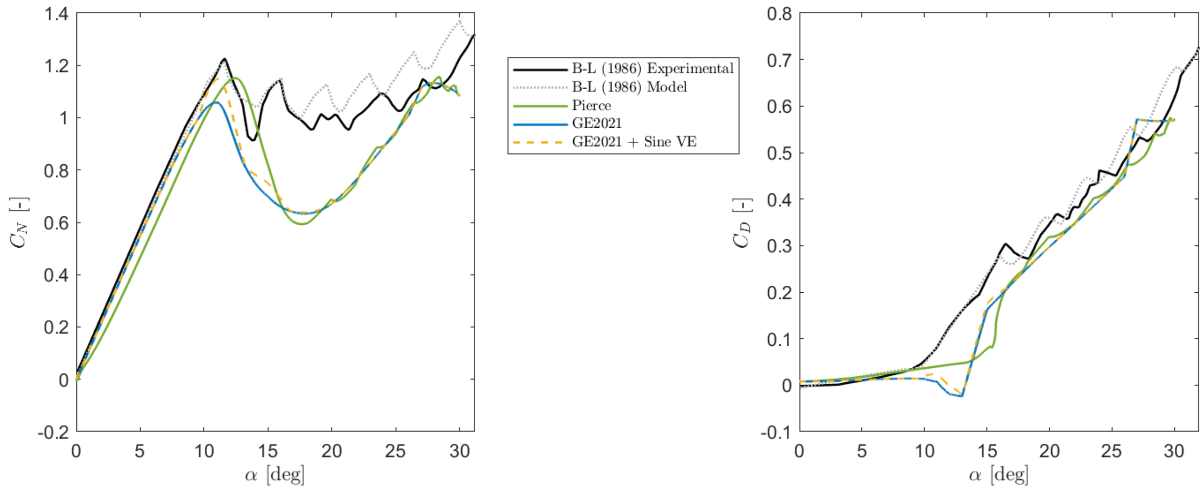

Figure 6.34: C_N for $M = 0.501$ and $\omega = 802deg/s$ using data from the Beddoes-Leishman [18], the code proposed by Pierce and the GE2021 with sinusoidal formulation of vortex effects.

The chosen parameters provide a proper fit for the forward flow ramp-up cases analyzed, with many of them aligning with those that previously already offered results close to those of the empirical data in the previously studied reverse flow cases. However, it is worth noting that while reverse flow dynamic stall modelling benefits from applying a delay, this is not the case for forward flow, where $d = 0$ provided satisfactory results. These discrepancies between forward and reverse flow modelling can pose challenges when using this sinusoidal modelling of the vortex effect to model a wide range of operational conditions in which Horizontal Axis Wind Turbines (HAWTs) are operational.

6.3.6. Optimization

The previous sections aimed to provide insights into the impact of different parameters used in the sinusoidal modelling of vortex effects. However, instead of relying solely on a qualitative assessment to determine which parameter values yield the closest results to the experimental data, three quantitative approaches have been implemented to try to provide a more objective evaluation.

The first approach employs the Euclidean distance metric. In this case, the vector norm between two curves is examined by calculating the square root of the sum of squared differences between corresponding data points:

$$Euclidean = \sqrt{\sum_{i=1}^{N} (experimental_i - model_i)^2} \tag{6.7}$$

The second approach makes use of the mean absolute percentage error (MAPE), which not only assesses the distance between data points but also incorporates normalization based on the magnitude of the experimental data:

$$MAPE = \frac{\sum_{i=1}^{N} \left(\frac{experimental_i - model_i}{experimental_i} \right)}{N} \tag{6.8}$$

The third and last approach employs the root mean square function (RMS) provided by MATLAB to calculate the root mean square error (RMSE), consisting on the difference between the experimental and modelled data:

$$RMSE = rms(experimental - model) = \sqrt{\frac{\sum_{i=1}^{N} (experimental_i - model_i)^2}{N}} \tag{6.9}$$

Making use of these quantitative assessment methods, the performance of the sinusoidal vortex effect modelling technique can be objectively compared against experimental data. These approaches provide a numerical assessment of the differences between the modelled load predictions and the available experimental data, to rigorously evaluate in a quantifiable way the parameter values that yield the closest match to the experimental data.

Table 6.1 presents the results for the studied parameters that affect the sinusoidal vortex effect modelling technique. To evaluate the performance of the model quantitatively, Table 6.2 displays the individual results using different evaluation metrics. Euclidean distance, MAPE, and RMSE are compared against the Lind data [14].

	T_{VL}	d	k_0	α_{vortON}	T_{res}	B_1
Euclidean	11.9032	-2.80154	0.0114684	3.74139	4.56786	0.26152
MAPE	2.10285	0.740143	0.179402	9.72395	1.5414	0.470764
RMSE	12.134	-0.194714	0.0952625	14.9126	2.44009	0.254351

Table 6.1: Optimization results for parameters.

The Euclidean distance approach yields results that closely align with the manually tuned values. However, it is important to note that such a small value for k_0 has a significant negative impact on Case

E and Case F, as evident in Table 6.2. Additionally, the obtained value for T_{res} is the highest among all the approaches used.

The RMSE approach also produces results similar to the manually tuned ones, except for a small delay of approximately $d \approx -0.195$. This particular delay has the most significant impact on Case F, as indicated in Table 6.2. Moreover, the vortex effect onset angle of attack $\alpha_{vortON} \approx 15°$ restricts the representation of vortex effects.

Using the MAPE metric results in a positive delay, contradicting the conclusions reached in the literature. This positive delay has the greatest impact on Case F, where the reduced frequency is the highest and the delay has the most significant effect. However, it should be noted that the value of k_0 obtained using MAPE is closest to the manually defined value.

	Case A	Case B	Case C	Case D	Case E	Case F	Total
Euclidean	5.72184	6.25488	5.59067	5.85501	7.77551	10.52	41.8937
MAPE	0.951903	1.14611	3.7466	2.64964	1.64691	4.86507	15.1621
RMSE	0.274015	0.334456	0.275147	0.324086	0.28922	0.335777	1.95368

Table 6.2: Optimization results for the different cases.

The optimized parameters presented in Table 6.1 have already been discussed in terms of their numerical impact on the different used metrics. However, visualizing the resulting lift and angle of attack distributions can provide further insights. For this purpose, Figures 6.35, 6.36, and 6.37 showcase the obtained results for Cases C, E, and F, respectively, using the optimal parameter values obtained by the various evaluation metrics previously introduced.

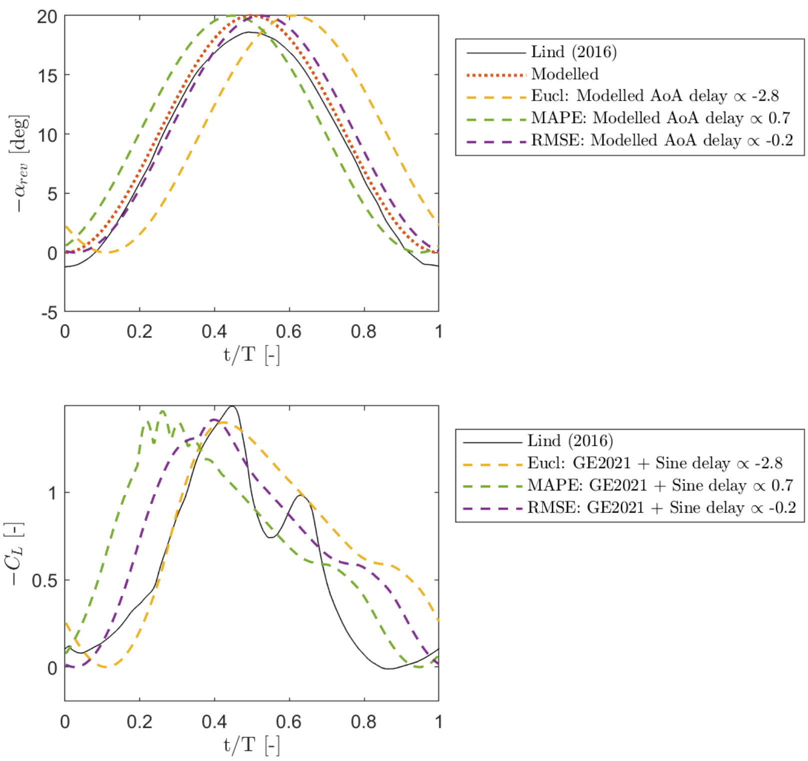

Figure 6.35: Optimized AoA and $-C_L$ distributions for Case C using different evaluation metrics.

By visually assessing the results, a better understanding of the impact of the optimized parameters on the lift and angle of attack distributions. This analysis helps us assess the performance of the sinusoidal vortex effect modelling technique, as well as the used evaluation metrics, in capturing the desired flow characteristics for each specific case.

In Figure 6.35, the results for Case C are displayed, where the reduced frequency is $k = 0.160$. In this case, the small delay constant of $d = -0.2$ obtained using the RMSE approach yields acceptable results, but is unable to model the multiple vortices that are visible in de empirical data. However, the high vortex onset angle of attack condition of α_{vortON} generates a peak that is similar to those produced when the delay only affects the vortex effects.

When using the Euclidean distance approach, the obtained results do not clearly showcase any impact produced by either the primary or secondary vortex. This makes the qualitative analysis of the flow more challenging, as no impact is visually discernible.

It is worth noting that the T_{VL} value obtained using the MAPE approach is significantly lower than the value used to study the effect of the different parameters, which was $T_{VL} = 11$. This, combined with a vortex effect reset condition T_{res} that seemed to yield appropriate results when combined with a larger T_{VL} value, generates several smaller vortices that are not consistent with the experimental data. Furthermore, it is important to note that the use of a positive delay proportionality constant, d, as observed in the MAPE optimization results, goes against the physics of reverse flow dynamic stall.

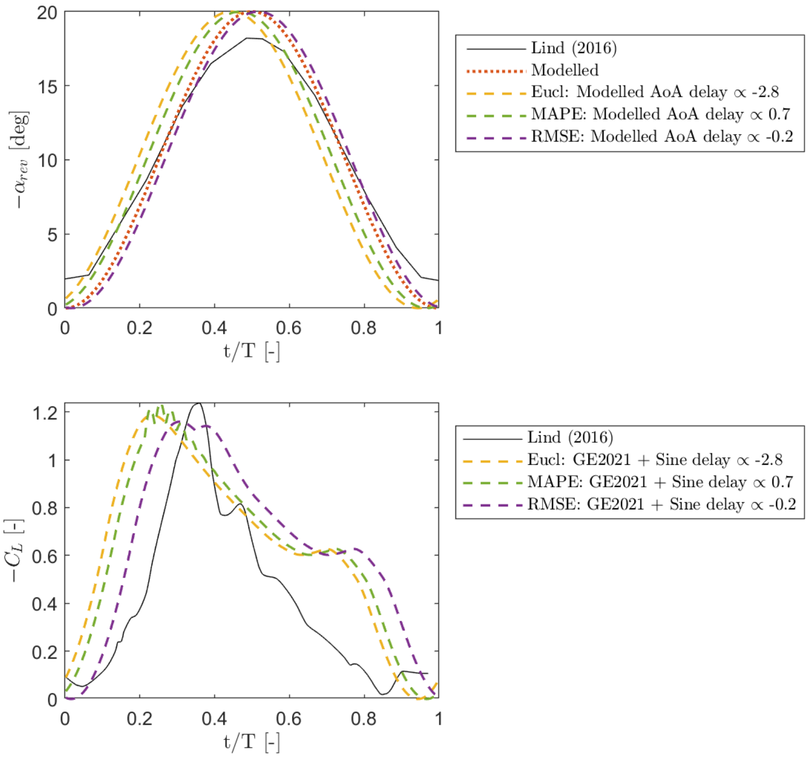

Figure 6.36: Optimized AoA and $-C_L$ distributions for Case E using different evaluation metrics.

The impact of the results obtained from the different optimizations for delay proportionality constant d, become more apparent when assessing the cases with different reduced frequencies. Cases E and F use the same mean angle of attack and amplitude in the sinusoidal pitching motion as Case C, but use $k = 0.100$ and $k = 0.309$ instead of $k = 0.160$ respectively. Therefore, Figures 6.36 and 6.37, which display the results obtained optimizing the parameters involved in the vortex effects modelling with Euclidean, MAPE and RMSE metrics offer better insight on the effect of the obtained parameters.

The use of RMSE as a metric yields as a result for its optimization $d \approx -0.2$ and $k_0 \approx 0.095$. This approach seems to be the better suited to tackle varying reduced frequencies. The first steep increase of lift coefficient occurs earlier in the cycle, not matching the one of the experimental data. These increases still occur within an acceptable range, as the anticipation of the steep increase also means an anticipation in the decay, being the decay closer to the one observed in the experimental data. However, similarly to the results for Case C, the late vortex onset angle does not allow to properly model the primary and secondary vortices allowing for intermediate decay for Cases C and E, and the vortex structure modelled in Case F shows an excessive magnitude but is however not far from the maximum $-C_L$ obtained in the experimental data.

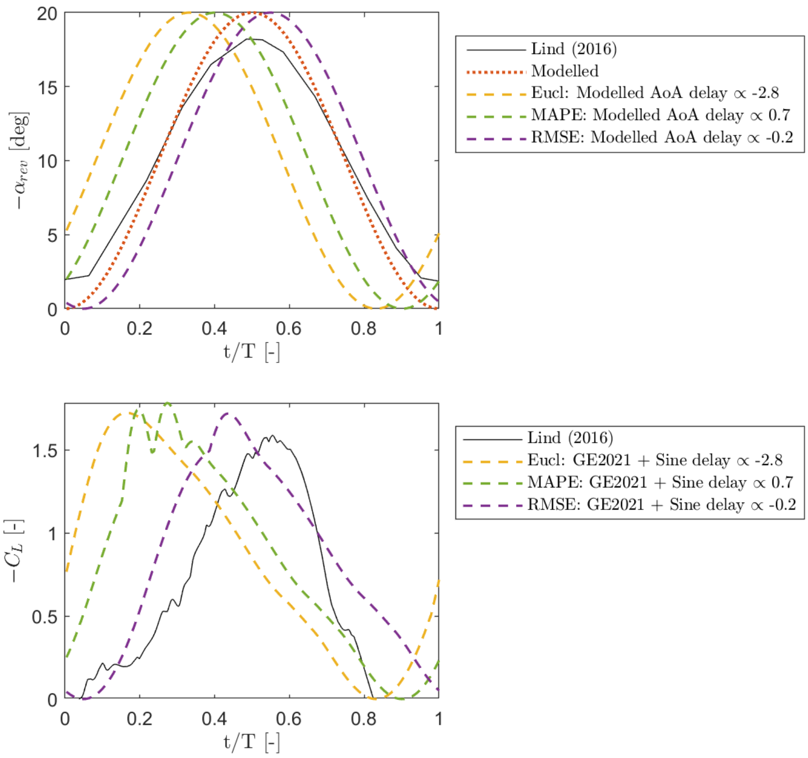

Figure 6.37: Optimized AoA and $-C_L$ distributions for Case F using different evaluation metrics.

The use of MAPE yields the expected results, as the $k_0 \approx 0.18$ it is expected to follow a similar trend to the cases studied in Section 6.3.1. However the delay proportionality constant is positive with $d \approx 0.74$, which is again inconsistent with the results observed in the experimental data. The formation of vortex structures is delayed with increasing reduced frequency, having a positive d would mean the opposite, and the vortices would form earlier with higher reduced frequency. The results for Cases E and F also show the three vortex structures previously mentioned, which again is not the observed trend in the experimental data.

From the results obtained using the Euclidean approach it becomes clear that although applying a delay is necessary, if the value for d becomes excessively high, it might have an undesired behaviour and a negative impact on the final load prediction. Utilizing a large $d \approx -2.8$ and a small k_0 implies that pitching cycles with higher reduced frequencies, the impact of the delay will become exaggeratedly high. The results of the Euclidean evaluation metric portrays this perfectly. Because $k_0 \approx 0.0115$, any reduced frequency will have an excessive effect on the delay. The sinusoidal pitching cycle however, is a periodic function and might therefore accommodate properly for certain values of k. However, in all the studied cases, but more predominately in Case F, represented in Figure 6.37, even if the value of d is negative, the angle of attack distribution is anticipated contrary to the literature.

From these results it can be concluded that none of the metrics implemented can be applied ob- tain optimal values for the parameters involved in the reverse flow dynamic stall. Utilizing the MAPE generates multiple vortex structures that do not represent the reality of this phenomenon. The optimal parameters obtained using the Euclidean metric, opposite to the delay in effective angle of attack observed in the available literature, moves the angle of attack distribution up in the cycle. The RMSE metric offers the necessary angle of attack distribution delay, but the high vortex onset angle of attack $\alpha_{vortON} \approx 14.9$ combined with a relatively high $T_{res} \approx 2.44$ delays the generation of the primary dynamic stall vortex and does not allow for a secondary vortex structure to form. However, the results obtained applying the Euclidean metrics offers results that generally offer a good approximation for the mean value of the overall loading distribution in the pitching cycle and the RMSE metric results could have been improved if further assessment of the impact of the separation and vortex effects in reverse flow dynamic stall was performed. Although the obtained results offer the optimized values to quantitatively represent reverse flow dynamic stall loading distributions, no accurate qualitative assessment can be drawn from the generated load distributions. The computation of the average $-C_L$ distribution can be useful in certain applications however, proper representation of the different vortex generated peaks is crucial to assess the fatigue HAWT blades suffer during their lifetime.

7

Modelling Results and Validation

After the individual analysis and verification of the proposed modifications to the GE2021 model, which only tackled flow separation effects, adding vortex effects was analyzed in Chapter 6, the more established Pierce [17] and GE2021 models were compared to these modified GE2021 models that included the vortex effects using three different formulations. The first is ”GE2021 + Pierce VE”, uses the original formulation of vortex effects implemented in the Pierce model [17], which coincides with that of the original Beddoes-Leishman model [18]. This allows to assess the performance of the highly established and widely used Beddoes-Leishman model for reverse flow conditions, while adding the impact of the vortex effects on the chordwise direction implemented by Pierce. The second, “GE2021 + SGC Mod. VE”, uses the a sinusoidal formulation to model vortex effects, implemented by Sheng, Galbraith and Coton [26], and initially proposed by Beddoes [30]. The third, “GE2021 + Sine VE”, makes use of a further simplified sinusoidal model that reuses the calculation of the inviscid lift from GE2021 is also studied (”GE2021 + Sine VE”).

”GE2021 + SGC Mod. VE” and ”GE2021 + Sine VE” utilize the same parameters described in section 6.2.1 to define the vortex development and its impact on the normal force. However, the used optimization procedure investigated in Section 6.3.6 did not yield the desired results, and went against the flow physics in some of the studied cases. Therefore, values that produced results aligned to those of the empirical data were selected for this final comparison and are included in Table 7.1. The same delayed angle of attack distribution was used for both models therefore, the values for the delay proportionality coefficient d as well as the baseline reduced frequency $k_0 = 0.200$ were equal for both models. Forward flow (FF) and reverse flow (RF) onset vortex effects angle of attack (α_{vortON}) were set independently while remaining consistent to the available experimental data.

	d	$FF\ \alpha_{vortON}$	$RF\ \alpha_{vortON}$	T_{VL}	T_{res}	B_1
GE2021 + SGC Mod. VE	-1	$9.5°$	$7°$	9	2	0.35
GE2021 + Sine VE	-1	$9.5°$	$7°$	11	1.5	0.15

Table 7.1: Values used for the different parameters used in ”GE2021 + SGC Mod. VE” and ”GE2021 + Sine VE” .

7.1. Reverse Flow

The focus of this study was to assess the performance of Beddoes-Leishman type models for reverse flow dynamic stall modelling. To do so, the proposed models have been compared to those researched by Lind [14] and presented in Table 5.1. In this section, the aim will be to produce a final assessment of the performance of the established and modified models presented throughout this document.

GE2021 does not model vortex effects which have been shown to be the most relevant phenomena in reverse flow dynamic stall according to the literature. Thus, its inability to capture the oscillations observed in the empirical $-C_L$ distributions are expected. However, the model developed by Pierce includes the modelling of vortex effects but proves to be unable to capture the multiple vortices being generated in reverse flow conditions. Furthermore, both Pierce's and GE2021 face the same limitation previously discussed in Section 5 (Figure 5.6) observed in Cases B and D, when for angles of attack close to $\alpha_{rev} \approx 5°$, the modelled results are higher than those obtained by Lind because the static polar is used to obtained the inviscid lift later used in the formulation of the separation effects.

As also discussed beforehand, this limitation in the formulation of the GE2021 model translates to the new models with added vortex effects, as these are additions made upon the existing GE2021 to provide improvements. Therefore, the "GE2021 + Pierce VE" model poses similar limitations as those generated by the Pierce model. The addition of the vortex effects with the approach used in the Pierce model falls short on the multiple vortex modelling requirements of reverse flow dynamic stall.

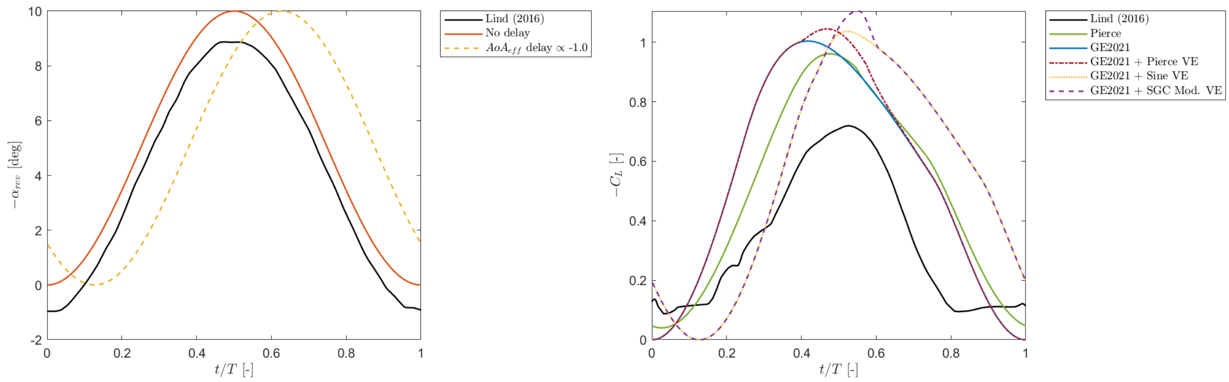

Figure 7.1: AoA and $-C_L$ distributions for Case A.

In Cases A and B, the maximum angle of attack does not exceed $\alpha_{rev} < 15°$, making them the two cases with a single dynamic stall vortex for a reduced frequency of $k = 0.160$. However, literature demonstrated flow separation in reverse flow dynamic stall takes place at angles of attack near $\alpha_{rev} \approx 7°$. Therefore, the vortex onset condition is triggered for both "GE2021 + SGC Mod. VE" and "GE2021 + Sine VE". This generates a clearly visible peak in $-C_L$ for Case A (Figure 7.1), produced by the "GE2021 + SGC Mod. VE" model. In the case of the "GE2021 + Sine VE" model, although vortex effects are triggered, the vortex generated effects are less prominent. In addition, for both these models, generate a secondary dynamic stall vortex for Case B (Figure 7.2), which does not match the empirical observations drawn by Lind [14].

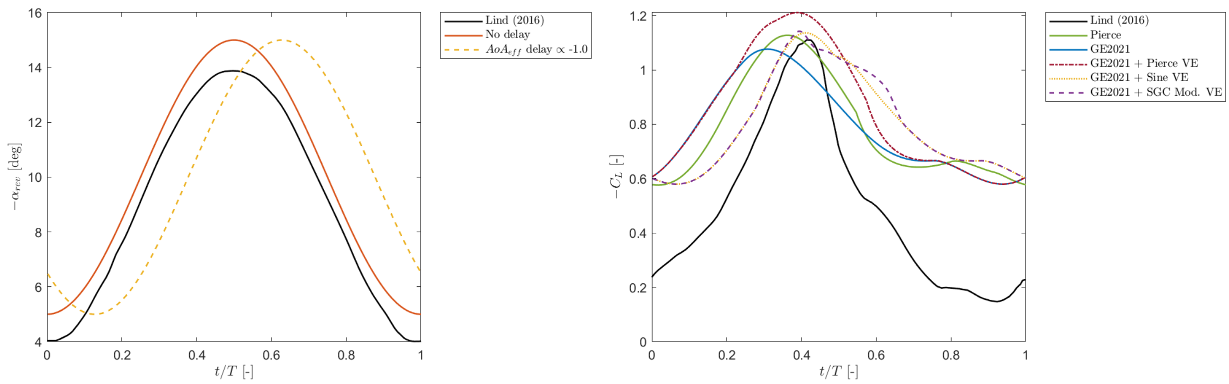

Figure 7.2: AoA and $-C_L$ distributions for Case B.

Nevertheless, the secondary dynamic stall vortex generated by “GE2021 + Sine VE” affects a shorter section of the cycle than the one generated by “GE2021 + SGC Mod. VE”. To help visualize the reason behind this, Figure 7.3 shows the vortex position τ_v and the computed vortex lift C_{L_V}. “GE2021 + Sine VE” calculates the C_{N_V} within the segments delimited between $\tau_v = 0$, this means that the rise and decay of the vortex occurs between the $0 < \tau_v < T_{res}$. Although this allows for more control of the portions of the cycle affected by each individual vortex, no time in-between vortices is allowed.

In the case of “GE2021 + SGC Mod. VE”, the shape function of normal force due to vortex effects V_x is allowed to increase between $0 < \tau_v < 1$ and the decay occurs when $1 < \tau_v$ or when the airfoil starts pitching down, which is an offset condition that sets τ_v to zero for both “GE2021 + Sine VE” and “GE2021 + SGC Mod. VE”. However, while in the case of the “GE2021 + Sine VE”, decay is not allowed to occur past the offset condition, in the case of “GE2021 + SGC Mod. VE”, if the vortex had not reached the trailing edge ($\tau_v = 1$) by the time the airfoil starts the pitch-down motion, the vortex will decay past that offset condition, to allow for a steady decay.

Combining the information from the literature, available in Figures 2.9 and 2.10, vortex induced peaks in $-C_L$ can be observed after the effective angle of attack shows a pitch down motion for the case that uses $k = 0.160$. However, this does not seem to occur for those with $k = 0.100$ and $k = 0.309$. Therefore, based solely on the available empirical data, it is not possible to determine what model has a more realistic approach to vortex decay.

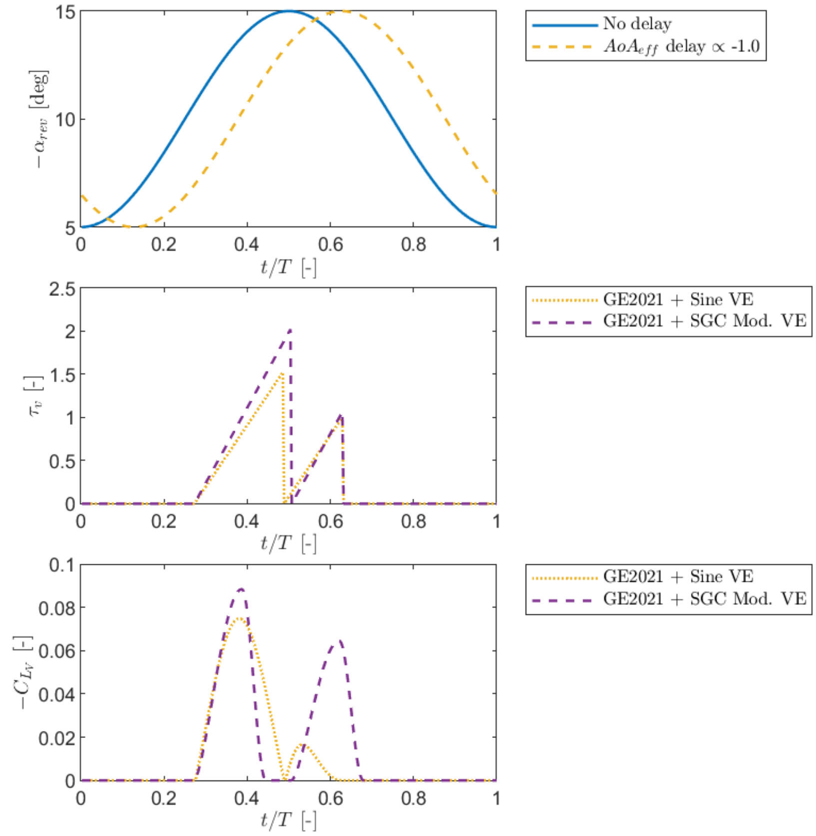

Figure 7.3: AoA, τ_v and $-C_{L_V}$ distributions for Case B.

Case D has the maximum angle of attack studied with a mean pitching angle of attack of $\alpha_m = 15°$ and an amplitude of $\alpha_a = 10°$. Therefore, the generation of multiple vortices is expected, and can be observed in the two clear peaks in $-C_L$ in Figure 7.4. However, from the same figure, it becomes clear that none of the studied models are able to reflect this case accurately. While GE2021, Pierce and their combination, are unable to reproduce the occurrence of the secondary vortex effects, both “GE2021 +

Sine VE" and "GE2021 + SGC Mod. VE" present minor improvements, although still not sufficient.

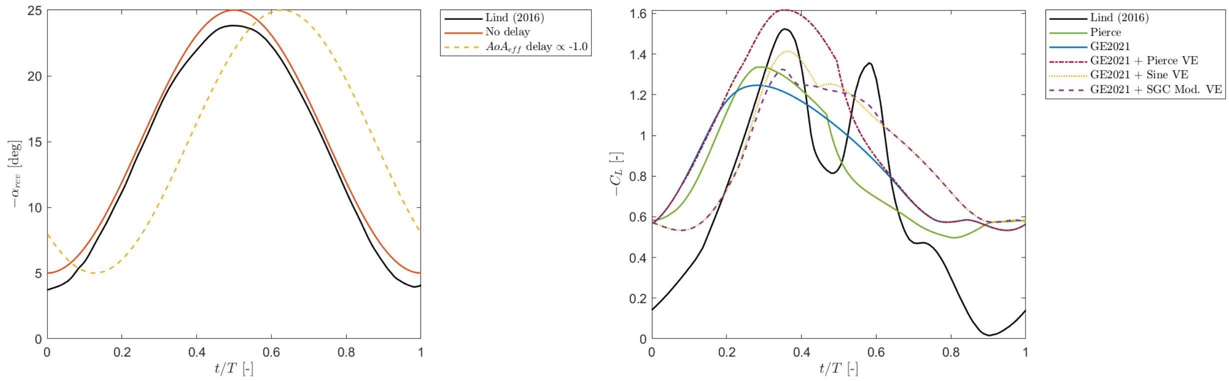

Figure 7.4: AoA and $-C_L$ distributions for Case D.

To understand more clearly the root of this misrepresentation, Figure 7.5 shows that although two vortices are tracked by both "GE2021 + Sine VE" and "GE2021 + SGC Mod. VE", the amplitude of the resulting $-C_{L_V}$ for the secondary dynamic stall vortex is limited by the difference between the dynamic and static separation points, which is close to zero in the portion of the cycle when the secondary dynamic stall vortex is generated.

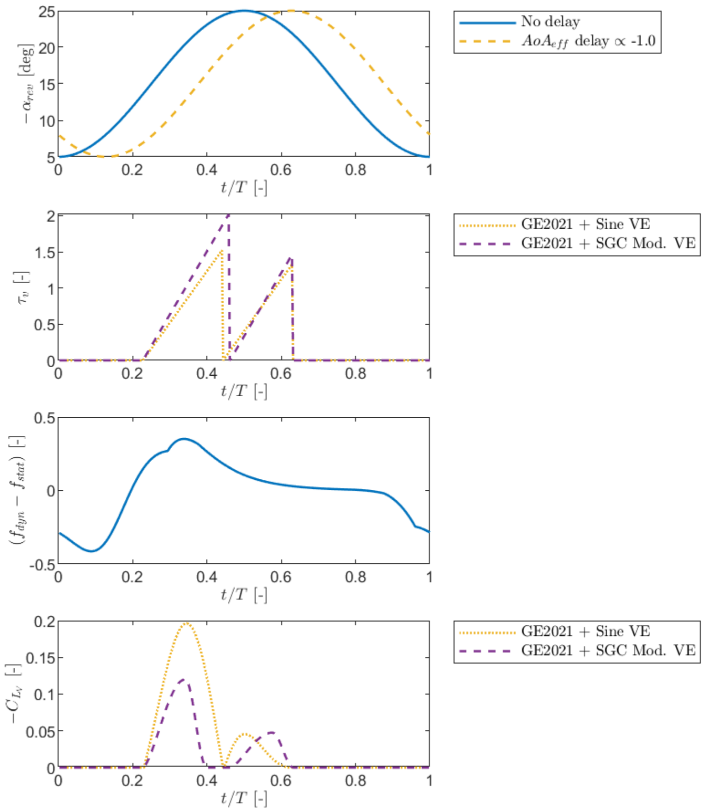

Figure 7.5: AoA, τ_v and $-C_{L_V}$ distributions for Case D.

To conclude with the study of reverse flow, ability to model the implications of the different pitching reduced frequencies will be studied. It is important to note that, while cases A, B, C and D, have a reduced frequency of $k = 0.160$, Cases E and F follow the same angle of attack distribution as case C but have a reduced frequency of $k = 0.100$ and $k = 0.309$ respectively. Therefore, cases E, C and F, will be used to analyse the impact of the proposed improvements.

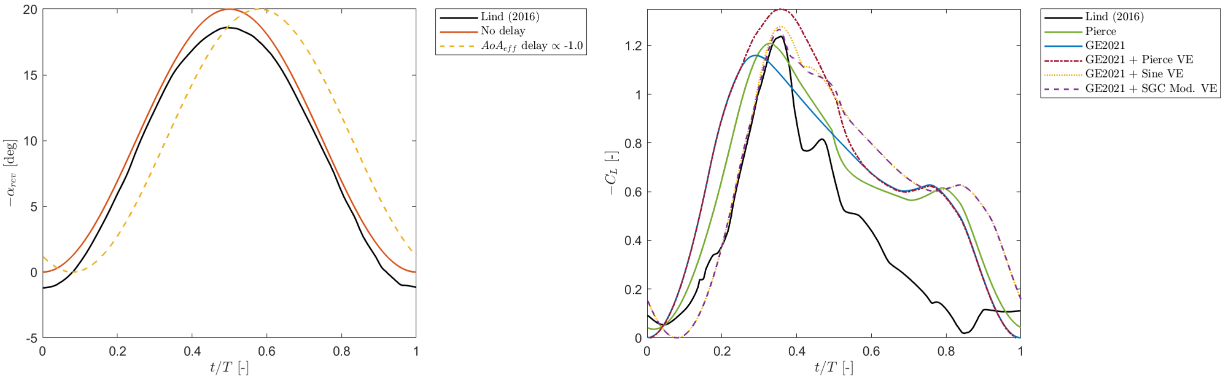

Figure 7.6: AoA and $-C_L$ distributions for Case E.

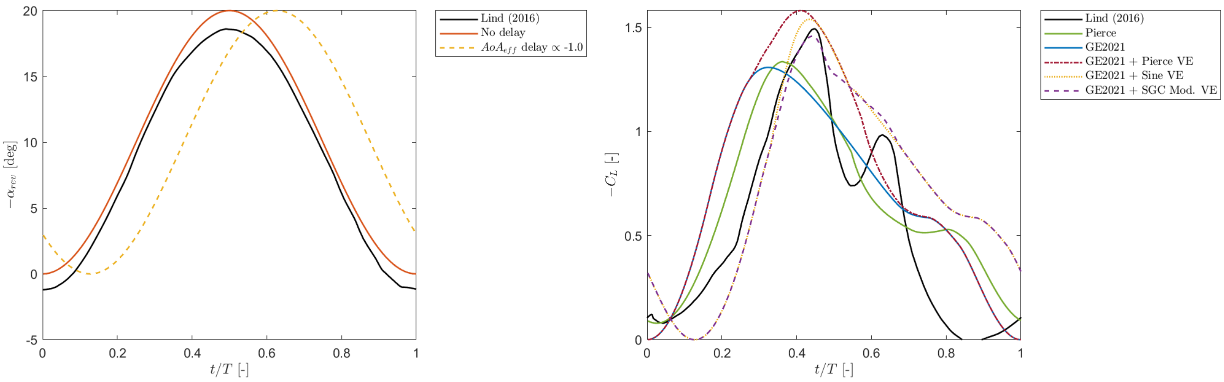

Figure 7.7: AoA and $-C_L$ distributions for Case C.

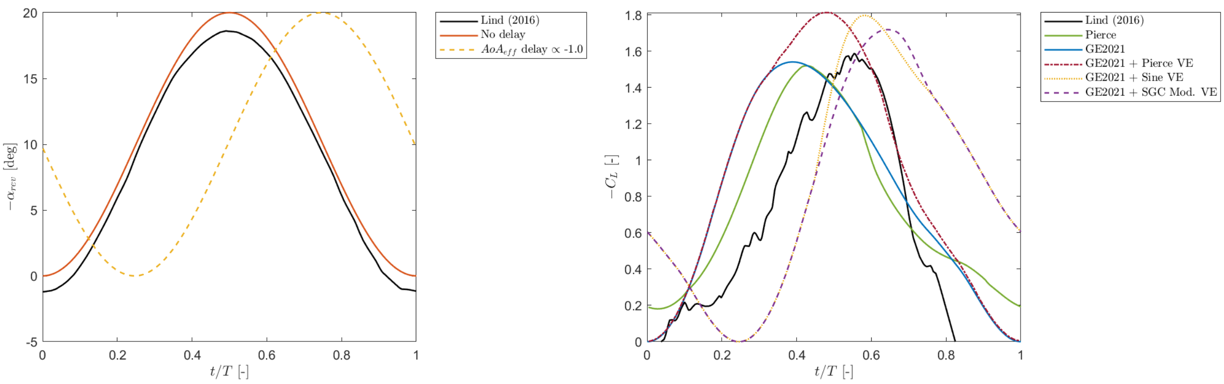

Figure 7.8: AoA and $-C_L$ distributions for Case F.

As previously discussed, increasing reduced frequency does not only delay the distribution of the effective angle of attack but also slightly increases its amplitude. To tackle the generated delay, Equation 6.4 was formulated to model a delayed angle of attack. The delayed angle of attack distribution uses a delay coefficient d that was set to $d = -1$, and a base frequency $k_0 = 0.200$ used to scale the impact of the delay proportionally to the reduced frequency of each studied case. Therefore, the expected impact of the delay on the angle of attack will be lower for Cases C and E, where the reduced frequencies are $k = 0.160$ and $k = 0.100$ respectively, and will have a greater impact for Case F which uses $k = 0.309$.

The impact of the reduced frequency on the angle of attack used for models "GE2021 + Sine VE" and "GE2021 + SGC Mod. VE" is clearly visible on Figures 7.6, 7.7 and 7.8. Although for Cases E and C a good agreement between the timing of the generation of the first dynamic stall vortex is obvered between the empirical data and the results obtained using "GE2021 + Sine VE" and "GE2021 + SGC Mod. VE", for Case F the delay is excessive, and further tuning might be necessary to obtain improved results.

Case C showcases a similar limitation to that experienced in Case D, where the difference between dynamic and static separation point locations is close to zero at the portion of the cycle when the secondary dynamic stall vortex is modelled thus, limiting its impact specially when using "GE2021 + Sine VE" as the growth and decay are again limited by the reseet τ_v, and therefore the effect of the SDSV is limited to a smaller portion of the cycle.

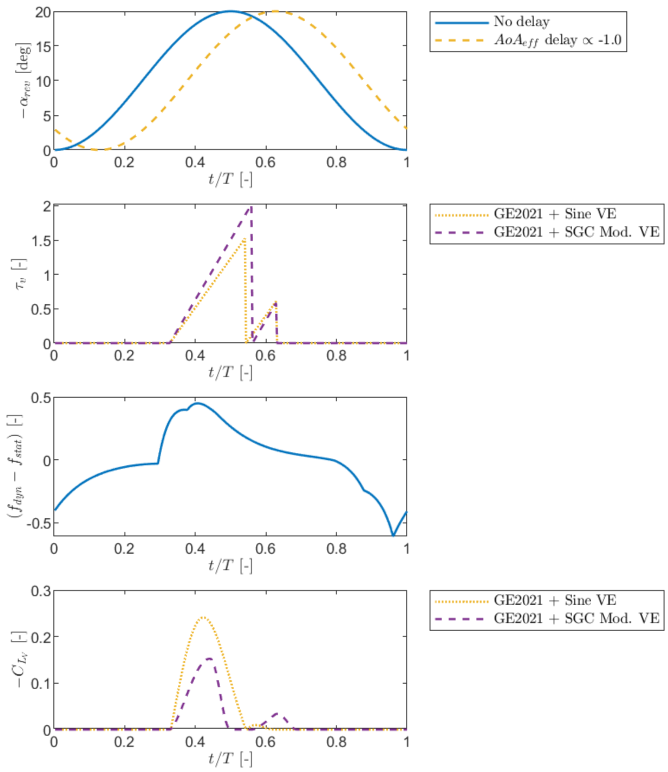

Figure 7.9: AoA, τ_v and $-C_{L_V}$ distributions for Case C.

As previously discussed, the formulation of the delayed angle of attack yields an excessively delayed angle of attack distribution for Case D. In addition to this, the addition of vortex effects, regardless of the type, "GE2021 + Pierce VE", "GE2021 + Sine VE" or "GE2021 + SGC Mod. VE", also yields a greater $-C_L$ than that one observed in the empirical data.

It is also important to note, that the current formulation of vortex effects also limits the decay between primary and secondary dynamic stall vortices, which is not as pronounced as the one observed in the empirical results. However, from the available literature, the greater decay could be caused by the generation and shed of a trailing edge vortex that was not modelled.

7.2. Forward Flow

Modelling dynamic stall conditions for horizontal axis wind turbines is a challenging task as HAWTs operate in rapidly changing conditions and using a wide range of airfoils. Therefore, it is crucial to analyze the performance of the studied models in forward flow. To do so, the models will be compared to the original results provided by Beddoes and Leishman [18]. The performance of the different models in the ramp-up cases in Figures 7.10 and 7.11 were assessed throughout Chapters 5 and 6. Nevertheless, a side-by-side comparison of all the models is still useful to understand the advantages and limitations of each model.

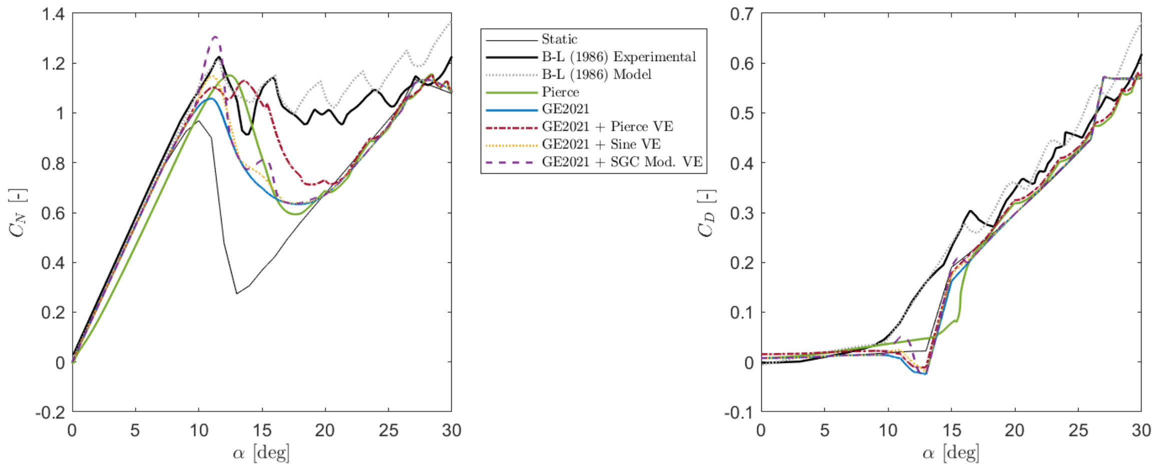

Figure 7.10: C_N and C_D for $M = 0.501$ and $\omega = 802deg/s$ using data from the Beddoes-Leishman [18], the code proposed by Pierce and the GE2021 with various formulation of vortex effects.

For both ramp-up cases, the addition of Pierce vortex effects to the separation effects computed using GE2021, does not offer desirable results. The combination of decay of the separation effects with the increasing vortex effects generates several smaller peaks in C_L that do not match the available experimental data. Pierce is the only studied model that includes a chordwise component of the vortex effects, which positively impacts the obtained C_D results for both the original Pierce and the proposed "GE2021 + Pierce VE".

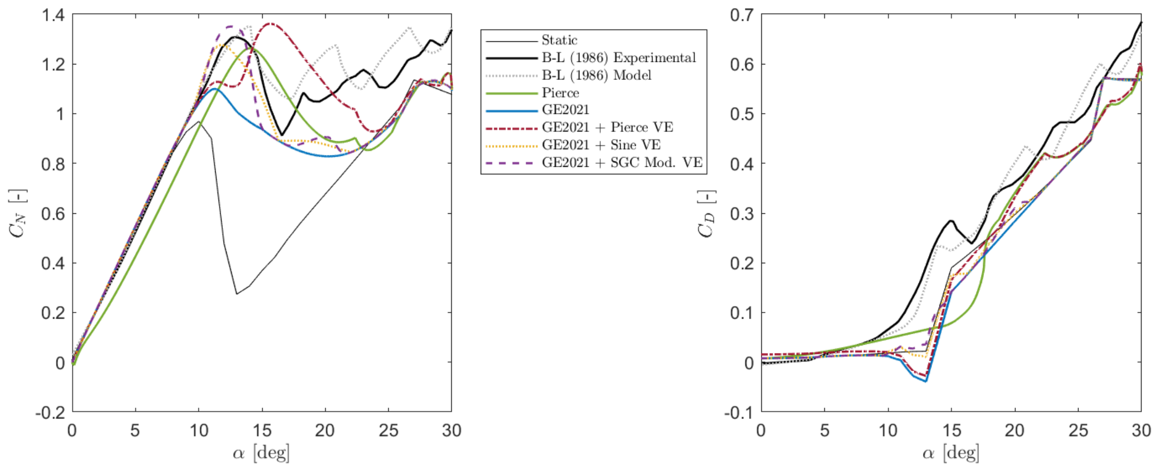

Figure 7.11: C_N and C_D for $M = 0.496$ and $\omega = 1493deg/s$ using data from the Beddoes-Leishman [18], the code proposed by Pierce and the GE2021 with various formulation of vortex effects.

It is important to note that $d = 0$ for both “GE2021 + Sine VE” and “GE2021 + SGC Mod. VE” was applied in forward flow conditions, but the rest of the parameters defined in Table 7.1 remained the same. When using the sinusoidal and the modified SGC vortex effects formulation, the vortex effects diminish with increasing angle of attack. The root of this decrease in the impact of the vortex effects resides on the difference between dynamic and static separation points. This is visible in Figure 7.12, where for angles of attack $\alpha \approx 20°$ this difference is close to zero, thus limiting the vortex effects possible impact.

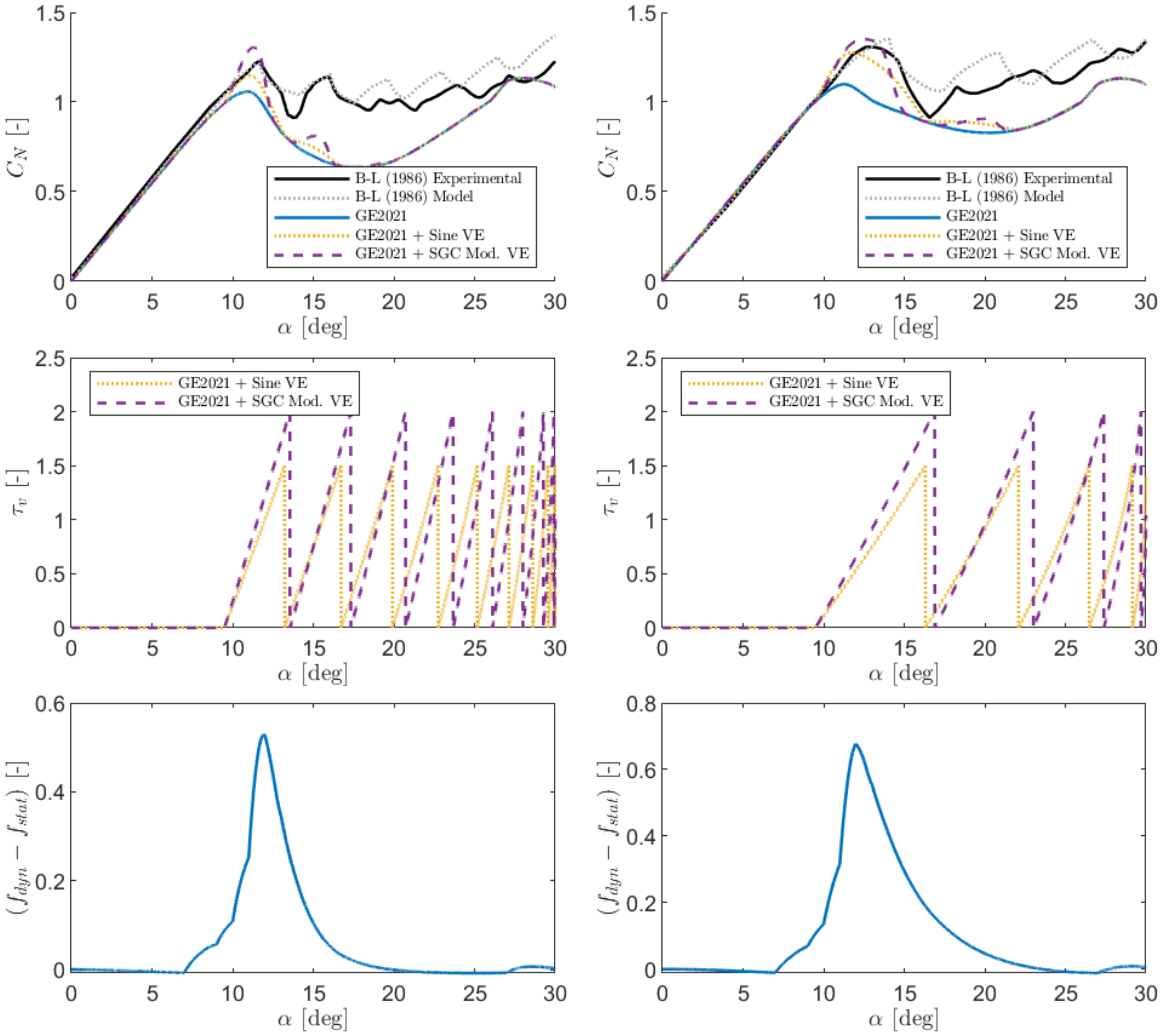

(a) C_N and τ_v for $M = 0.496$ and $\omega = 1493 deg/s$.

(b) C_N and τ_v for $M = 0.501$ and $\omega = 802 deg/s$.

Figure 7.12: Ramp-up cases using different vortex effects onset angle of attack.

Although neither “GE2021 + Sine VE” or “GE2021 + SGC Mod. VE” incorporate chordwise vortex effects, the translation of the effects of the different vortices on the normal force transfers onto the C_D. This offers a small improvement from the original GE2021 model.

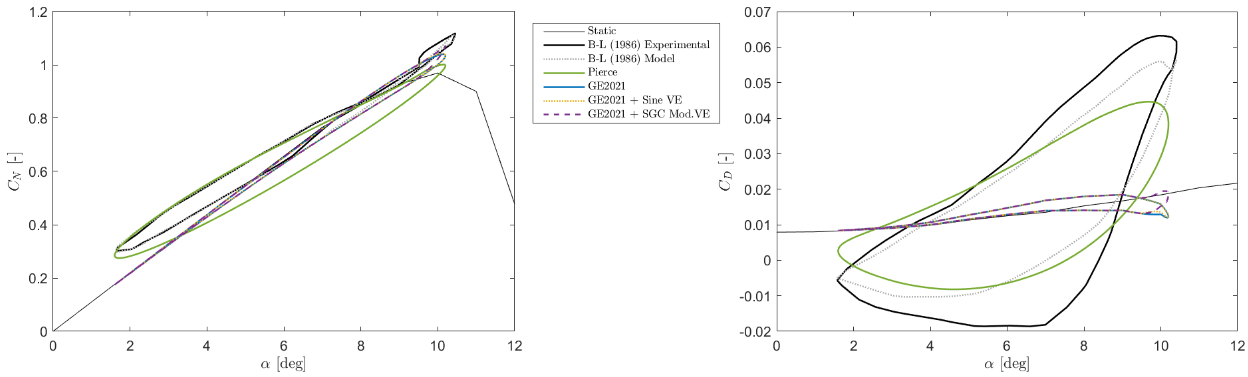

Figure 7.13: C_N and C_D for $M = 0.48$, $\alpha_m = 5.9°$, $\alpha_a = 4.3°$ and $k = 0.146$ using data from the Beddoes-Leishman [18], the code proposed by Pierce and the GE2021 with various formulation of vortex effects.

Two more pitching motions studied by Beddoes and Leishman were analyzed. For both these cases, an improvement is visible for the C_N prediction for larger angles of attack when the vortex effects are added to the original GE2021 model. However, a weak prediction of the drag coefficient is revealed in Figure 7.13, with only the Pierce model being able to come close to the empirical data. Nevertheless, the use of the modified SGC vortex effects provides the most improvement in comparison to the original GE2021 model, as this implementation allows the vortex effects to decay during the pitch down motion. This is a common trait with the use of the Pierce vortex effects that can be observed in 7.14, for which the onset of the vortex effects is close to that one of the sinusoidal or SGC vortex effects, but last for a longer portion of the pitching down motion, offering results closer to those of the experimental data.

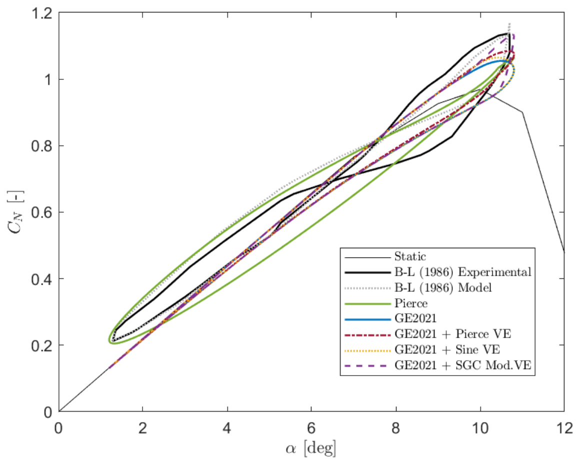

Figure 7.14: C_N for $M = 0.488$, $\alpha_m = 6.0°$, $\alpha_a = 4.8°$ and $k = 0.099$ using data from the Beddoes-Leishman [18], the code proposed by Pierce and the GE2021 with various formulation of vortex effects.

Sheng, Galbraith and Coton looked at cases with deeper stall and low Mach numbers, and therefore the performance of the GE2021 model with added vortex effects were studied. Firstly, the results of the normal coefficient will be discused. When using sinusoidal vortex effects a greater portion of the pitch-up movement is affected by a single vortex. However, this effect is greater than the one observed in the experimental data provided by Sheng, Galbraith and Coton at $10° < \alpha < 18°$, while not matching the vortex effects observed at $18° < \alpha < 20°$. Although the use the modified SGC vortex effects is also unable to match the vortex effects in the $18° < \alpha < 20°$ range, for the lower range of angles of attack in the pitch up motion, the use of modified SGC vortex effects yields results extremely close to those observed in the empirical data. Meanwhile, GE2021 falls short in both the pitch up and the decay, while the Pierce model showcases better performance in the pitch down motion.

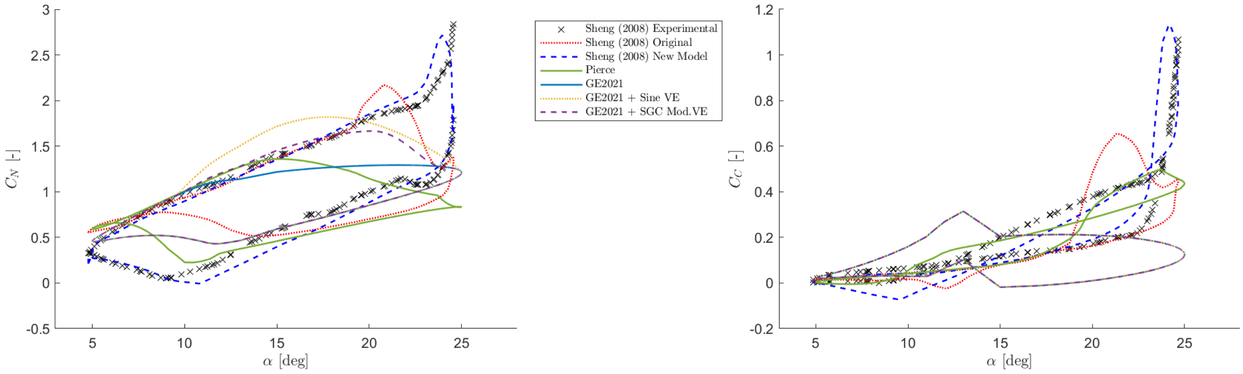

Figure 7.15: C_N and C_C for $M = 0.12$, $\alpha_m = 15°$, $\alpha_a = 10°$ and $k = 0.124$ using data from the study performed Sheng, Galbraith and Coton [26], the code proposed by Pierce and the GE2021 with various formulation of vortex effects.

For this specific case, the insufficient representation of the C_N peak observed on the higher angles of attack by “GE2021 + Sine VE” and “GE2021 + SGC Mod. VE” does not only reside on the difference between dynamic and static separation points. As illustrated in Figure 7.16, using $T_{VL} = 11$ and $T_{VL} = 9$ respectively only allows for a single vortex to be modelled when using “GE2021 + SGC Mod. VE”, and with “GE2021 + Sine VE” the secondary vortex does does not affect a great part of the cycle therefore greatly limiting its impact. In forward flow no delay for the effective angle of attack is considered. However, this case could have benefited from it. Therefore, further assessment of the specific needs for delays in light, deep and reverse flow stalls could be beneficial.

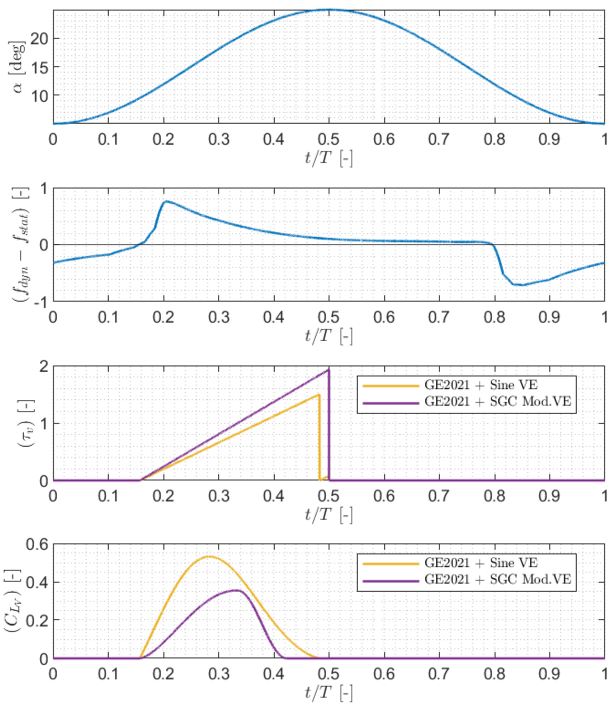

Figure 7.16: C_N, difference between dynamic and static separation point, τ_v and C_{L_V} for $M = 0.12$, $\alpha_m = 15°$, $\alpha_a = 10°$ and $k = 0.124$ using data from the study performed by Sheng, Galbraith and Coton [26], the code proposed by Pierce and the GE2021 with various formulation of vortex effects.

In the case of the chordwise coefficient, GE2021, “GE2021 + Sine VE” and “GE2021 + SGC Mod. VE” showcase the same results as expected, due to the fact that neither accounts for the vortex effects in the chordwise direction. Therefore, Pierce offered better results in the chordwise direction as it is the only implemented model with such effects taken into account.

8
Conclusions and future work

8.1. Conclusions

The objective of the proposed research aimed to assess the strengths and weaknesses of models based on the original dynamic stall model formulation proposed by Beddoes and Leishman [18], and the possible improvements to adapt these to reverse flow dynamic stall conditions. Chapter 2 explores the differences between forward and reverse flow dynamic stall and the main attributes and phenomena that characterize the latter. However, it is important to note that experimental research on airfoils in reverse flow conditions, and specifically in reverse flow dynamic stall is fairly limited, mostly focused on the research developed by Lind for helicopter applications. Nevertheless, this research is extremely detailed and although further testing of cambered and thick airfoils would be desirable, it still allows to create an initial characterization and draw conclusions of the flow physics in reverse flows.

From the literature, it became clear that in contrast to forward flow dynamic stall. Flow separation in reverse flow dynamic stall is triggered by the sharp aerodynamic leading edge and the reduced frequency of the specific cycle has a direct effect on the effective angle of attack experienced by the airfoil. Additionally, vortex effects proved to be the most relevant phenomena in reverse flow dynamic stall. Therefore, analysis of the performance of established models such the one proposed by Pierce [17], the GE2021, and SGC proposed by Sheng, Galbraith and Coton[26] was necessary.

The performance offered by these models in reverse flow conditions was assessed in Chapter 5. Pierce, GE2021, and an available interpretation of the SGC model were tested and the results were compared to pitching motions in reverse flows studied by Lind. These models were not able to provide a proper representation of the multiple vortices formed in a single pitching cycle, as well as the delay caused by increasing reduced frequency. Three vortex effect modelling options were incorporated to the GE2021 model that solely accounted for separation effects. The first was the implementation of Pierce's vortex effects formulation. The second a variation of the Sheng, Galbraith and Coton and Beddoes sinusoidal definition. The third and last consisted on a simplification of the sinusoidal vortex effects formulation.

After the individual analysis and verification of the proposed additions of vortex effects to the GE2021 model in Chapter 6, the more established Pierce and GE2021 models were compared to these GE2021 model modifications, that included the vortex effects using the three aforementioned formulations. The first is ”GE2021 + Pierce VE”, which uses the original formulation of vortex effects implemented in the Pierce model , is very similar to that of the original Beddoes-Leishman model, only adding chordwise effects.

The analysis of the Pierce model and its vortex effects allowed to assess the viability of the highly established and widely used Beddoes-Leishman model for reverse flow conditions. However, as previously observed by the study of the Pierce model, the combination of the GE2021 separation effects with Pierce's vortex modelling was still insufficient to model the multiple vortices generated in some of the studied reverse flow cases. Therefore, models that follow the original Beddoes-Leishman vortex effect implementation are not likely to be adequate options to model reverse flow dynamic stall.

Sheng, Galbraith and Coton proposed the use of a Beddoes formulation [30] to model vortex effects [26]. The original report from Beddoes was not accessible, and therefore, the implementation by Sheng, Galbraith and Coton was the main focus of the analysis and was so referred as SGC. Although the vortex effects sinusoidal implementation was of great interest, the available interpretation of the SGC model implemented by dos Santos and Marques [32] did not yield desirable results. However, the combination of the separation effects with GE2021 and modified sinusoidal vortex effects implementation ("GE2021 + SGC VE") allowed to model several load increments rooted in vortex generation and convection over the airfoil, improving the current GE2021 model. Furthermore, the proposed angle of attack delay provided results that more closely resembled those of the empirical data, although further tuning would still be necessary.

To simplify this last model, a second sinusoidal vortex effects implementation was proposed. With the modified formulation of the GE2021 with added SGC vortex effects, the calculation of the vortex decay could become computationally expensive. Therefore, a similar approach to the one used in the GE2021 model to calculate the inviscid lift was applied in order to calculate the effects of vortices on the normal force coefficient ("GE2021 + Sine VE"). However, this simplification also implied limitations as the vortex effect distribution was not directly linked to the vortex position. This results in consecutive sinusoidal curves that do not closely resemble the experimental data.

Although the available literature also showed that the effective angle of attack was delayed with increasing reduced frequency, and therefore, both separation and vortex effects would be affected by this delay, this simplified model was also used to asses whether the delay should be solely applied to vortex effects or to the whole calculation. This study was developed, as the current GE2021 model has been thoroughly validated, and minimal variations to the current implementation would be desirable to ensure approval of the newly proposed models. From this study, it was concluded that although the GE2021 model is currently used with no delay in the effective angle, the whole model could benefit from the addition of this delay when used to model RFDS, although further tuning is necessary.

After the composition and analysis of the different proposed models, the research questions previously formulated could be answered. As it was visible in the literature, the initiation of flow separation and vortex phenomena begin at low angles of attacked and are triggered by the sharp geometric trailing edge that becomes the aerodynamic trailing edge in reverse flow conditions. Therefore, for the studied cases, the onset conditions used by Pierce were not adequate to represent RFDS. Nevertheless, the addition of the vortex effects using the formulation proposed by Pierce did not include a delay in the angle of attack which could potentially improve its performance. However, this vortex effects formulation is still unable to properly model the studied cases with various generated vortices. On the other hand, the use of a fixed low angle of attack as an onset condition for the SGC and sinusoidal vortex effects modelling techniques, yielded results that resemble the experimental data.

Regarding the differences found in the literature about the vortex speed over the airfoil between forward and reverse flow dynamic stall, all the proposed models used the same vortex speed tuning constant for forward and reverse flows. Through visual inspection of the results the use of the same coefficient in forward and reverse flow to control vortex speed did not seem to have a critical impact on the performance of the studied models. Nevertheless, if the definition of a numerical assessment method was in place, this could be used to draw further conclusions on this issue.

The explicit use of the vortex effects formulation proposed by Pierce, being very similar to the one in the original Beddoes-Leishman model, does not seem to suffice to produce results that resemble the empirical data. On the other hand, the sinusoidal vortex effects modelling options improved on the representation of the several vortices generated in reverse flow dynamic stall. The modelling of separation and vortex effects provided results that closely resemble those of the experimental data, and although trailing edge vortex modelling could possibly improve these results, the current investigation yielded an appropriate performance.

Although the validation data is limited and further research is necessary, it can be concluded from the available results that the vortex effects modelling technique proposed by Sheng, Galbraith and Coton, using a sinusoidal curve, allows to represent the vortex generated loads in RFDS with minimal modifications. This approach yielded better results than the use of Beddoes-Leishman based vortex effects modelling techniques that made use of a deficiency function in RFDS conditions.

In addition, although the original SGC model uses a wide range of airfoil dependent constants, the addition of vortex effects to the GE2021 model did not mean an exaggerated increase in the number of implemented constants. Nevertheless, the dependence of these parameters on the airfoil shapes is still to be determined as further validation data would be required.

8.2. Future Work Recommendations

From these conclusions, recommendations for future work on the topic can be outlined.

- The available literature on reverse flow dynamic stall was extremely restricted, only including experimental data for a thin and symmetrical NACA 0012. This made validation of the proposed models limited, as this airfoil is not representative of the vast range of airfoils used in horizontal axis wind turbines. Therefore, the study of dynamic stall in thicker and cambered airfoils is crucial for the proper development of new modelling techniques. Additionally, a study on the vortex shedding frequency in reverse flow conditions would allow a more accurate prediction of the vortex reset condition.
- The available load distributions for reverse flow dynamic stall focused on lift distributions. Therefore, if more experimental data was available, the research of the effect of dynamic stall vortices on drag would be interesting to assess if the formulation by Pierce could be a good starting point to model these loads.
- The numerical assessment of the proposed models and optimization of the utilized constants came short. Therefore, the implementation of a new evaluation technique would be necessary to offer an objective assessment of the proposed models.
- The available literature clearly depicts the importance of vortex effects in reverse flow dynamic stall. However, the proposed variations of the GE2021 model still use separation effects as the main source of loading. An assessment of the relevance of separation effects relative to the vortex generated effects could enhance the modelled results.
- While rotor sizes increase to capture more energy, the stiffness of rotor blades does not increase proportionally. This causes edgewise vibrations, which have limited aerodynamic damping, to be more likely to generate large dynamic responses that need to be studied and assessed [33]. Therefore, it is necessary to determine the effectiveness of the studied models to model edgewise vibrations.
- In the empirical data obtained by Lind, a fast and strong lift drop between primary and secondary dynamic stall vortices caused by a trailing edge vortex can be observed [14]. However, this effect was not included in the proposed models, limiting their performance. Therefore, including trailing edge vortex effects could provide improvements in reverse flow dynamic stall modelling.

References

[1] M. A. Khan, C. Simão Ferreira, G. J. Schepers, and N. N. Sørensen, "Spectral analysis of New MEXICO standstill measurements to investigate vortex shedding in deep stall," *Wind Energy*, vol. 23, no. 1, pp. 31–44, Jan. 2020, ISSN: 10991824. DOI: 10.1002/we.2409.

[2] "What Is Wind?" National Energy Education Development, Tech. Rep., 2018. [Online]. Available: www.NEED.org.

[3] A. Lind, A. Jones, A. Lind, and A. Jones, "Adaptation of the Leishman-Beddoes Dynamic Stall Model for Reverse Flow," *APS*, E7.001, 2016. [Online]. Available: https://ui.adsabs.harvard.edu/abs/2016APS..DFD.E7001L/abstract.

[4] D. Micallef and T. Sant, "A Review of Wind Turbine Yaw Aerodynamics," *Wind Turbines - Design, Control and Applications*, Jul. 2016. DOI: 10.5772/63445.

[5] M. A. Khan, "Dynamic Stall Modeling for Wind Turbines," Tech. Rep. [Online]. Available: http://repository.tudelft.nl/..

[6] J. Anderson, *Fundamentals of Aerodynamics*, 6th ed. McGraw-Hill Education.

[7] W. J. Mccroskey, "The Phenomenon of Dynamic Stall," Tech. Rep.

[8] K. W. Mcalister, L. W. Carr, and W. J. Mccroskey, "Dynamic Stall Experiments on the NACA 0012 Airfoil," NASA Ames Research Center, Tech. Rep., Jan. 1978.

[9] L. W. Carl, K. W. Mcalister, and W. J. Mccroskey, "Analysis of the development of dynamic stall based on oscillating airfoil experiment," 1, Tech. Rep., 1977.

[10] A. H. Lind and A. R. Jones, "Unsteady aerodynamics of reverse flow dynamic stall on an oscillating blade section," *Physics of Fluids*, vol. 28, no. 7, Jul. 2016, ISSN: 10897666. DOI: 10.1063/1.4958334.

[11] J. G. Leishman, "Challenges in modeling the unsteady aerodynamics of wind turbines," in *ASME 2002 Wind Energy Symposium, WIND2002*, 2002, pp. 141–167, ISBN: 156347476X. DOI: 10.1002/we.62.

[12] A. H. Lind and A. R. Jones, "Title of dissertation: An Experimental Study of Static and Oscillating Rotor Blade Sections in Reverse Flow," University fo Maryland, Tech. Rep., 2015.

[13] A. H. Lind, L. R. Smith, J. I. Milluzzo, and A. R. Jones, "Reynolds number effects on airfoils in reverse flow," *53rd AIAA Aerospace Sciences Meeting*, 2015. DOI: 10.2514/6.2015-1973. [Online]. Available: https://arc.aiaa.org/doi/10.2514/6.2015-1973.

[14] A. H. Lind and A. R. Jones, "Unsteady airloads on static airfoils through high angles of attack and in reverse flow," *Journal of Fluids and Structures*, vol. 63, pp. 259–279, May 2016, ISSN: 10958622. DOI: 10.1016/J.JFLUIDSTRUCTS.2016.03.005.

[15] J. G. Lesihman, *Principles of Helicopter Aerodynamics (Cambridge Aerospace Series)*, Second Edition. 2006, ISBN: 978-0-521-85860-1.

[16] A. Bjorck, "DYNSTALL: Subroutine Package with a dynamic stall model," The Aeronautical Research Institute of Sweden, Tech. Rep., 2000. [Online]. Available: www.stem.se.

[17] K. G. Pierce, "Wind Turbine Load Prediction using the Beddoes-Leishman Model for Unsteady Aerodynamics and Dynamic Stall," Ph.D. dissertation, The University of Utah, Aug. 1996.

[18] J. G. Leishman and T. S. Beddoes, "A Semi-Empirical Model for Dynamic Stall," *Journal of the American Helicopter Society*, vol. 34, no. 3, pp. 3–17, Aug. 1986, ISSN: 2161-6027. DOI: 10.4050/JAHS.34.3.3.

[19] C. Tran and D. Petot, "Semi-empirical model for the dynamic stall of airfoils in view of the application to the calculation of responses of a helicopter blade in forward flight.," 1980.

[20] K. W. McAlister and D. Petot, "NASA Technical Paper AVSCOM Tech nica I Report Application of the ONERA Model of Dynamic Stall," Tech. Rep.

[21] D. A. Peters Professor, "Toward a Unified Lift Model for Use in Rotor Blade Analyses Stabil ity," Tech. Rep.

[22] V. K. Truong, "A 2-D Dynamic Stall Model Based on a Hopf Bifurcation," Tech. Rep., Sep. 1993.

[23] J. Moncino, “Static and Dynamic Response of Airfoils in Reversed Flow,” Ph.D. dissertation, Insitute for Aerodynamics and Gas Dynamics University of Stuttgart & GE Wind Energy GmbH, Dec. 2021.

[24] W. Sheng, R. A. D. Galbraith, and F. N. Coton, “A New Stall-Onset Criterion for Low Speed Dynamic-Stall,” *Journal of Solar Energy Engineering*, vol. 128, no. 4, pp. 461–471, Nov. 2006, ISSN: 0199-6231. DOI: 10.1115/1.2346703. [Online]. Available: https://asmedigitalcollection-asme-org.tudelft.idm.oclc.org/solarenergyengineering/article/128/4/461/464153/A-New-Stall-Onset-Criterion-for-Low-Speed-Dynamic.

[25] D. Herring, A. Niven, and R. Galbraith, *Analysis of reattachment during ramp down tests*, 1988. [Online]. Available: http://hdl.handle.net/20.500.11881/2782.

[26] W. Sheng, R. A. D. Galbraith, and F. N. Coton, “A modified dynamic stall model for low mach numbers,” *Journal of Solar Energy Engineering, Transactions of the ASME*, vol. 130, no. 3, pp. 0 310 131–03 101 310, Aug. 2008, ISSN: 01996231. DOI: 10.1115/1.2931509/469315. [Online]. Available: https://asmedigitalcollection-asme-org.tudelft.idm.oclc.org/solarenergyengineering/article/130/3/031013/469315/A-Modified-Dynamic-Stall-Model-for-Low-Mach.

[27] W. Sheng, R. A. Galbraith, and F. N. Coton, “Improved Dynamic-Stall-Onset Criterion at Low Mach Numbers,” *https://doi-org.tudelft.idm.oclc.org/10.2514/1.29163*, vol. 44, no. 3, pp. 1049–1052, May 2007, ISSN: 15333868. DOI: 10.2514/1.29163. [Online]. Available: https://arc-aiaa-org.tudelft.idm.oclc.org/doi/10.2514/1.29163.

[28] P. G. Wilby, “The development of rotor airfoil testing in the UK,” *Journal of the American Helicopter Society*, vol. 46, no. 3, pp. 210–220, 2001, ISSN: 00028711. DOI: 10.4050/JAHS.46.210.

[29] A. J. Niven and R. A. D. Galbraith, “Modelling dynamic stall vortex inception at low Mach numbers,” *The Aeronautical Journal*, vol. 101, no. 1002, pp. 67–76, Feb. 1997, ISSN: 0001-9240. DOI: 10.1017/S0001924000066732. [Online]. Available: https://www-cambridge-org.tudelft.idm.oclc.org/core/journals/aeronautical-journal/article/abs/modelling-dynamic-stall-vortex-inception-at-low-mach-numbers/6B66625AAC1395FE8C605BD8BA5749FB.

[30] T. S. Beddoes, “A Third Generation Model for Unsteady Aerodynamics and Dynamic Stall,” Westland Helicopter Limited, Tech. Rep., 1993.

[31] L. G. dos Santos and F. D. Marques, “Improvements on the Beddoes–Leishman dynamic stall model for low speed applications,” *Journal of Fluids and Structures*, vol. 106, Oct. 2021, ISSN: 10958622. DOI: 10.1016/J.JFLUIDSTRUCTS.2021.103375.

[32] L. G. P. dos Santos, *GitHub Repository for ” Improvements on the Beddoes–Leishman dynamic stall model for low speed applications.” by dos Santos, L. G. P., & Marques, F. D. (2021)*.

[33] Z. Zhang, J. Li, S. R. Nielsen, and B. Basu, “Mitigation of edgewise vibrations in wind turbine blades by means of roller dampers,” *Journal of Sound and Vibration*, vol. 333, no. 21, pp. 5283–5298, Oct. 2014, ISSN: 0022-460X. DOI: 10.1016/J.JSV.2014.06.006.

A

Supplementary Results Figures

A.1. Modified SGC Vortex Effects

A.1.1. Delay

GE2021 is used to model separation effects, this limits the extent that vortex effects are able to impact the modelled results. An illustration of this issue is clear in the results showcased in Figures 6.5, A.1 and A.2, where although the initial increase in $-C_L$ is better matched with the use of the delayed angle of attack, the modelled decay rate is slower than the one observed in the experimental data.

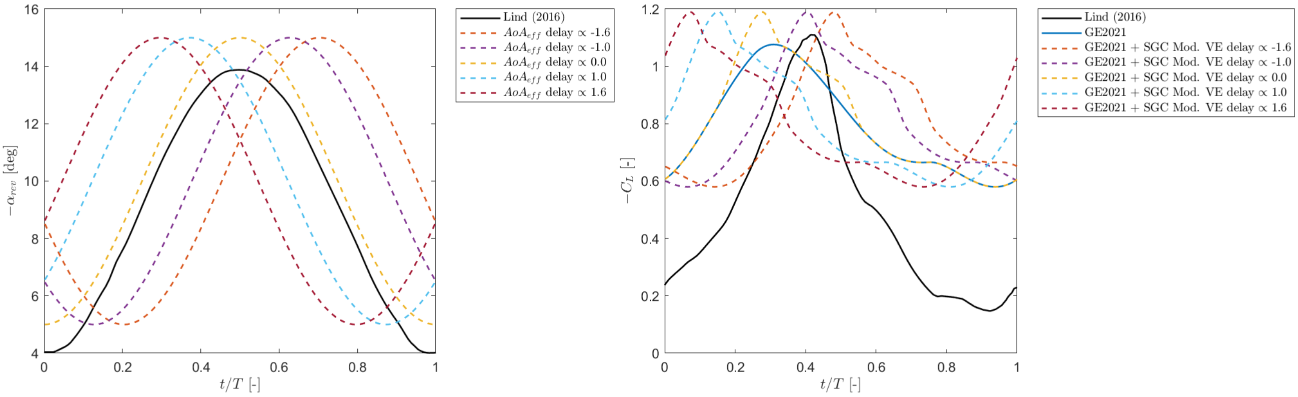

Figure A.1: AoA and $-C_L$ using Modified SGC vortex effects for Case B with different delay proportionality constants (d).

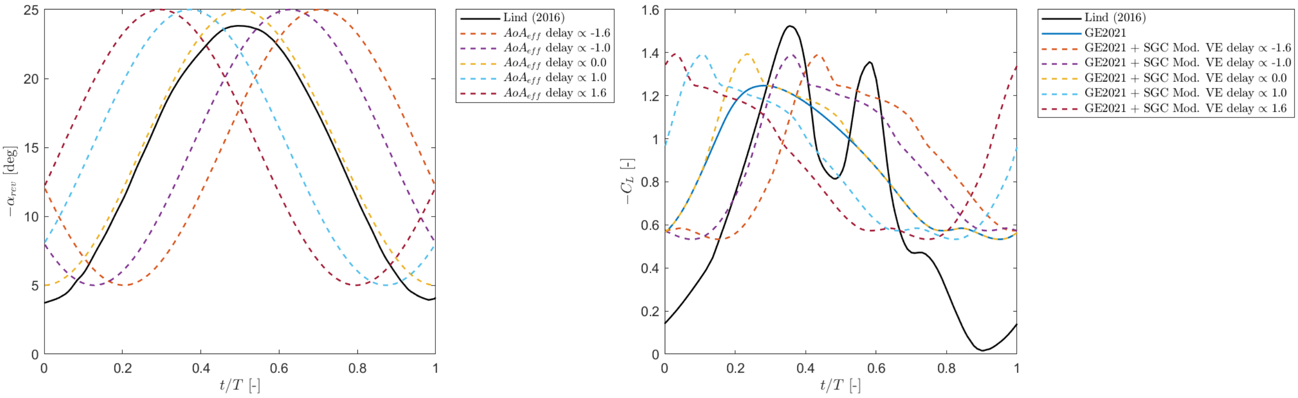

Figure A.2: AoA and $-C_L$ using Modified SGC vortex effects for Case D with different delay proportionality constants (d).

A.1.2. Dynamic Stall Onset

As discussed in Section 6.2.1.2, both Cases D (Figure 6.7) and B (Figure A.3), showcase values for $-C_L$ at $-\alpha_{rev} \approx 5°$ that double and triple the experimental data. The cause for this difference between empirical and numerical data was further explored in Chapter 5, and rooted on the reliance on the static polar to calculate the inviscid lift. This impacted the lift obtained from the computation of the flow separation effects.

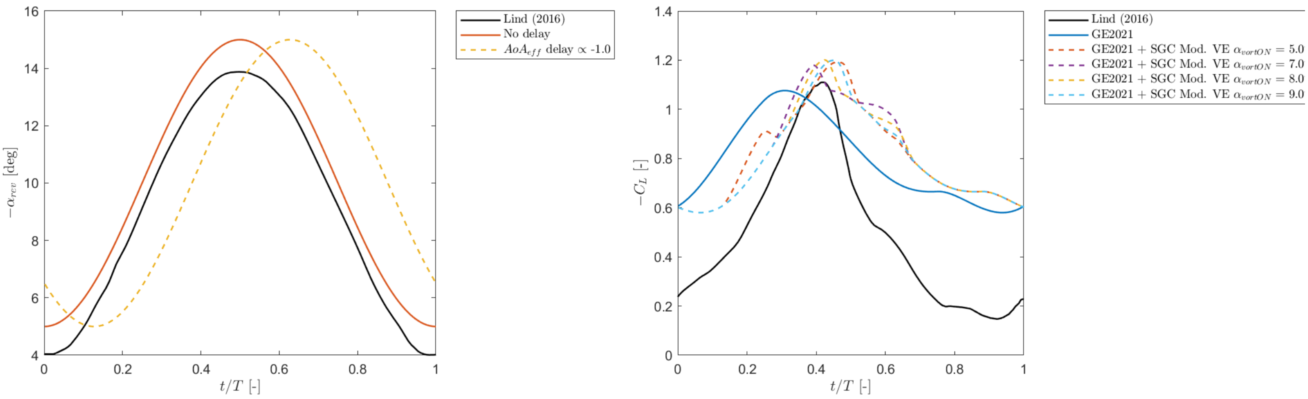

Figure A.3: AoA and $-C_L$ using Modified SGC vortex effects for Case B with different stall onset AoA α_{vortON}.

A.1.3. Vortex Strength

In Section 6.2.1.4, the fact that the amplitude of $-C_{L_v}$ remains relatively consistent throughout the six studied cases is discussed. The following figures help support that a single value of B_1 can be established to tune the impact of vortex effects on $-C_L$. Nevertheless, as also discussed in Section 6.2.1.4, a balance is always necessary to obtain acceptable results for the six cases.

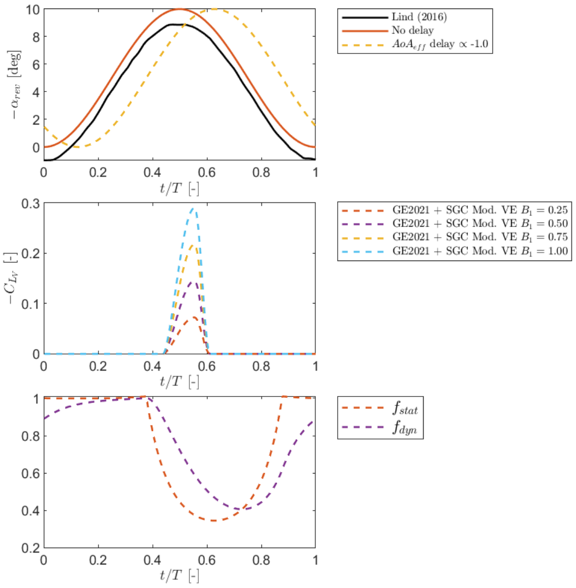

(a) Case A.

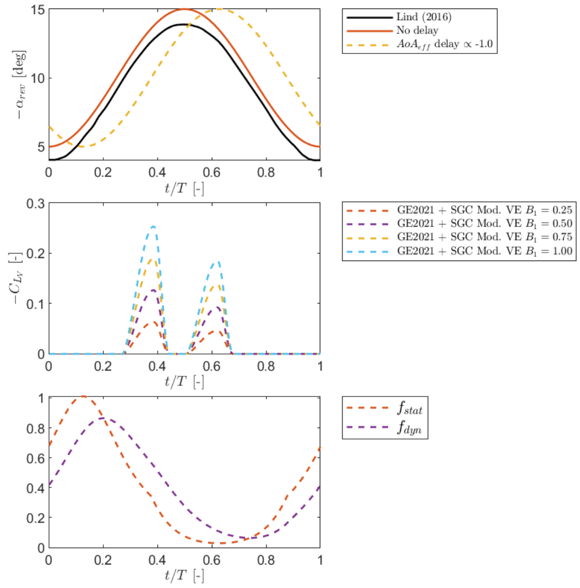

(b) Case B.

Figure A.4: Results for $-C_{L_V}$, τ_v and separation points with $d = -1$, using different vortex intensity proportionality coefficients B_1.

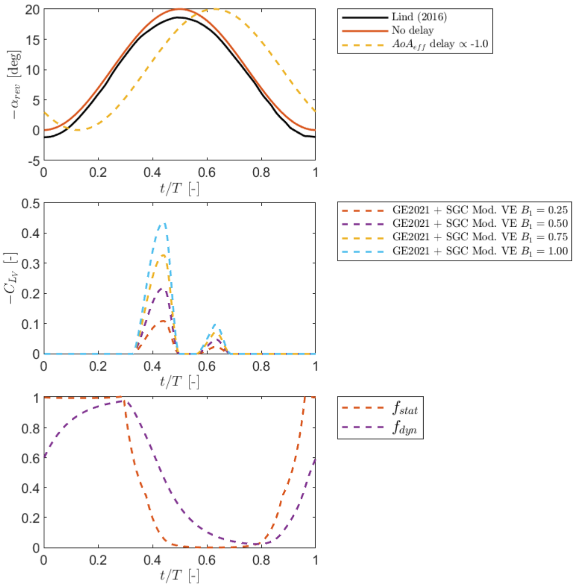

(a) Case C.

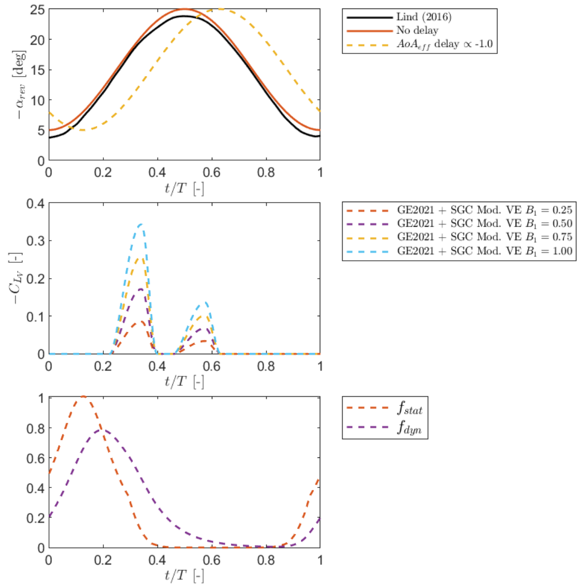

(b) Case D.

Figure A.5: Results for $-C_{L_V}$, τ_v and separation points with $d = -1$, using different vortex intensity proportionality coefficients B_1.

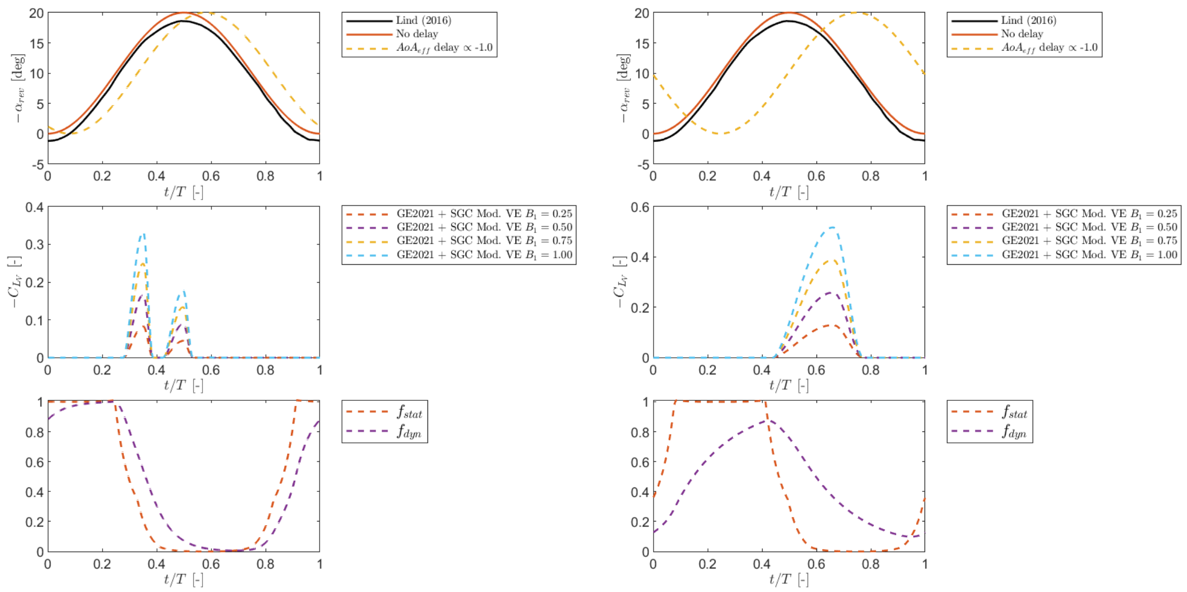

(a) Case E. **(b)** Case F.

Figure A.6: Results for $-C_{L_V}$, τ_v and separation points with $d = -1$, using different vortex intensity proportionality coefficients B_1.

A.2. Sinusoidal Vortex Effects

A.2.1. Delay

Figure 2.10 shows that varying the reduced frequency has an effect on the effective angle of attack in reverse flow dynamic stall. However, being the GE2021 a heavily validated model, it was worth assessing whether the proposed delayed angle of attack distribution should be applied to the full flow behaviour, or solely to the vortex effects that were added to the GE2021 model. Although Cases E, C and F were studied in Section 6.3.1, other cases can be useful to understand the impact of a partial or full delay.

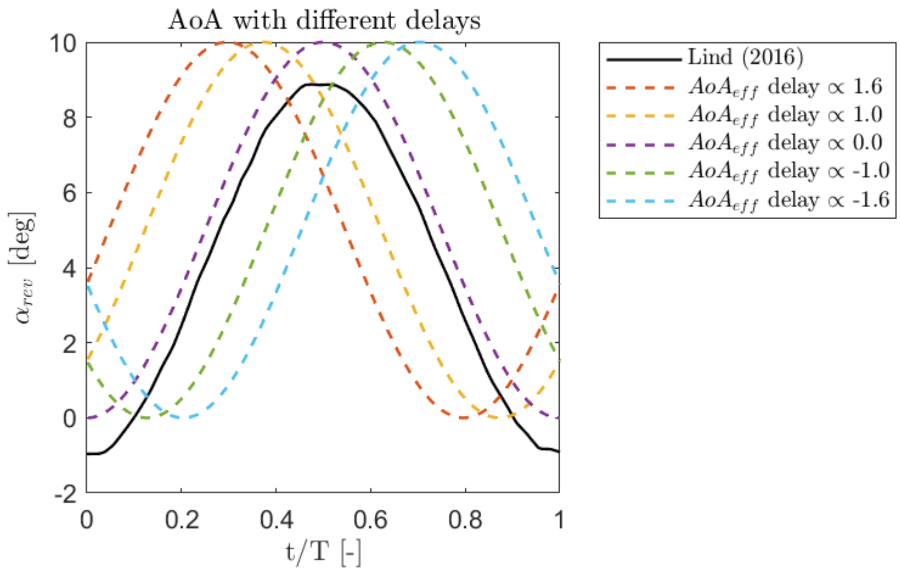

Figure A.7: AoA for Case A delay with different proportionality constants (d).

Figure A.7 visually depicts the slight difference between the modelled angle of attack and the angle of attack utilized by Lind [14] due to the previously discussed calibration issues. In addition, several angle of attack distributions are represented, each with a different delay proportionality constant.

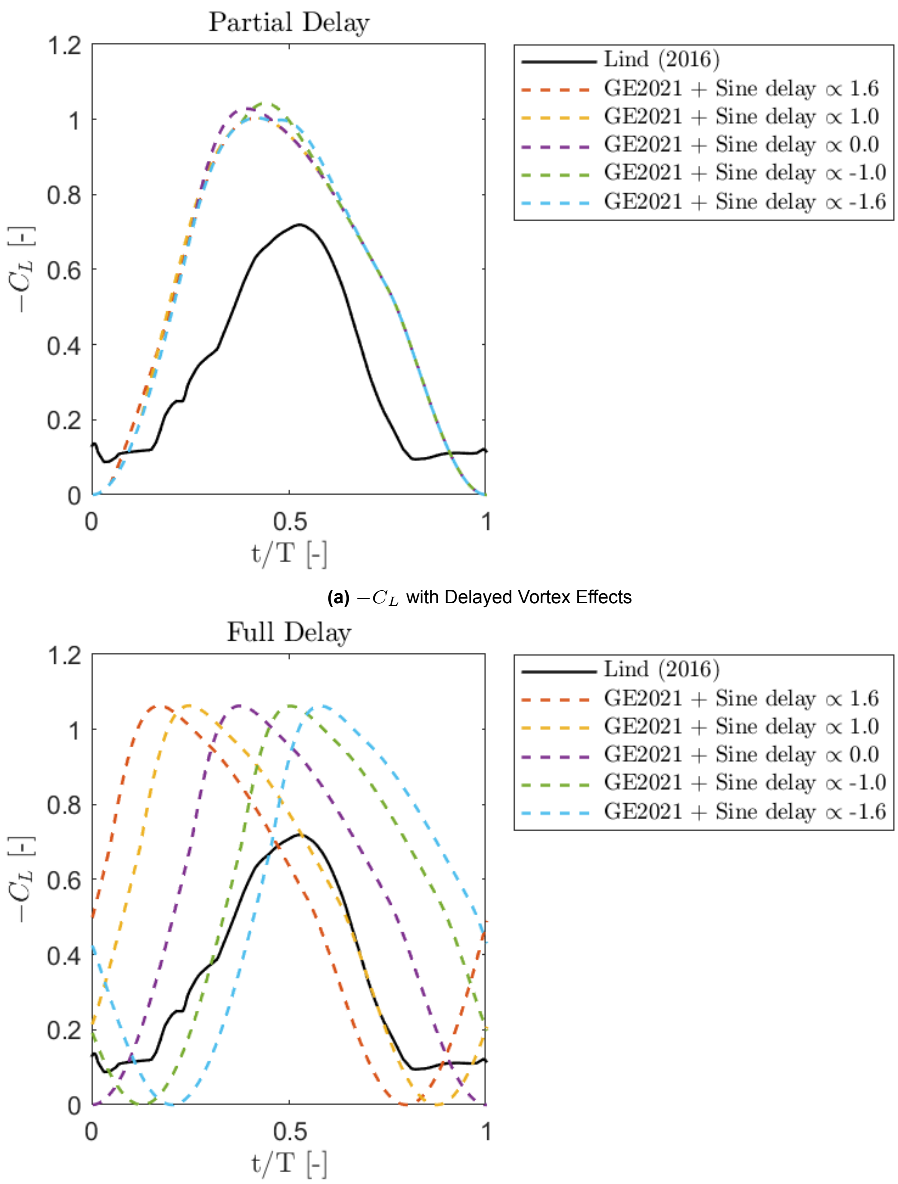

(a) $-C_L$ with Delayed Vortex Effects

(b) $-C_L$ with Full Delay

Figure A.8: Case A

In Figure A.8a, the lift coefficient that is modelled by incorporating a delay solely in the vortex effects or utilizing a partial delay can be observed. This comparative analysis allows to assess the impact of these modifications on the lift coefficient behavior. On the other hand, Figure A.8 provides a comprehensive view of the effect of a full delay, where the previously computed $\alpha(t)$ (Equation 6.4) is employed to calculate separation and vortex effects.

Case A represents a scenario where the influence of vortex effects is relatively low. Consequently, the observed impact of vortex structures on the lift coefficient is noticeably small in both the experimental and modelled data. However, this case serves as a crucial reference point to highlight the limitations of the current model GE2021 and any proposed modifications. Despite the inclusion of vortex effects in the GE2021 model, it becomes evident that these effects alone might not be sufficient to accurately capture the complexities of reverse flow dynamic stall. The modelled representation of the separated flow, in comparison to the actual behavior, exhibits a more pronounced impact that does not align with the physical reality of reverse flow dynamic stall. Therefore, further refinements and enhancements might be necessary to properly assess the impact of separation and vortex effects during reverse flow dynamic stall.

Case D is another case worth discussing as the impact of the sinusoidal vortex effect becomes distinctly visible. When comparing the baseline lift coefficient with separation effects calculated using the GE2021 model to the experimental data, discrepancies are observed at the beginning and end of the cycle where the angle of attack is at its lowest value. This disparity highlights the need for the previously mentioned assessment of the impact of separation effects in reverse flow.

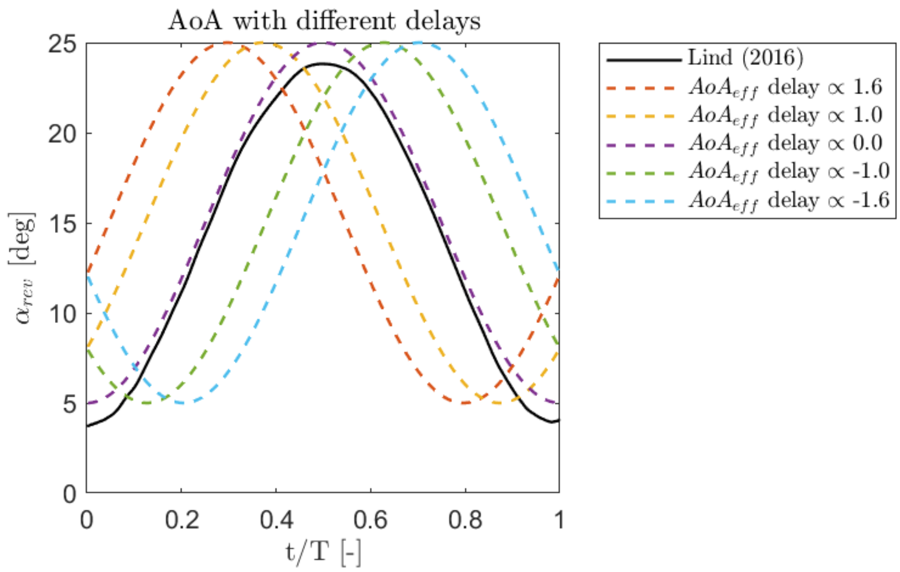

Figure A.9: AoA for Case D delay with different proportionality constants (d).

Examining Figure A.10a, where delay is solely applied to the vortex effects, a notable distinction between the modelled data and the experimental results in terms of the lift coefficient can be observed. The modelled data exhibits an earlier and more rapid increase and decay compared to the experimental data. Specifically, in the region where $t/T < 0.15$, the experimental data displays a lower slope, while between $0.15 \leq t/T \leq 0.35$, the slope becomes steeper. Interestingly, by applying a full delay (Figure A.10b), a closer alignment with the steeper slope observed in the experimental data is achieved.

The results obtained by applying a full delay, affecting separation and vortex effects, using either $d = -1.0$ or $d = -1.6$, not only more closely resemble the aforementioned slope but also exhibit peaks that better align with the primary and secondary vortex formations observed in the experimental data. This suggests that incorporating a full delay in the model allows for a more accurate representation of the dynamics associated with reverse flow dynamic stall, resulting in improved agreement with experimental observations.

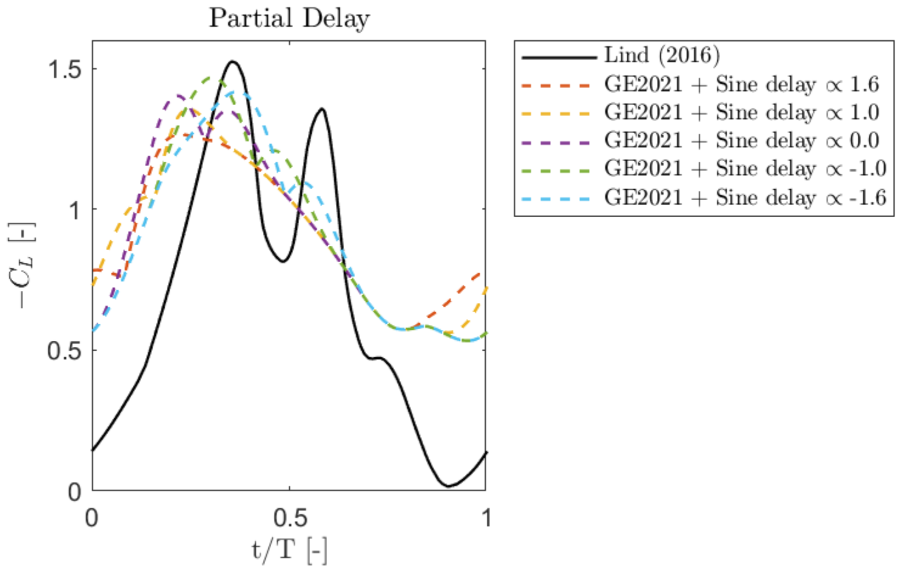

(a) $-C_L$ with Delayed Vortex Effects

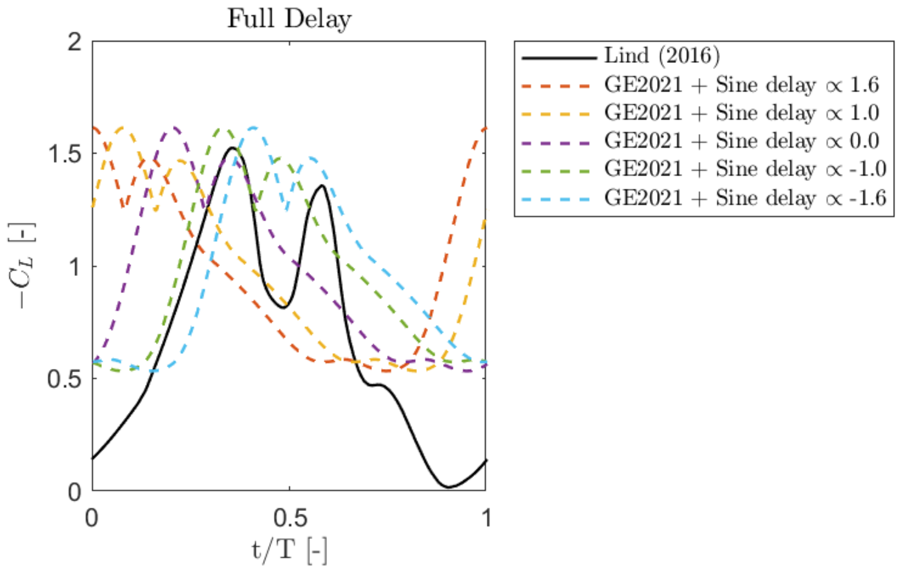

(b) $-C_L$ with Full Delay

Figure A.10: Case D